CHARACTERIZATION AND MITIGATION OF SINGLE-EVENT EFFECTS IN RF CIRCUITS AND SYSTEMS

A Dissertation
Presented to
The Academic Faculty

by

Adrian Ildefonso Rosa

In Partial Fulfillment
of the Requirements for the Degree
Doctor of Philosophy in the
School of Electrical and Computer Engineering

Georgia Institute of Technology
August 2020

CHARACTERIZATION AND MITIGATION OF SINGLE-EVENT EFFECTS IN RF CIRCUITS AND SYSTEMS

Approved by:

Dr. John D. Cressler, Advisor
School of Electrical and Computer Engineering
Georgia Institute of Technology

Dr. Nelson E. Lourenco
School of Electrical and Computer Engineering
Georgia Institute of Technology

Dr. Hua Wang
School of Electrical and Computer Engineering
Georgia Institute of Technology

Dr. Shimeng Yu
School of Electrical and Computer Engineering
Georgia Institute of Technology

Dr. E. Glenn Lightsey
Daniel Guggenheim School of Aerospace Engineering
Georgia Institute of Technology

Date Approved: July 2, 2020

ACKNOWLEDGEMENTS

First, I would like to express my deepest gratitude to my advisor, champion, and mentor, Dr. John D. Cressler. Throughout the years you have shown me a level of kindness, support, guidance, trust, and confidence that has allowed me to grow as a researcher and as a person. Thank you for the many opportunities to bring my own views into our research, and for letting me pursue those experiments that may have been on the riskier side. Thank you for encouraging me to find my own "style" of research, teaching, and mentorship, and for the safety net when one of my attempts failed. Thank you for being patient through my growth and training. Thank you for helping me expand my world view both philosophically and literally (I promise all those trips were a good investment!). Your presence in my life has been a truly positive force, that I hope continues for years to come.

I would like to thank the other members of my dissertation committee, Dr. Nelson Lourenco, Dr. Hua Wang, Dr. Shimeng Yu, and Dr. Glenn Lightsey. The valuable feedback you have provided will shape some of my future work in this research area.

I would also like to thank the folks at the U. S. Naval Research Laboratory: Ani, Joel, Steve, Jeff and Dale for their technical mentorship and help conducting experiments for this work.

Thank you to all the members of the SiGe Team for their help and support throughout the years. In particular, I would like to thank Anup, Sunil, Jeff, Victor, Milad, Yunyi, Uppili, Harrison, Nelson Sepúlveda, Peter, Chris Coen, Rob, and Adilson. All of those late nights doing tapeout and radiation experiments would not have been possible without counterbalancing those experiences with shared beers, trashketball, ping pong tournaments, and long lunches.

I want to extend a special thank you to all the folks in the radiation effects team: George, Delli, Zach, Nelson Lourenco, and Mason. Thanks for all your challenging questions, the support during experiment trips, and the good times through the years. Your help and support have directly shaped the results of this dissertation.

Thank you to the amazing staff that made this work possible. In particular, I would like to thank Alison, Carolyn and Janine, my three gladiators who fought the logistical hurdles of performing off-site research experiments. None of this work would have been possible without your support.

I would also like to thank all my life mentors and those friends who have chosen to "do life" with me (you know who you are!), for their valuable counsel throughout the years. Thank you for supporting me and calling me out when I have needed it the most, and for knowing me well enough to know the difference.

To all my friends with whom I have shared special beers through the years Johnny, Nash, Brian and Emma, thank you for the good times, late night conversations, and moral support through the years. I used to say that a having few beers with friends was cheaper than therapy, but after all these years, I'm afraid to do the math.

Thank you to my friends Ormarie, Angel, and Mónica for their support through the years. These past 10 years together have been quite a ride, and I am a better person for having you with me. Hope you're ready for the next 10 years.

To my friends "Los Colomborriqueños" from the University of Puerto Rico at Mayagüez, thank you for helping me get through some difficult challenges (both in and out of the classroom) and making it possible for me to get to Georgia Tech!

Special thanks to my parents, Olivo and Lourdes, and my brother and his wife, Adriel and Cristina for their constant encouragement.

Finally, to all my friends and family, thank you for your continued support throughout the years, even when you had no idea what I was doing. Know that you have a special place in my heart.

TABLE OF CONTENTS

LIST OF TABLES

LIST OF FIGURES

SUMMARY

Orbital and space radiation environments can strongly limit the performance and reliability of spacecraft payloads. When energized particles penetrate spacecraft shielding and traverse electronic systems, they can generate voltage and current spikes known as single-event transients (SETs). These SETs can propagate through electrical systems, potentially disrupting their proper operation. In the context of an RF communications systems payload, the data being received by the spacecraft can be corrupted by SETs. These events could lead to critical issues if the on-board computer interprets these corrupted data as a command and executes an unintended action. In practice, it is not possible to completely shield electronic systems from these events. Thus, to ensure the proper operation of spacecraft in radiation environments, the risk of these events must be considered and, if necessary, mitigated.

There are three major phases in the risk management process: testing, assessment, and mitigation. During the testing phase, radiation sources on Earth are used to emulate the space environment and reproduce any damage that electronics may experience when exposed to space radiation. Then, the results are used to identify changes in relevant performance metrics for a given system and assess the risk that these changes pose to the mission. If the risk is too high, design techniques can be utilized at the device, circuit, and system level to mitigate these risks.

The objective of this research is to develop new approaches to test, assess, and mitigate the risks of single-event transients in RF communications systems. Two different techniques are presented for testing single-event effects. These techniques utilize pulsed lasers to emulate the SETs that result when heavy ions traverse semiconductor devices. A new approach for characterizing single-event effects in RF receivers

with modulated data is then presented. Finally, three different mitigation techniques that can be applied to RF communications systems are also presented. These techniques involve the detection of SETs in RF systems, using *pnp* devices in place of *npn* devices, and using silicon-on-insulator substrates to limit charge collection on the electrical terminals of the device. The results shown are all based on device test structures and circuits that utilize silicon-germanium heterojunction bipolar transistors (SiGe HBTs). A summary of the contributions from this research follows.

1. A new approach to quantitatively correlate single-event transients produced by two-photon absorption and heavy ions in SiGe HBTs. This work was presented at the 2018 IEEE Nuclear and Space Radiation Effects Conference (NSREC) and published in the IEEE Transactions on Nuclear Science (© 2019 IEEE) [5]. This work was also selected for the "Outstanding Student Conference Paper Award" and the "Outstanding Conference Paper Award" for NSREC 2018.

2. The first investigation on the use of quasi-Bessel beams to generate laser-induced transients in SiGe HBTs via two-photon absorption. This work has been accepted for an oral presentation at the 2020 IEEE Nuclear and Space Radiation Effects Conference and will be submitted to the IEEE Transactions on Nuclear Science.

3. A new characterization technique for single-event transients in RF communications systems that uses I-Q diagrams. This work was presented at the 2016 Radiation Effects on Components and Systems (RADECS) Conference and was published in the IEEE Transactions on Nuclear Science (© 2017 IEEE) [3, 6].

4. Demonstrated the use of an RF power detector to sense single-event transients in RF circuits. This work was presented at the 2017 IEEE Nuclear and Space Radiation Effects Conference and published in the IEEE Transactions on Nuclear Science (© 2018 IEEE) [7].

5. An investigation of the single-event transient response of commercial SiGe HBTs on bulk and silicon-on-insulator substrates. This work was presented at the 2019 IEEE Nuclear and Space Radiation Effects Conference and published in the IEEE Transactions on Nuclear Science (© 2020 IEEE) [8]. This work was also nominated for the "Outstanding Conference Paper Award".

6. An assessment of the tradeoffs between RF performance and single-event transient robustness of low-noise amplifiers designed using only *npn* and only *pnp* SiGe HBTs in a complementary SiGe BiCMOS platform. This work was presented at the 2019 Radiation Effects on Components and Systems Conference and has been accepted for publication in the IEEE Transactions on Nuclear Science (© 2020 IEEE). The paper is available online as "Early Access" [9].

Acknowledgment of Support

The material in this dissertation is based on work supported by the Defense Threat Reduction Agency under contracts HDTRA-1-13-C0058 and HDTRA1-16-1-0018, and by the National Science Foundation Graduate Research Fellowship Program under Grants DGE-1148903 and DGE-1650044.

CHAPTER I

INTRODUCTION

1.1 The Satellite That Changed Everything

"Good afternoon. I understand that part of today's press conference is being relayed by the Telstar communications satellite to viewers across the Atlantic, and this is another indication of the extraordinary world in which we live. This satellite must be high enough to carry messages from both sides of the world, which is of course a very essential requirement for peace, and I think this understanding which will inevitably come from the speedier communications is bound to increase the well-being and security of all people, here, and those across the oceans" [10].

When President John F. Kennedy uttered these powerful words on July 23, 1962, he made history. This press conference, was the first one transmitted via satellite across the Atlantic Ocean. The world's first transatlantic television signal had been relayed by the Telstar 1 satellite only 11 days earlier [1]. The potential for societal, political, and economic impacts of this new technology was immediately apparent as the dollar strengthened in Europe shortly after President Kennedy denied rumors that the U.S. would be devaluing it during this press conference. A new era of communications had begun.

The Telstar 1 satellite, shown in Fig. 1, was the world's first active communications satellite. It was launched at the height of tensions between the United States and the Soviet Union during the Cold War as an "antidote to the possibility of nuclear war" [11]. The satellite flew in low-Earth orbit (LEO) and was only visible to ground stations for about 20 minutes every few hours. At the time, launching satellites in to a geostationary orbit (GEO), the preferred orbit for these types of satellites today,

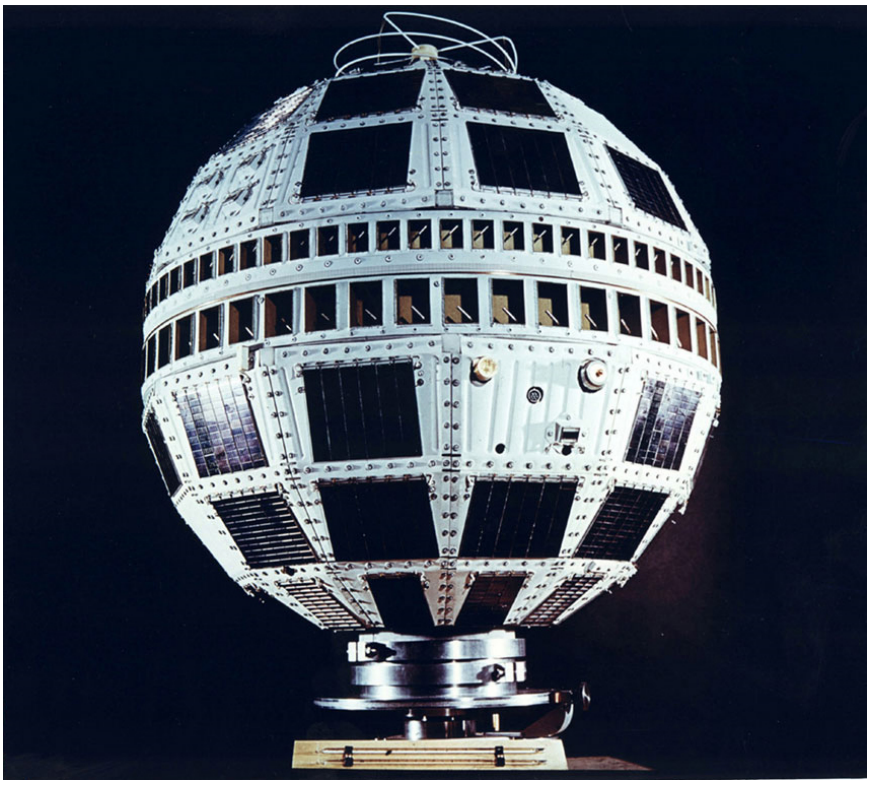

Fig. 1: Image of the Telstar 1 satellite (reproduced from [1]).

was significantly more challenging. The impact of this achievement was so widespread that it permeated into pop culture, and even inspired the traditional design of soccer balls at the time.

What President Kennedy or any of the others watching this press conference could not have known that day is that the mission of Telstar 1 would be short-lived.

On November 24, 1962, only several months after its initial broadcast, Telstar 1 experienced its first malfunction when the command system failed to respond. The previous months foreshadowed this malfunction as some systems showed signs of sluggish performance and intermittent operation [12]. In February 1963, less than a year after its launch, Telstar 1 was no longer operational. The early demise of Telstar 1 was a direct result of enhanced radiation in the inner Van Allen belt.

When the Telstar 1 was built, engineers and scientists already knew of the existence of charged energetic particles trapped in the Van Allen belts. Their design

had accounted for some degradation in performance of the electronics due to exposure to radiation. Yet when the Telstar 1 started malfunctioning, it had received approximately two hundred times the expected dose [13].

The day before Telstar 1 launched, the U. S. Air Force conducted their largest high-altitude nuclear test, which launched from Johnston Island in the Pacific. Named Starfish Prime, this test detonated a 1.4-megaton nuclear warhead. The damage was larger than scientists expected. The explosion caused an electromagnetic pulse so strong that it disrupted the electrical power and destroyed several traffic lights in Hawaii. An artificial aurora borealis terrified many observers. The test also increased the amount of radiation surrounding Earth.

This detonation directly increased the flux of charged particles in the inner Van Allen Belt by two orders of magnitude. The impact was so strong that effects were still measurable five years later. At least eight satellites were directly damaged by the Starfish Prime event. Telstar 1, was the first casualty of exposure to ionizing radiation in space.

At the time, the reasons for performance degradation of electronics due to ionizing radiation were not well understood [13]. The complexities of this problem were exacerbated by nuances associated with semiconductor fabrication processes. As an example, when the fabrication of the National Semiconductor LM139, a common comparator chip, was moved from Scotland to Texas, the company made some slight modifications to the layout of the chip. The part was essentially the same, but these minor changes lowered the tolerable amount of dose that the part could survive from 100 krad to 30 krad [14].

Today, it is well known that orbital and space radiation environments can strongly limit the performance and reliability of spacecraft payloads [15]. Mitigation techniques are typically put in place to prolong the lifetime of these systems. Throughout the duration of a mission, however, energized particles can still penetrate spacecraft

shielding and cause damage to the on-board electronics.

This chapter presents a cursory overview of the effects of radiation on microelectronics. First, the three main types of radiation effects in electronics are discussed. Although the techniques presented in this dissertation can be applied to other fabrication processes, the experiments shown were performed using Silicon-Germanium Heterjunction Bipolar Transistor (SiGe HBTs). Thus, a section on the specific effects of radiation on SiGe HBTs follows. Then, a general overview of testing, assessment and mitigation techniques for microelectronics is presented. Some general applications of RF circuits and systems in spacecraft are then briefly introduced. Finally, the main objectives and layout of this dissertation are presented.

1.2 Overview of the Effects of Radiation on Microelectronics

The space environment adds several challenges to the already difficult job of spacecraft designers. In particular, the high levels of radiation that electronics encounter in space can have serious implications for the spacecraft design process. Although an exceptionally interesting topic, a discussion of the sources of radiation in space and the dynamics of the space climate are outside of the scope of this dissertation. The interested readers are referred to [16] for a review of space climatology in the context of spacecraft electronics applications. Instead, this text is focused on the effects of this radiation on electronic systems. There are three major types of radiation-induced damage in electronics: 1) total ionizing dose (TID) effects, 2) displacement damage dose (DDD) effects, and 3) single-event effects (SEEs). The text below provides a cursory explanation of each of these effects.

Total Ionizing Dose TID effects are cumulative, and are a result of energy deposition in insulating materials, which can degrade device and circuit performance [17,18]. When ionizing radiation deposits energy in an insulator and generates electron-hole pairs, the electric field across the insulator will tend to separate these charges. Since

electrons have higher mobility than holes, they tend to be swept away by the electric field, leaving holes trapped in the insulator. Over time, these holes can diffuse through the localized states in the oxide towards the insulator-semiconductor interfaces and result in interface traps. Some notable effects of these traps in MOSFETs are threshold voltage shifts, off-state leakage current increases, and increases in 1/f noise [19,20]. At the circuit and system level, TID can reduce the gain and bandwidth of amplifiers, increase the noise in certain systems, and prevent logic circuits from switching. This effect was the one responsible for the malfunction of the Telstar 1.

Displacement Damage Dose DDD effects are a result of a particle with mass penetrating the semiconductor material and losing energy through non-ionizing mechanisms. This process can result in the incident particle physically displacing atoms in the semiconductor lattice, which could lead to point defects [21]. These defects could, in turn, lead to increased recombination centers that can increase leakage current in devices. Furthermore, if the displaced atom is a dopant species that forms an interstitial defect, this dopant will no longer be electrically active. This effect is known as dopant deactivation and can cause shifts in device performance. These days, DDD effects are a concern for solar cells as their efficiency can be significantly degraded.

Single-Event Effects In the broadest sense, the term "single-event effects" is an umbrella term used to describe events occurring at a specific instance of time, as opposed to cumulative effects such as TID and DDD. In general, an SEE occurs when an ionized, high-energy particle or photon penetrates a semiconductor material. As it passes through, the particle or photon transfers its energy to the material and creates electron-hole pairs along its path. The generated carriers can then be separated by the internal electric fields of active devices, generating a current that can have adverse effects on the circuit operation [22]. These effects are typically transient in nature, and although often non-destructive, they are still of interest to the space

community as they can alter the proper operation of systems or compromise the data acquired by scientific instrument. Examples of these types of effects include: single-event transients (SETs), in which the current generated in the material exits through the device terminals and propagates through the circuit or system; and single-event upsets (SEUs), in which a bit in a digital system is flipped from a logic high to a logic low or vice versa.

There are some instances in which SEEs could be catastrophic, and can result in permanent damage to the devices or circuits affected. Examples of these effects include: single-event latchup (SEL), in which a positive feedback is established in a thyristor structure and can lead to device destruction if not contained; single-event burnout (SEB), in which a power FET is forced into thermal runaway that could also lead to device destruction; and single-event gate rupture (SEGR), in which the gate dielectric of a FET ruptures due to an excessively high electric field during a transient event [23].

1.3 Radiation Effects in SiGe HBTs

Most of the research included in this dissertation utilizes SiGe HBTs as they have been shown to have great potential for building electronics for extreme environments, including space applications [24–27]. The attractiveness of SiGe BiCMOS technologies stems from the ease of integration with existing CMOS platforms with little overhead cost. This integration allows for the design and fabrication of high-performance, monolithic, mixed-signal circuits and systems. Designers can use SiGe HBTs for high-performance analog and RF applications, while at the same time leveraging the highly-scaled CMOS devices for dense digital circuitry. A comprehensive treatment of SiGe HBTs and their applications in electronic systems is outside the scope of this dissertation. Instead, the reader is referred to [28] and the references therein. However, a brief introduction to the effects of radiation on the performance of SiGe

HBTs follows.

SiGe HBTs enjoy an increased robustness to TID compared to most CMOS technologies, and are said to be tolerant to multi-Mrad(SiO_2) dose levels [27,29,30]. Their built-in TID tolerance is a result of the device structure required to deposit the SiGe alloy in the base. The main effect of TID on SiGe HBTs is an increase in base leakage current and a reduction in current gain at low injection. This increase in base current is a result of interface traps generated along the emitter-base (E-B) spacer. However, for most high-performance circuits, these devices are biased above the point where the change in leakage current is significant and its effect on circuit performance is typically minor.

There are few studies showing only DDD effects in SiGe HBTs [31, 32], due in part to the difficulty of obtaining clean neutron beams that allow separation of DDD and TID effects. The results suggests that, due to the relatively high doping levels in SiGe HBTs, DDD effects are not the limiting factor in their radiation response.

Although SiGe HBTs are considered to be robust against TID and DDD effects, they are particularly susceptible to SEEs, in particular, to SETs. There have been many studies on the SET response of SiGe HBT devices and circuits, a subset of which includes [6, 7, 27, 33–45]. When a heavy ion passes through the emitter-base-collector stack, the high-density of carriers generated in this region will effectively break down the built-in electric fields in the junctions, which is also known as the "ion shunt" effect. This large amount of excess carriers leads to current transients with relatively large amplitudes. In addition, any transient occurring outside this emitter-base-collector stack will also lead to charge collection by the reverse-biased sub-collector to substrate junction [27]. Since the collector is typically the output for most circuits, this effect is also of concern for proper circuit operation.

A recent study showed that the germanium-induced quasi-drift field in the SiGe base plays a significant role in the SET response of SiGe HBTs, and that increasing

the Ge content in the base increases the amplitude and duration of the transients measured at the device terminals [33]. This result represents a challenge for future generations of SiGe HBTs, as increasing Ge content and the quasi-drift field in the base are typical strategies to improve device performance. Since these changes also increase their susceptibility to SEEs, researchers must be intentional about mitigating these effects at the device, circuit, and system level. Thus, research on characterizing and mitigating SEEs in circuits and systems built with SiGe HBTs continues, and is one of the themes of this dissertation.

1.4 Radiation Hardness Assurance

Radiation Hardness Assurance (RHA) is the process of ensuring that components, subsystems, and systems will meet mission requirements when operating in a radiation environment with a given probability of survival and confidence level. This process begins with the definition of mission requirements (e.g., launch date, duration, orbit, operations and data handling). Once the mission requirements are established, the radiation environment is defined. Then, the response of electronic systems to this environment must be identified, including all vulnerabilities and risks to the success of the mission. The radiation-related risks are then managed in a step that involves three major phases: testing, assessment, and mitigation. These three phases are the main topic of this dissertation.

1.4.1 Testing

During the testing phase, radiation sources on Earth are used to emulate the space environment and reproduce any damage that electronics may experience when exposed to harsh conditions. Appropriate selection of radiation sources to adequately emulate the environment of a given mission is essential to properly assess the risk of using a given electronic system on a spacecraft. For SEE testing, particle accelerators are typically used to characterize the response of electronics to heavy ions, protons, and

electrons. However, "beam time" at these facilities can be limited and expensive. An attractive alternative is to use pulsed lasers to emulate the effects of charged particles on electronics.

Pulsed-laser single-event effects (PL-SEE) testing provides information complementary to that of traditional heavy-ion broadbeam test campaigns performed for space qualification of electronic components [46]. In particular, PL-SEE testing allows experimenters to identify sensitive device and circuit nodes [47–49], verify radiation-hardening-by-design (RHBD) implementations [50–52], screen parts for destructive effects such as single-event latchup (SEL) [53–55], inject localized faults into digital systems [56–58], study basic SEE mechanisms [59–61], and calibrate and validate models [62].

PL-SEE testing is a powerful tool that should be used in parallel with heavy-ion testing to produce more robust electronics for radiation-harsh environments. This testing technique could be used to screen parts before performing heavy-ion testing, reducing the demand for beam time at particle accelerators.

There are many differences between charge deposition from charged particle and optical sources, and most of the results obtained through PL-SEE testing often are qualitative in nature. Since the inception of PL-SEE techniques, researchers have sought to obtain quantitative agreement between heavy-ion- and laser-induced measurements. Despite some successes with correlating heavy-ion and laser charge generation through empirical factors [51, 55, 63, 64], this topic remains an active area research [65, 66], and will be addressed in this dissertation.

1.4.2 Assessment

The sensitivity of electronics to radiation must be quantified for the environment of a given mission. This process requires identifying changes in relevant performance metrics for a given system and assessing the risk that these changes pose to the

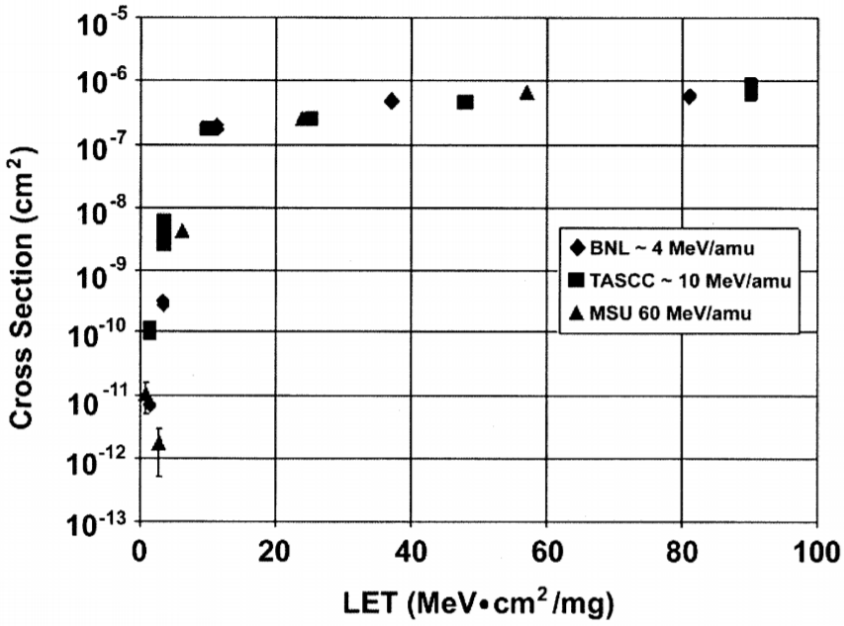

Fig. 2: Example of error cross section curve obtained from heavy-ion testing at different facilities. (reproduced from [2] © 2003 IEEE).

mission.

To effectively assess the risk of radiation to a mission, a performance metric needs to be specified and monitored during testing. In the context of SEEs, a typical metric is called the error cross section. For this metric, errors – which are broadly defined and application-specific – are measured as a function of linear energy transfer (LET). The error cross section is the number of errors normalized to the fluence of particles used in a given experiment. A typical example of an error cross section curve is shown in Fig. 2. The "errors" can vary depending on the application. For example, in memories and digital systems the errors take the form of SEUs, which means that a bit is flipped from a logic one to a logic zero, or vice versa. In other applications, SEL cross sections can be measured as a function of LET.

By knowing how susceptible the system is to errors when subjected to particles of a given LET, and how many particles of that same LET are present in a given mission, the overall sensitivity can be determined. This information is then used to determine the probability of an error occurring for the duration of the mission. The

risk to success of the mission will be determined by factors such as the error rate (i.e., how often errors are generated), the severity (i.e., whether they are destructive), and the criticality of the systems (i.e., where they are occurring in the spacecraft).

When the risks associated with the mission are too high, design techniques are utilized at the device, circuit, and system level to mitigate these risks.

1.4.3 Mitigation

Aside from typical shielding mechanisms employed by spacecraft designers to mitigate the effects of radiation on electronic systems, additional mitigation strategies are usually employed for increased robustness. There are four main approaches to mitigate SEEs

1. **Reduce Charge Generation:** This can be accomplished by adding additional shielding on the spacecraft so that the incident particles lose more energy before they reach sensitive electronics. Another way to accomplish this is by using electronics built from materials with a larger bandgap energies. Since the average energy to create electron-hole pairs (EHPs) inside a material is approximately three times the bandgap, a charged particle with a given energy will result in fewer EHPs in materials with larger bandgaps.

2. **Reduce Charge Collection:** Charge collection is dominated by drift and diffusion processes in a semiconductor device. This process can be modified by adding regions of increased carrier recombination inside and around devices. Additionally, device structure (e.g., twin/triple well structures), layout modifications (e.g., spatial separation of sensitive nodes), as well as choice of substrate (e.g., silicon-on-insulator) can limit charge collection.

3. **Modify Circuit Response:** The response of the circuit can be modified in different ways. First, the charge collected can be canceled using the signal path

by making changes in the circuit topology [67] or in the circuit layout [52]. In addition, filters can be added to remove fast transients in analog circuits.

4. **Modify System Response:** This approach includes changes to the architecture or operation of systems [68]. For example, a common system-level mitigation technique is to implement a majority voter, where a critical circuit or subsystem is triplicated and the output of all three copies are compared to identify data corrupted by an SEE. This approach is commonly known as triple-modular redundancy (TMR). In addition, SEL can be mitigated and prevented from being catastrophic by placing current monitors on all power supplies and power-cycling the system if an excessive (but still safe) amount of current is drawn. Using parity-checks, error detection and correction techniques, data retransmission, and active watchdog timers are all examples of system- and software-level radiation hardness.

These approaches can be alternatively classified into techniques that achieve radiation tolerance, also known as radiation hardness, by either using design techniques or by changing fabrication processes.

Radiation-hardening-by-design (RHBD) techniques encompass a broad range of approaches that utilize changes in the system design to mitigate the effect of radiation on their performance. These include changes in device layout, circuit topologies, system implementations, and software architecture [69]. RHBD techniques are attractive because they can be implemented in commercially available semiconductor fabrication platforms. Implementing radiation hardening techniques often involves a compromise in size, weight, power and cost. RHBD techniques allow for these tradeoffs to be taken into consideration for a given mission.

The alternative to RHBD techniques is radiation-hardening by process (RHBP), in which the semiconductor fabrication process is altered to reduce the adverse effects of radiation. An example of this is the use of silicon-on-insulator (SOI) processes to

prevent SEL, since the parasitic thyristor structure often present in CMOS processes would be removed. Using SOI platforms will also reduce charge collection [35, 70, 71]. However, changes in process to mitigate a particular effect on a given mission could be costly. Therefore, an RHBD approach is often preferred.

The appropriate implementation of mitigation techniques will depend on many factors, including the radiation environment, criticality of components, risk to the mission objectives, and cost of implementation. However, it is difficult to make systems that are infallible in the presence of radiation. With the constant development of new microelectronic technologies with improved performance, old mitigation techniques must be reevaluated and new ones explored.

1.5 RF Circuits in Space Systems

Ensuring the robustness of communications payloads on spacecraft is critical for the success of the mission. After its launch, the only way to interface with a satellite is through its communications system. Engineers and scientists on Earth depend on these systems to retrieve scientific data collected by spacecraft, monitor the health of other systems, and fix any issues that may arise during the course of the mission.

The RF communications circuits receiving messages from a ground station are particularly sensitive to SEEs, since they carry the weakest signals due to long transmission distances and atmospheric attenuation. The effects of SETs on RF communications systems remain relatively unexplored [72]. Most of the studies on data corruption due to SETs are done in digital systems because it is easier to determine errors in the digital domain. To test these systems, they are typically exposed to a source of energetic particles (e.g., proton or heavy-ion beams) and the SEU cross section is monitored as a function of particle energy. Such a useful comparison metric does not exist for RF systems carrying modulated data. Since data is encoded in the amplitude and phase of the signal, it is difficult to determine whether an error has

occurred until it has been converted into the digital domain. Such a metric would be relevant for determining the risk of SETs for RF communications systems, and one is proposed as part of this work.

The circuits used to conduct this research were designed to operate at C band. C band (4-8 GHz) is one of the most commonly used frequency bands for microwave satellite communications, along with Ku band (12-18 GHz), and Ka band (27-40 GHz) [73]. Satellite systems operating at these frequencies have supported many applications through the years such as commercial satellite communications (e.g., INTELSAT), maritime mobile systems (e.g., INMARSAT), and satellite mobile systems (e.g., Globalsat) [74]. In addition, carriers around 5 GHz have been considered for next-generation global navigation satellite systems, and this band has been designated for this purpose by the International Telecommunication Union [75–77]. Another application of RF circuits at these frequencies is the receiver of remote sensing satellites. One example is the synthetic aperture radar payload on board the RADARSAT-2 mission, which operates at 5.405 GHz [78]. Thus, RF circuits and systems designed in this frequency band can support several space applications and ensuring their tolerance to radiation is key for the proper operation of these systems.

Testing, assessing, and mitigating SETs in RF systems will be the main focus of this research.

1.6 Objective and Organization

The objective of this research is to develop new approaches to test, assess, and mitigate the risks of SETs in RF communications systems. As such, a chapter of this dissertation is dedicated to each of these phases in the radiation hardness assurance process. Chapter 2 presents two different testing techniques that utilize pulsed lasers to emulate the SETs that result when heavy ions traverse semiconductor devices. Chapter 3 introduces a new approach for characterizing SEEs in RF receivers with

modulated data, as well as an error metric used to assess the risk involved for space missions. Chapter 4 presents three different mitigation techniques that can be applied to RF communications systems. These techniques involve the detection of SETs in RF systems, using *pnp* devices in place of *npn* devices, and using silicon-on-insulator substrates to limit charge collection on the electrical terminals of the device. Finally, Chapters 5 and 6 include some concluding remarks, summarizes the author's contributions and presents some ideas for potential future research based on the results of this work.

CHAPTER II

USING PULSED-LASERS FOR SEE TESTING IN ELECTRONICS FOR SPACE

2.1 Introduction

Before sending electronic systems to space, their SEE response is characterized using particles that are representative of the radiation environment in which they will operate. Using particle accelerators for this qualification process can be expensive, and limited availability to these facilities can result in project delays. For several decades, pulsed lasers have been used as a tool to inject localized carriers into semiconductor devices as a means to probe various single-event effects in devices, circuits, and systems. Pulsed-laser single-event effects (PL-SEE) testing has augmented the results obtained in broad-beam accelerator testing by providing engineers and scientists with data that can be used to better understand the phenomena observed during beam experiments. Such results are useful since they can quickly narrow down the specific cause of a given component's single-event sensitivity, thereby yielding both schedule and budgetary benefits for many space missions.

Due to the inherent differences in the dosimetry of heavy-ion and laser sources, most of the results obtained through PL-SEE testing often are qualitative in nature. Since the inception of PL-SEE techniques, researchers have sought to obtain quantitative agreement between heavy-ion- and laser-induced measurements. This effort has resulted in some success for single-photon absorption (SPA) processes, where empirical correlation factors have been derived for several platforms [51, 55, 63, 64]. Correlation factors derived from such investigations have been used to accurately predict SEL and SEU thresholds (i.e., the LET at which a device will either latch or

upset) in a range of technologies.

For recent-generation, highly-scaled technologies with increased densities of metal traces, it has become difficult to employ topside SPA for SEE testing since the metal layers can block, or interfere with, the incident beam. As a solution to overcome the issues with topside testing, backside excitation has been leveraged for many years by careful selection of wavelength for SPA [79,80], or by exploiting two-photon absorption (TPA) processes [81]. In either case, the beam can propagate through the backside of the wafer, allowing the laser to penetrate into the sensitive volume unobstructed by metallization. Despite some successes with correlating heavy-ion and SPA charge generation through empirical factors, due to the increased complexities associated with carrier distributions generated by TPA, achieving a similar correlation for TPA is challenging and remains a topic of active research [65, 66]. Thus, the work in this chapter will focus on TPA PL-SEE testing.

In recent years, several studies have focused on determining ways to correlate TPA pulsed-laser results with charged particle data [5, 45, 51, 55, 63–66, 82, 83]. However, given the large number of variables associated with this problem, there are still several open questions that must be addressed. Achieving quantitative correlation between transient data produced from these two vastly different sources would alleviate some of the previously mentioned challenges with component qualification for space applications.

In this chapter, two different approaches to correlating ion and laser data in SiGe HBTs are shown. The first approach involves optimizing the parameters of the experimental setup at a laser facility to better reproduce the transients generated by heavy ions. The second approach involves using a novel charge deposition technique using a different optical setup than what has traditionally been used in the past.

2.2 Optimizing Optical Parameters to Correlate Ion and Laser Data

The primary goal of this section is to provide a general framework for optimizing laser parameters during a TPA PL-SEE experiment, such that one can quantitatively reproduce the heavy-ion-induced transients that could be encountered in a radiation environment (e.g., space). This is achieved by extracting certain "features" from measured heavy-ion-induced SETs, and then using an optimization routine to minimize the error between the waveforms resulting from ion and laser testing. PL-SEE provides an experimentally-accessible method for generating a wide variety of SETs, enabling this error minimization. Modifying certain laser parameters manifests in different TPA-induced carrier distributions which, in turn, gives rise to different SETs. As a result, this approach is shown to successfully identify an "optical geometry" with pulse energy as a free parameter that can then be used to reproduce heavy-ion data for a range of LETs in advanced SiGe HBTs. While the results shown in the present section are specific to SiGe HBTs, the presented framework does not assume a specific technology. Therefore, the overall approach of "feature matching" can be applied to other semiconductor technologies, based on Si and III-V materials, to attempt quantitative correlation of transients resulting from heavy-ion and pulsed laser testing.

2.2.1 Heavy-Ion and Laser Charge Deposition

In the context of heavy-ion testing, LET is defined as the deposited charge per unit length in a given material. The collected charge due to an SEE is obtained from integrating the transient current over time, and is directly related to the amount of deposited charge in the material [84]. For heavy-ion testing, several combinations of ions and energies can be used to obtain the same surface LET in silicon. As an example, Fig. 3 shows the surface LET in silicon, simulated using SRIM [85] for two

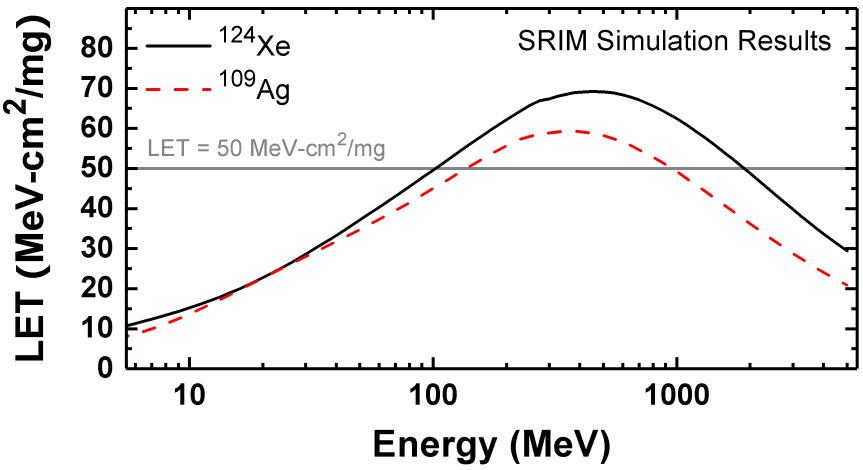

Fig. 3: Simulated linear energy transfer in silicon as a function of ion energy for two different ions.

different ions as a function of ion energy. The simulations show that there are four possible conditions to obtain a surface LET = 50 MeV-cm^2/mg. These conditions, however, will result in different ion ranges and radial energy distribution profiles (i.e., different charge deposition profiles).

Similarly, several combinations of laser conditions (e.g., spot size, wavelength, energy, and pulse duration), referred to in this section as "optical geometries," can result in the same deposited charge within the sensitive volume of a device; this is referred to as the laser-equivalent LET (LE-LET) due to its analogy with heavy-ion LET [86]. This concept is illustrated in Fig. 4, where the deposited charge due to TPA is plotted as a function of laser pulse energy for multiple focused spot sizes. These curves were calculated using analytical expressions from the literature [65] that have been verified using NLOBPM [87]. For these calculations, the sensitive volume thickness was chosen to be 60 μm and the laser focus was placed at Z_{foc} = 30 μm (i.e., in the center of the sensitive volume). In Fig. 4, and in the discussion below, the reported focused spot sizes, ω_0, are measured as the radial distance between the point of maximum intensity and the point where the intensity equals $1/e^2 = 0.135$ times the maximum value. This measurement is also known as the half width at the

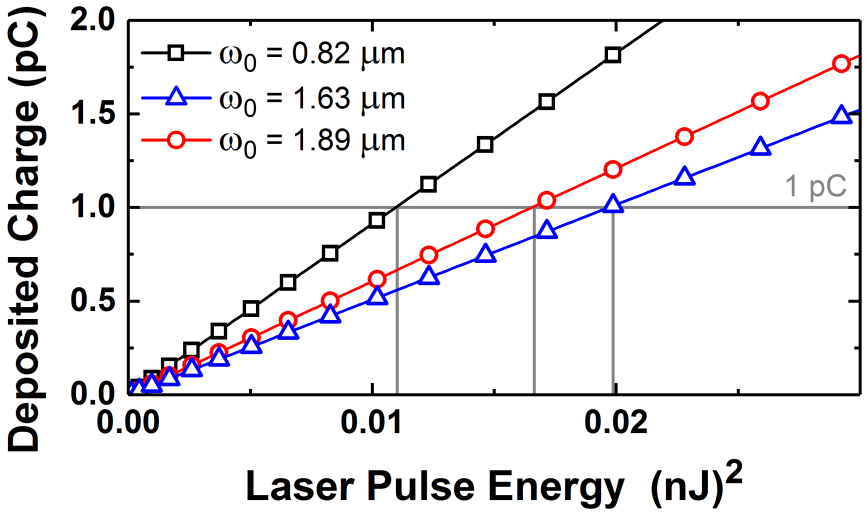

Fig. 4: Calculated deposited charge in a sensitive volume that is 60 μm thick as a function of laser energy for multiple focused spot sizes (ω_0). The laser is focused at a depth of Z_{foc} = 30 μm. The values for focused spot size are taken to be the half width measured at the $1/e^2$ point.

$1/e^2$ point (HW$1/e^2$).

The spatial distribution of carriers generated from an incident ion, also known as the charge deposition profile, will depend on the ion's energy and mass, as well as the target material. For carriers generated from a pulsed laser, the charge deposition profile depends on the wavelength, the focused spot size, the laser pulse energy, and the target material. In addition, for TPA-induced generation, the charge deposition profile will also depend on the pulse width. Wavelength and pulse width are typically fixed by the laser source and may not be easily tunable during an experiment. The focused spot size is often fixed by the optical setup but may be adjusted, although it is usually kept at the minimum achievable value to maximize spatial resolution in position-dependent measurements. Finally, the pulse energy is usually the primary experimental variable since it is typically the easiest to change.

An obvious solution to enable correlation of SETs from these two fundamentally different sources would be to recreate heavy-ion charge deposition profiles using a laser. However, heavy ions used for SEE testing typically have a long range, and the

radial distribution of the resulting charge deposition is typically confined to several hundred nanometers. For a focused laser beam, the minimum achievable radial spot size is determined by the wavelength, the refractive index of the material, and the focusing geometry. The axial distribution, which is given by the Rayleigh range for a Gaussian laser beam, is proportional to the square of the spot size. Thus, an inherent tradeoff exists between matching the axial and radial components of a laser-induced charge deposition profile to that of a heavy ion when using a focused beam. This tradeoff can be observed in Fig. 5, where simulated charge deposition profiles for various optical geometries are compared to that of a heavy ion. Note that due to the rapid decrease in the charge density of the heavy-ion data, the logarithm of the data is plotted, further illustrating the differences between these two sources.

Due to the intrinsic dependence of the spot size (radial component) and the Rayleigh range (axial component) of a Gaussian laser beam, it is not feasible to recreate the charge deposition profile of a heavy ion. Thus, the goal for correlating SETs from these different sources is to find different charge deposition profiles for each source that would result in the same measured waveform, which is after all, typically what one cares most about at the device and circuit level. A method for identifying these charge deposition profiles and the associated optical geometries is described below.

2.2.2 Optical Parameter Optimization via Feature Matching

In the context of this research, a "feature" is defined as a measurable or calculated property of an SET. For the SETs measured in SiGe HBTs, several features have been identified in an attempt to fully describe the waveform, including: transient peak amplitude, transient full-width-at-half-maximum (FWHM), plateau height, transient duration, and collected charge. These features are illustrated in Fig. 6, where a representative heavy-ion-induced transient is used as an example. The mechanisms

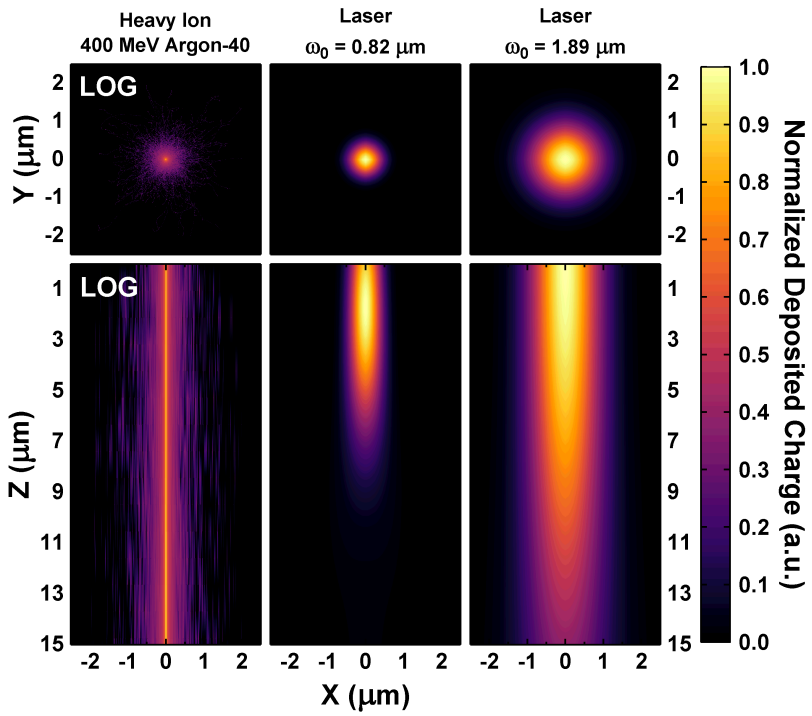

Fig. 5: Comparison of charge deposition profiles for (left) a 400 MeV ^{40}Ar ion, (center) focused laser with a 0.82 μm (HW1/e^2) focused spot size, and (right) focused laser with a 1.89 μm (HW1/e^2) focused spot size. Note that due to the rapid decrease in the radial charge density of the heavy-ion data, the logarithm of the data is plotted instead.

of charge collection for SiGe HBTs are described in detail elsewhere [70, 88–91]. Two distinct components in these transients can be identified. The first, is a sharp, narrow transient response that results from the ion-shunt effect, the relevant characteristic of which is described by the transient peak amplitude. The second component is an extended "tail" that results from delayed charge collection due to carrier diffusion. This component is characterized by the collected charge, the plateau height, and the transient duration.

Although some of these features are highly-correlated (e.g., higher transient peak typically leads to larger collected charge), their dependence on charge deposition profiles can vary significantly. Therefore, attempting to correlate laser and ion data using only a single feature generally leads to less than optimal results. An attempt to use single-feature laser/ion correlation is shown in Fig. 7, for which, by only adjusting

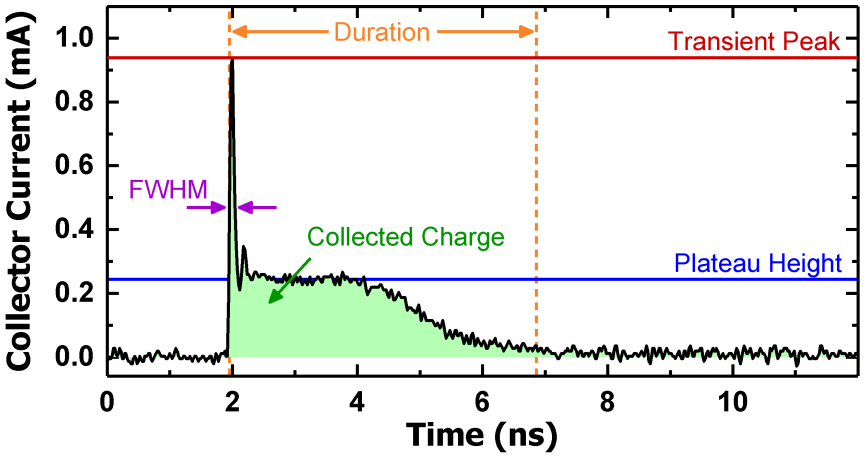

Fig. 6: Representative collector current transient taken from an emitter-centered strike of a 400-MeV, ^{40}Ar ion (LET = 10.72 MeV-cm^2/mg). The main features of the heavy-ion-induced waveform are highlighted.

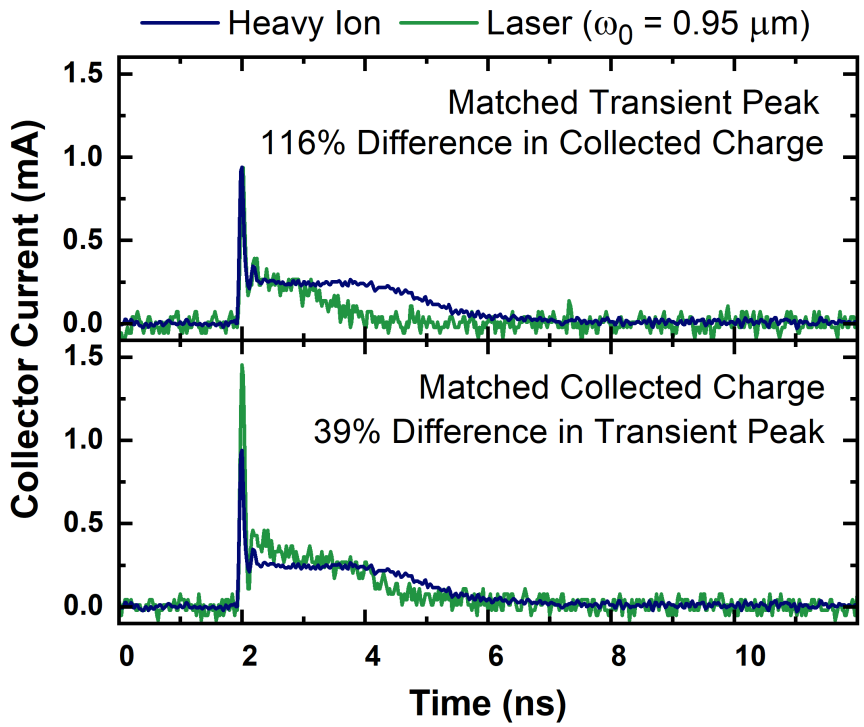

Fig. 7: Comparison of ion- and laser-induced transient for a laser focused spot size $\omega_0 = 0.95\ \mu m$ when (top) the transient peak is matched and (bottom) the collected charge is matched.

the laser pulse energy, laser transients are matched to either the transient peak amplitude or the collected charge of an ion transient. The data show that matching the transient peak amplitude alone results in a 116% difference in collected charge,

while matching only collected charge results in a 39% difference in transient peak amplitude. To achieve the desired waveform correlation, relevant features must be matched simultaneously.

Once relevant features have been identified in the heavy-ion dataset, the laser parameters can be swept experimentally to determine the optimal optical geometry required to correlate ion-induced and laser-induced waveforms. An example of how this may be achieved in practice is presented below.

2.2.3 Experimental Setup

Heavy-ion-induced transients were measured at the 88-inch cyclotron BASE Facility at Lawrence Berkeley National Laboratory (LBNL) using the 10-MeV/amu heavy-ion cocktail over a wide range of LETs. In addition, ion-induced transients were measured using the heavy-ion microbeam facility at the GSI Helmholtz Center for Heavy Ion Research [92]. The microbeam data obtained using calcium ions with an energy of 4.8 MeV/amu, contains information on the spatial dependence of the measured SETs and allows one to draw certain conclusions from the broadbeam data. A summary of the facilities and ions utilized in the present study is included in Table 1. The values reported for LET are taken from SRIM simulations at the silicon surface after the ion has passed through the oxides in the back-end-of-line (BEOL) layers.

Laser-induced transients were measured at the U. S. Naval Research Laboratory (NRL) using through-wafer TPA [81]. TPA carrier injection allows for time-resolved, position-dependent, three-dimensional measurements of SETs. The system features 150 fs, 1260 nm wavelength optical pulses at a repetition rate of 1 kHz, and is calibrated daily following the procedure described in [93]. The laser focused spot size was varied between 0.82 μm to 1.89 μm, measured at the $1/e^2$ point (HW1/e^2), by utilizing different microscope objective lenses and changing the beam size at the input aperture of each lens [93]. A summary of the optical geometries used in the present

Table 1: Summary of Experimental Conditions for Heavy-Ion Data Taken at LBNL for a 5AM SiGe HBT

Facility	LBNL					GSI
Ion	Ne	Ar		Xe		Ca
Z	10	18		54		20
A	22	40		124		48
Energy (MeV)	216.28	400.00		1232.55		230.40
Angle of Incidence	0	0	45	0	45	0
Surface LET (MeV-cm^2/mg)	3.79	10.72	15.93	64.85	95.59	20.68
Range (μm)	174.7	130.2	92.1	90.1	63.8	53.5
Flux (10^5 ions/cm^2·s)	8.00	7.00	6.70	1.20	1.43	—*
Eff. Fluence (10^8 ions/cm^2)	3.01	3.38	3.14	5.71	1.63	—*

* Data from GSI was collected by scanning an ion microbeam across the device multiple times with one ion strike per position.

investigation, along with the model number for each objective lens, is included in Table 2. The input beam size was measured using the traditional knife-edge technique and the focused spot size for each geometry was calculated using the expressions derived by Urey [94]. This approach for determining the size of the focused beam has been previously verified [93]. Measurements were taken for several laser pulse energies. The energies reported in this section are the energies incident on the backside of the sample (i.e., no corrections have been made to account for reflection losses in the silicon/air interface). During these experiments, the laser was focused on the X-Y-Z coordinate that resulted in the largest collected charge in the SiGe HBT.

For each experiment, the samples were attached and wirebonded to a custom-designed, high-speed printed circuit board (PCB). The front of the die is left uncovered to allow for topside heavy-ion testing, while a small circular aperture in the PCB

Table 2: Summary of Optical Geometries Utilized for Laser Testing at NRL for a 5AM SiGe HBT

Objective Lens Model	Input Beam Size (mm)	Focused Spot Size (μm)
Mitutoyo LCD Plan Apo NIR 100× LWD	2.1	0.82
	1.05	0.95
Mitutoyo M Plan Apo NIR 50×	2.1	1.27
	1.05	1.63
Mitutoyo M Plan Apo NIR 20×	2.1	1.89

exposes the backside of the die for TPA pulsed-laser testing. The board uses coplanar waveguides to deliver the signals from the wire bonds to Southwest Microwave SMA end-launch connectors. At NRL and LBNL, the induced SETs were captured using a Tektronix DPO71254, which is a 12.5-GHz bandwidth, real-time oscilloscope capable of capturing data at 50 GS/sec. At GSI, SETs were captured using a Tektronix TDS6154, which is a 16-GHz bandwidth, real-time oscilloscope capable of capturing data at 40 GS/sec.

The samples used in the present study are *npn* SiGe HBTs fabricated using GlobalFoundries' 5AM SiGe BiCMOS platform. These devices were selected because they are an attractive solution for both on-orbit and terrestrial extreme environments requiring high-performance analog, high-frequency RF, and highly-integrated digital circuitry on a single die. In addition, a large body of publications—a summary of which can be found in [27]— has resulted from studying the radiation response of devices in this particular platform. The emitter stripe of the selected device has an area of 0.5×10 μm^2. All transients were captured with all terminals of the device grounded, unless otherwise specified.

2.2.4 Experimental Results

2.2.4.1 Feature Dependence on Optical Parameters

All measured transients were processed using a custom feature extraction algorithm that uses simple waveform analysis techniques. The values for the collected charge, transient peak amplitude, plateau height, transient duration, and transient FWHM were extracted for each measured transient, as a function of spot size and laser pulse energy. The first step in the analysis is to remove features that are invariant with respect to the experimental parameters, or that contain redundant information (i.e., are highly correlated with other features). The transient FWHM was found to be invariant with changing spot size and laser pulse energy, and is not considered in this analysis. Unsurprisingly, the collected charge was found to be highly correlated with transient duration and plateau height. In this manner, the plateau height and collected charge, along with the transient peak amplitude, were selected for this analysis. Note that the transient duration could have been used in place of the plateau height or the collected charge. However, the latter were chosen due to the simplicity in their extraction from time-domain data.

For the following discussion, a worst-case heavy-ion-induced transient was selected from the recorded ^{40}Ar strikes (LET = 10.72 MeV-cm^2/mg) to compare with laser data. The worst-case transient was chosen based only on the transient peak amplitude, since laser and microbeam data have shown that the largest peak in a SiGe HBT is obtained when the ion passes through the center of the emitter-base-collector stack (i.e., center of the intrinsic device). For this heavy-ion transient, the collected charge, transient peak amplitude, and plateau height were extracted to be 1.06 pC, 0.978 mA and 0.24 mA, respectively.

The features extracted from the laser data are shown in Fig. 8. Each feature is plotted as a function of focused spot size and the square of the laser pulse energy (the latter is necessary due to the TPA mechanism [65]). A surface fit is included to

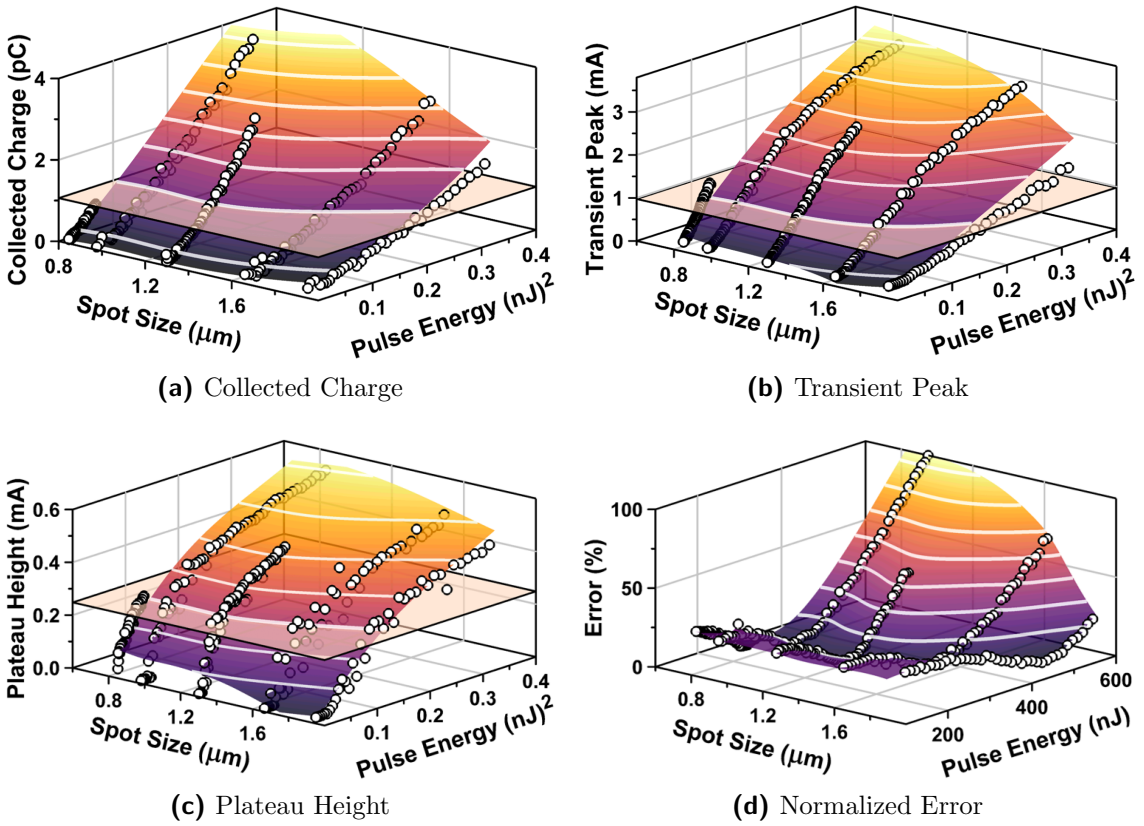

(a) Collected Charge **(b)** Transient Peak

(c) Plateau Height **(d)** Normalized Error

Fig. 8: Extracted (a) collected charge, (b) transient peaks, and (c) plateau heights for laser-induced transients measured as a function of different focused spot sizes and energies. A surface fit has been included to guide the eye. The semi-transparent horizontal plane shows the optimal value for each feature to match a worst-case, heavy-ion SET for an ^{40}Ar strike (LET = 10.72 MeV-cm^2/mg). The normalized error resulting from comparing features extracted from laser-induced transients to the worst-case, heavy-ion SET is shown in (d). A minimum error is achieved for a spot size of 1.89 μm and a pulse energy of 483 pJ.

guide the eye. The semi-transparent horizontal plane shows the value of each feature corresponding to the worst-case ion transient, and is the target value for each feature extracted from the laser data. This means that the data points that lie on the plane represent the set of laser conditions that will match a given feature extracted from a heavy-ion waveform.

The collected charge, shown in Fig. 8(a), is found to increase with increasing laser pulse energy for a fixed spot size, and decrease with increasing spot size for a given pulse energy. These results are expected, since the amount of charge generated by TPA is proportional to the square of the pulse energy, and roughly inversely

proportional to the square of the focused spot size [65]. The transient peaks, shown in Fig. 8(b), have a similar dependence on spot size and energy as the collected charge. The plateau heights, shown in Fig. 8(c), were found to increase with increasing pulse energy (for a fixed spot size), but were found to be only weakly dependent on spot size (for a fixed pulse energy). Note that there exist several laser conditions that allow for individual laser-induced waveform features to be matched to certain features of ion-induced transients. However, the pitfalls of considering only individual features are discussed above: it results in poor matching of the remaining features. Thus, to quantitatively match the entire ion/laser waveforms, all features must be matched, within acceptable error bounds, by using the same set of optical parameters.

2.2.4.2 Feature Matching by Error Minimization

To find simultaneous laser conditions that match heavy-ion transient features, a difference error for each feature was determined. The total error was calculated as an equal-weight sum of the magnitude of the individual error values. The total error was normalized, and is shown as a function of spot size and laser pulse energy in Fig. 8(d) for the worst-case ^{40}Ar strike previously described. A minimum error is achieved for a spot size of 1.89 μm and a pulse energy of 483 pJ.

A similar analysis was performed for several other worst-case ion-induced transients and a common optimum spot size of 1.89 μm resulted in the minimum error. This result suggests that, for a given optimized optical geometry (i.e., wavelength, spot size, and pulse width), the laser pulse energy can be adjusted to achieve various equivalent LET values.

The laser-induced collector transients obtained with these optimized laser conditions are compared to the heavy-ion waveforms in Fig. 9. Observe that excellent agreement is obtained between ion and laser waveforms for a range of LETs. Fig. 10 compares laser and ion transients for the collector, base, and substrate terminals

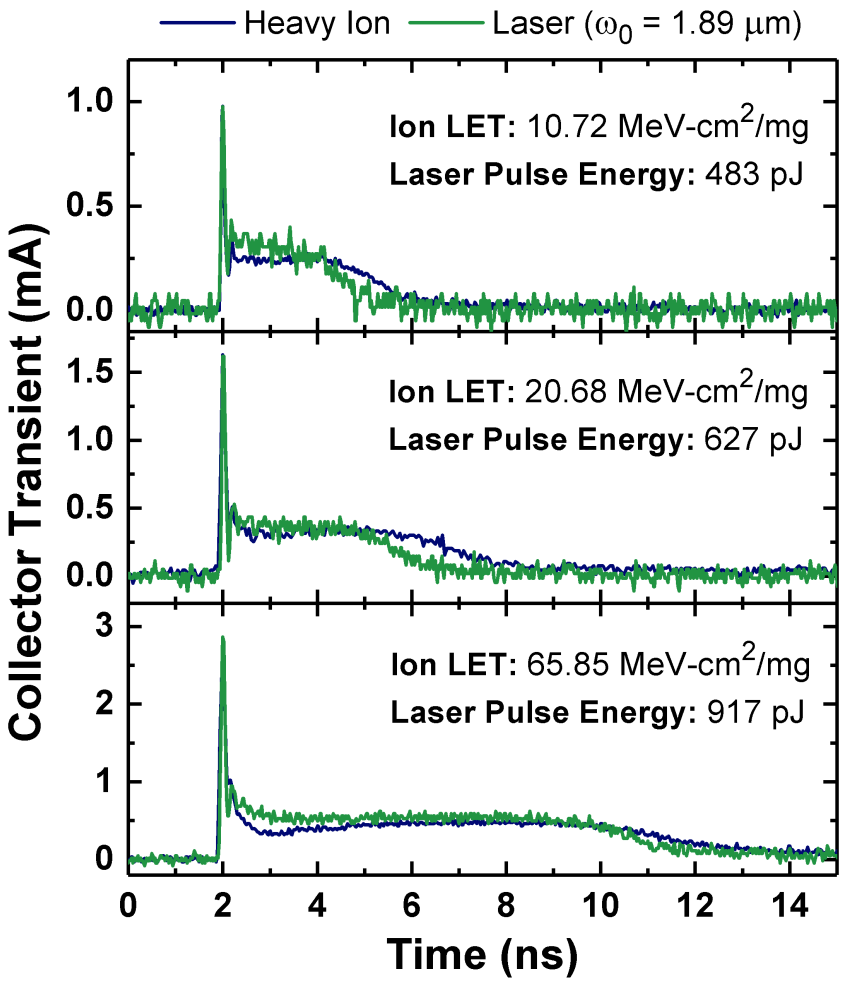

Fig. 9: Comparison of heavy-ion- and laser-induced single-event transients for multiple heavy-ion LETs and laser pulse energies.

when the device is biased at $V_C = V_B = 0.8$ V, $V_E = V_{Sub} = 0$ V, again showing good agreement between the two sources. It was not possible to monitor the emitter transient during laser testing since the fourth channel on the oscilloscope was utilized to measure the laser pulse energy by recording the response of a linear photodiode [93].

Overall, the waveforms induced with the optimized laser conditions show excellent agreement with the heavy-ion data for a variety of experimental conditions. Note that the best agreement is obtained for the largest spot size considered in the present study, which suggests that performing TPA PL-SEE testing with the smallest achievable spot size may not be the optimal approach if the goal is to obtain quantitative information

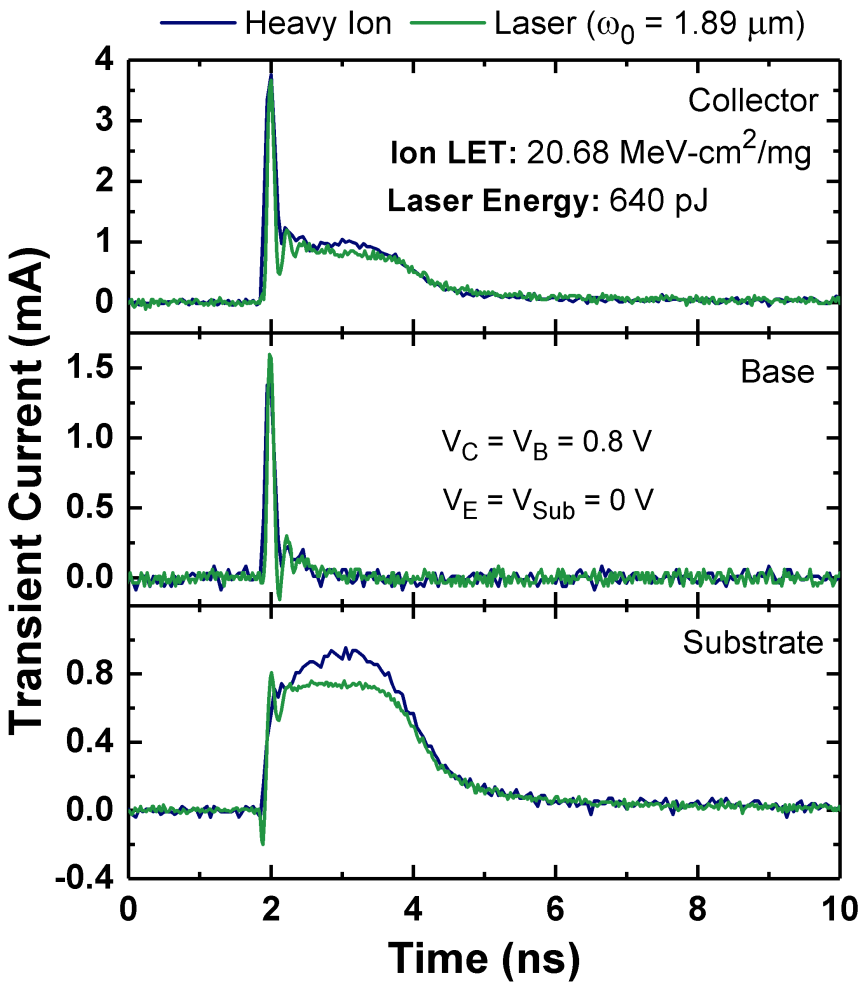

Fig. 10: Comparison of heavy-ion- and laser-induced single-event transients for the collector, base and substrate terminal when the device is biased at $V_C = V_B = 0.8$ V, $V_E = V_{Sub} = 0$ V.

about ion-induced transients (at least for the 5AM SiGe HBT utilized in the present study). The improved matching to ion-induced waveforms for this bulk device is a result of the larger spot size generating longer track lengths, which enable an elongated vertical charge deposition that better resembles that of a heavy-ion strike in the axial direction. Furthermore, these results confirm that it is not necessary to match the carrier distribution of a heavy ion in order to induce equivalent transients.

This correlation can be achieved due to the dependence of certain features on different characteristics of the induced charge deposition profile. For example, while the transient peak amplitude depends on the peak concentration of induced carriers,

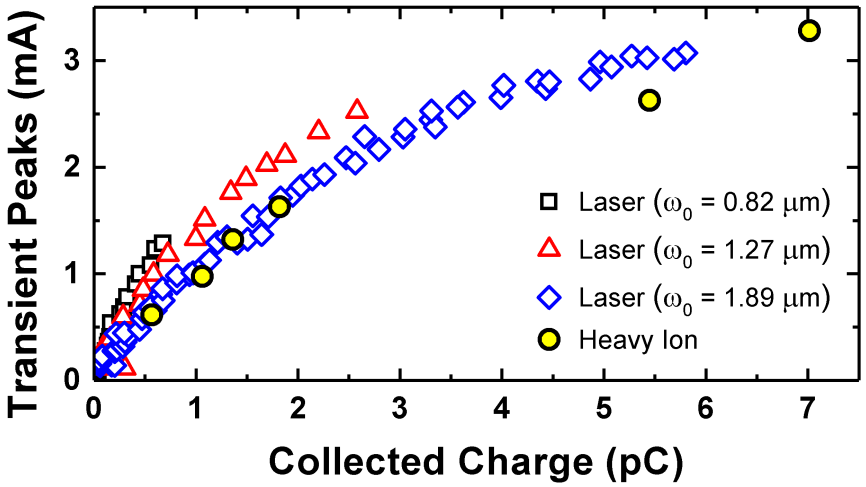

Fig. 11: Collector transient peaks as a function of collected charge for heavy-ion- and laser-induced transients. Multiple laser spot sizes are shown for comparison. Best agreement is obtained for a laser spot size $\omega_0 = 1.89\ \mu m$.

the collected charge depends on the deposited charge, or the total amount of induced carriers. For a Gaussian laser beam, one can lower the peak carrier concentration while maintaining the same amount of charge by increasing the focused spot size. This is illustrated in Fig. 11, where the transient peak amplitude is plotted as a function of collected charge for heavy-ion data and multiple laser spot sizes. The data show that as the laser spot size is increased, for a fixed collected charge, the transient peak amplitude is reduced. Furthermore, the relationship between collected charge and transient peak amplitude for the heavy-ion dataset is best reproduced by the laser when the spot size is 1.89 μm. This result is an indicator that simultaneously matching multiple features between ion and laser datasets leads to improved waveform correlation when compared to single-feature matching approaches.

2.2.5 Discussion

2.2.5.1 Estimation of Equivalent LET

After finding the optical geometry that best reproduces the relationship between the transient peaks and collected charge of ion-induced transients, laser pulse energy is

the only free experimental parameter. Therefore, pulse energy can be empirically correlated with heavy-ion LET. Fig. 12 shows LET values used in heavy-ion experiments, calculated using SRIM, as a function of the laser pulse energy that best reproduces the ion-induced transient. Note that the abscissa shows the square of pulse energy due to the non-linear dependence of deposited charge on laser pulse energy. The vertical error bars are obtained from the maximum expected variations in LET due to the possibility of an ion traversing different materials in the BEOL and have been obtained from SRIM simulations. The horizontal error bars represent the uncertainty in determining the laser pulse energy (± 5%). The red dashed line in Fig. 12 is a linear fit to the experimental data. From this fit, the equivalent LET can be obtained from the experimental laser pulse energy by,

$$LET = 70.2 \times (PE)^2 - 5.2 \tag{1}$$

where the pulse energy, PE, is given in nJ and LET is given in MeV-cm^2/mg.

Note that, although limited data are available, the data point for the biased case is well-aligned with the grounded data points. This suggests that the same empirical fit could potentially be used across a wide range of bias voltages and at the circuit level, which is clearly advantageous.

A recent study by Hales *et al.* [66], applied the concept of LE-LET in order to correlate collected charge generated by pulsed-laser and heavy-ion excitation in a bulk diode. Using this approach, good laser-ion correlation was achieved for a variety of optical geometries for both single-photon absorption and TPA. One of the advantages of the LE-LET approach is that it does not require significant amounts of data to estimate an equivalent LET. The sensitive volume of this bulk diode is much larger than the carrier distribution profile generated by the laser. The devices utilized in the present investigation, however, have a sensitive volume that is comparable in size to the TPA-induced carrier distribution profile, which is part of the reason why changing the spot size significantly changes the transient shape. Thus, applying the

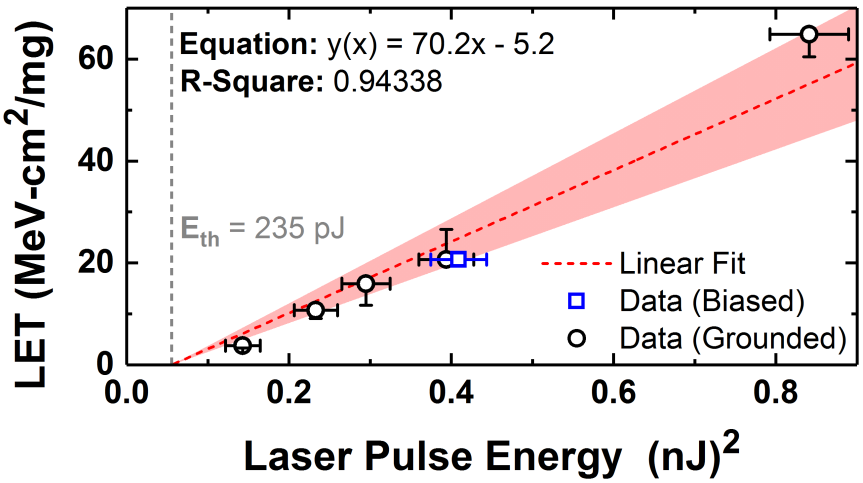

Fig. 12: LET used in experiment as a function of the pulse energy required to minimize the error between the respective ion and laser transients. The square of the pulse energy is plotted to account for the non-linear generation process. The red dashed line shows a linear fit to the data when the intercept on the abscissa is set to $E_{th} = 235$ pJ. The red shaded region shows the 95% confidence interval of the linear fit.

LE-LET approach by itself would not be sufficient to achieve good correlation for the SiGe HBT investigated in the present section. Further work needs to be completed to extend the LE-LET approach to devices with a sensitive volume that is comparable in size to a TPA carrier distribution profile.

Finally, note that the fit does not pass through the origin. There are two potential reasons for a non-zero intercept: 1) the correlation between heavy-ion LET and laser pulse energy may not hold at low LET values, and 2) the carrier densities generated at low laser pulse energies are not sufficient to result in a measurable transient. The first statement could not be verified due to the lack of data at lower LETs. However, the laser data show an apparent threshold energy below which no transient was measured above the noise floor, as shown in Fig. 13. This observation supports the second statement. Thus, this threshold energy, E_{th}, was used to fix the intercept in the empirical fit.

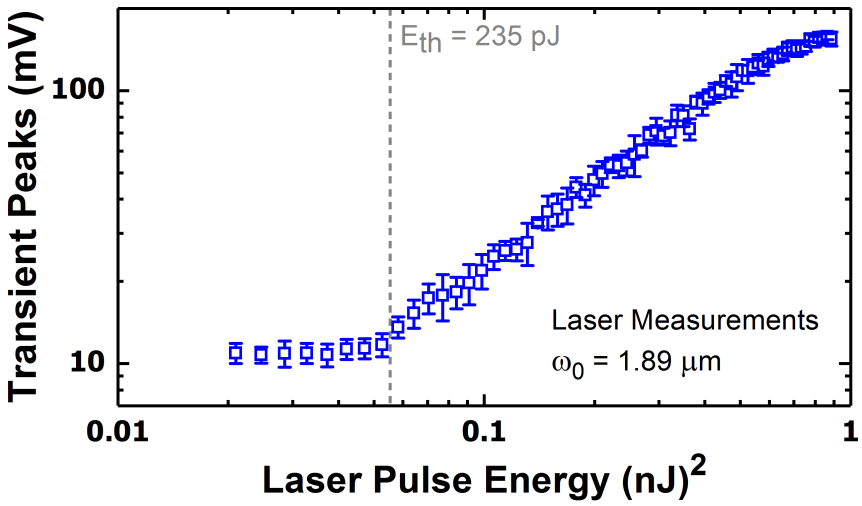

Fig. 13: Transient peak amplitude as a function of laser pulse energy squared. The data show that below a pulse energy $E_{th} = 235$ pJ, there is no measurable transient. This energy threshold was used as the intercept in the fit shown in Fig. 12.

2.2.5.2 Limitations of the Presented Approach

Although the presented feature matching approach is independent of technology or process, the obtained empirical relationship between heavy-ion LET and laser pulse energy is not. The results shown in the present study only apply to 5AM SiGe HBTs of a specific geometry. Achieving this correlation requires a lot of laser and heavy-ion data to identify the most appropriate optical parameters for testing. Once identified, however, one may continue to utilize these parameters for different circuits without requiring additional heavy-ion data. Furthermore, with a well-calibrated TCAD model and the use of simulation tools such as NLOBPM, Geant4, and Synposys Sentaurus, the optimal laser parameters could potentially be extracted from simulation results, reducing the amount of data needed to apply this approach.

An additional limitation is the increase of the laser spot size for improved correlation between ion and laser data. Typically, PL-SEE testing setups will focus the spot size to the smallest possible value, close to the spatial resolution limit of the optical setup. Having a small spot size is obviously desirable, as it affords experimenters the capability of performing high-resolution spatial scans. These scans can be

very useful for identifying sensitive junctions and evaluating specific implementations of RHBD approaches. Although increasing the spot size may not be an option for highly-integrated digital systems, this is not the case for high-performance analog and RF systems. For analog and mixed-signal circuits (e.g., amplifiers, comparators, and power switches) larger devices are typically used to enable higher gain and support larger currents without compromising device reliability. In the case of CMOS-based RF systems, opting for highly-scaled platforms could result in performance penalties due to losses in the device interconnects required to interface the circuit with the rest of the system [95]. The device geometry used in the present study is relevant in the context of analog and RF applications and can be used to design high-performance RF circuits. Although less of a concern for large devices, the effect of spot size on spatial resolution must still be considered.

To investigate any potential drawbacks of using an increased spot size with the selected sample, the laser was scanned across the device and the transients were measured as a function of position for multiple laser spot sizes. These results are compared to similar measurements performed using the microbeam at GSI in Fig. 14, which serves as a baseline for achievable resolution. The uncertainty in ion strike location for the microbeam is approximately 500 nm. The data show that, for the particular device used in the present study, doubling the laser spot size does not significantly compromise the resolution of spatial data. Thus, loss of scanning resolution should not be a concern for devices that would be utilized to design analog and RF circuits. In addition, Fig. 14 shows that the transient peaks quickly reduce to zero outside of the deep trench isolation, which indicates that charge sharing, a concern for highly-scaled CMOS processes, is not an issue for this SiGe platform.

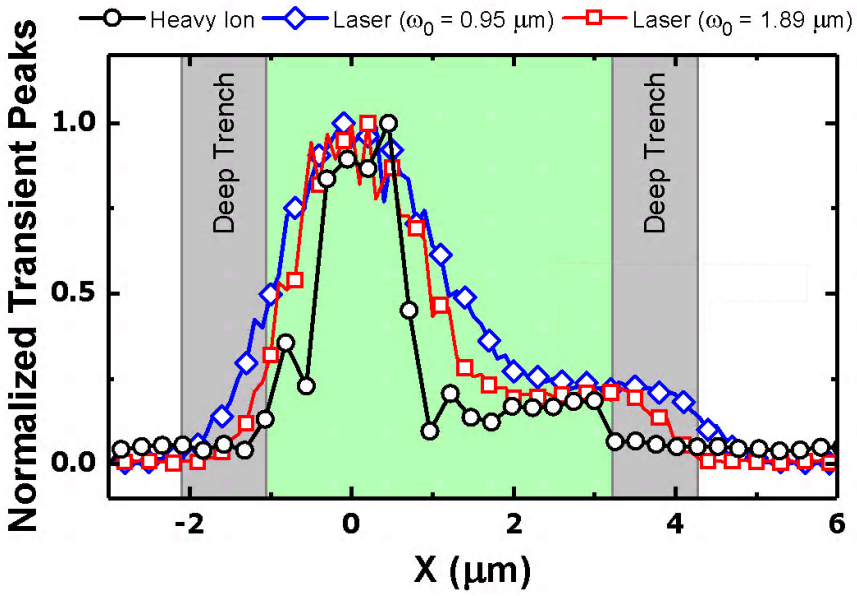

Fig. 14: Comparison of spatial dependence of transient peaks for ion- and laser-induced transients. The uncertainty in ion strike location is 500 nm. The emitter stripe is centered around $X = 0$ μm. The green region highlights the dimensions of the active area in the device, while the grey regions represent the dimensions of the deep trench isolation. Note that the increased spot size that results in improved agreement with heavy-ion data does not significantly compromise the resolution of spatial data for the 5AM SiGe HBT.

2.2.5.3 Applicability to Other Technologies

The presented framework for obtaining waveform correlation between ion- and laser-induced transients relies on feature extraction, dimensionality reduction (i.e., removing irrelevant features from the problem), and error minimization techniques. All of these techniques are independent of semiconductor process or technology. The purposeful generality of this approach allows for the analysis to be expanded to other platforms. Certainly, it can be expected that a different set of optical geometries will be obtained to correlate data for smaller device nodes or devices in a silicon-on-insulator platform, where the sensitive volume thickness is restricted by the buried oxide. Furthermore, in the present study, only focused spot size and laser pulse energy were considered in the analysis. These particular parameters were chosen because they are the most accessible for tuning by the experimenter. However, a similar

process could have been followed by varying the wavelength, or the pulse energy, or both. For the technology selected in the present section, tuning the focused spot size and pulse energy was enough to achieve excellent correlation between ion and laser data. For other technologies, more parameters may need to be considered, but the feature-matching approach would still be applicable to this optimization problem with higher parameter dimensionality.

There are a large number of technology-dependent factors that will affect the optical parameters required to achieve full waveform correlation and finding a global solution for all semiconductor processes may not prove feasible. However, similar to the existing catalogs containing radiation effects data for commercial electronic components, an analogous catalog or "library" could be assembled to include optical geometries for different semiconductor processes. Such a collection would provide experimenters with the necessary information to utilize laser systems to obtain data that is quantitatively representative of heavy-ion data.

2.3 Using Bessel Beams for Pulsed-Laser Testing in SiGe HBTs

One of the drawbacks of the previous framework is the necessary compromise in spatial resolution in laser testing to achieve correlation with ion data. More recently, a novel approach to generate carriers for PL-SEE testing has been introduced [82, 96]. This new method involves the use of a conical focusing element known as an "axicon," rather than a traditional spherical lens. The resulting beam is known as a quasi-Bessel beam (QBB), which has the same radial distribution over several hundreds of micrometers in the axial direction. In contrast to the more traditional Gaussian beam used for PL-SEE, the dimensions of the QBB in the axial and radial direction can be controlled independently. This property of the QBB is advantageous when attempting to mimic the charge deposition profile of heavy ions, which tend to be small in the radial direction and long in the axial direction (i.e., high aspect ratio). Although

QBBs are widely used in other fields, their recent introduction to the radiation effects community has generated significant interest.

In this section, QBBs are used to induce SETs in SiGe HBTs. The main goal of this section is to provide the first experimental results of SETs in SiGe HBTs induced using the new QBB technique, and to compare the transients resulting from QBBs to more conventional Gaussian beams. The results of this paper indicate a larger parameter space in PL-SEE testing and show how both Gaussian beams and QBBs can be leveraged for different needs. The scope of this summary is limited to SETs induced via TPA.

2.3.1 Experimental Setup

Laser-induced transients were measured at the U. S. Naval Research Laboratory (NRL) using the same setup described in Section 2.2.3.

For this specific experiment, the pulse width was approximately 150 fs, measured at its FWHM value. To generate the Gaussian beam, the beam size at the input to the focusing elements had a radius of approximately 1.95 mm, measured at the $1/e^2$ point (HW1/e^2). The laser was then focused using a 20× microscope objective, which resulted in a focused spot size of 2.1 μm at HW1/e^2 (calculated based on [94]). To generate the QBB, an experimental setup similar to [82, 96] was utilized. For this experiment, an axicon with $\alpha = 5^\circ$ and a lens with $f = 50$ mm were used in conjunction with the same 20× objective. The input beam into the focusing elements had a radius of approximately 1.15 mm at HW1/e^2. This setup resulted in a QBB with a focused spot size of approximately 1.6 μm at HW1/e^2 and an axial FWHM of 2.4 mm (both values calculated based on [96]). Due to the larger span of the QBB in the axial direction, the pulsed energies used to achieve transients with similar amplitudes are much larger than for the Gaussian beam, as will be shown throughout this section.

Table 3: Summary of Experimental Conditions for Heavy-Ion Data Taken at LBNL for an 8HP SiGe HBT

Ion	Ne	Ar	Cu	Kr	Ag	Xe
LET (MeV-cm^2/mg)	3.49	9.74	21.17	30.86	48.15	58.78
Range (μm)	174.6	130.1	108.0	109.9	90.0	90.0
Flux (10^5 ions/cm^2·s)	5.35	2.50	1.95	1.30	1.20	1.15
Eff. Fluence (10^8 ions/cm^2)	11.40	9.05	8.40	9.51	5.02	3.32
# of Events	474	463	401	462	412	473

The heavy-ion-induced transients were measured at the 88-inch cyclotron BASE Facility at Lawrence Berkeley National Laboratory using the 10-MeV/amu heavy-ion cocktail across multiple linear energy transfers (LETs) ranging from 3.49 MeV-cm^2/mg to 58.78 MeV-cm^2/mg. A table of the different experimental conditions is shown in Table 3.

For each experiment, the samples were attached and wirebonded to the same PCB described in Section 2.2.3. The induced SETs were captured using a Tektronix DPO71254, which is a 12.5-GHz bandwidth real-time oscilloscope capable of capturing data at 50 GS/sec.

All of the heavy-ion and laser data were generated in an *npn* SiGe HBT device structure fabricated using GlobalFoundries' 130-nm 8HP SiGe BiCMOS platform. The emitter stripe of the selected device has an area of 0.13×10 μm^2. All the data were taken with all terminals of the device grounded, unless specified otherwise.

2.3.2 Experimental Results

One of the advantages of using a QBB over a traditional Gaussian beam is the ability to obtain a large aspect ratio in the charge deposition profile (i.e., one that is both narrow in the radial direction and long in the axial direction). To explore the impact of these differences when characterizing the SET response of SiGe HBTs, each beam

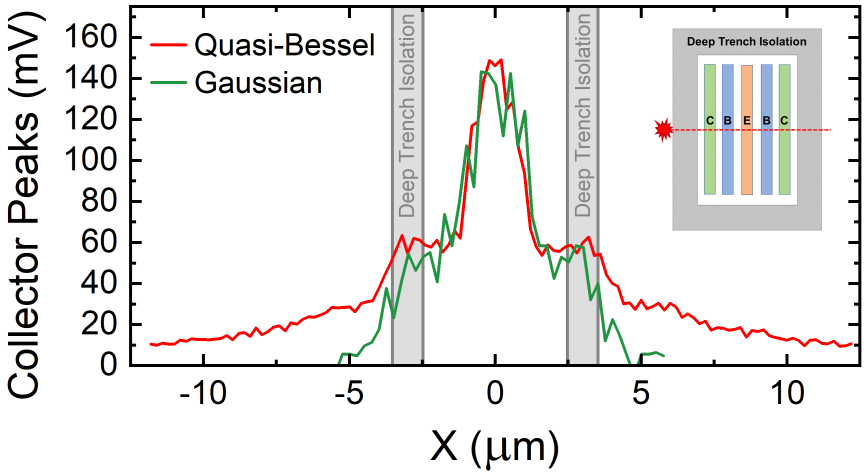

Fig. 15: Comparison of collector transient peaks as a function of position when the Gaussian and Quasi-Bessel beams are scanned across the device. The inset shows the position where the laser was scanned. The center of the emitter is placed at X = 0 μm.

was scanned across the device. Fig. 15 shows the peak amplitude of the transients measured at the collector terminal as a function of position for both the QBB and the Gaussian beam. The inset in Fig. 15 shows the direction of the scan. The grey bars show the location of the deep-trench isolation (DTI) regions. The data show a typical response for a SiGe HBT with a CBEBC layout configuration. The largest transient amplitudes were measured around the intrinsic device (i.e., the center of the emitter). The shoulders on either side of the maximum amplitude correspond to subcollector/substrate transients. The presence of measurable transients far away from the edge of the DTI for the QBB, despite its smaller spot size compared to the Gaussian beam, indicate that a much larger amount of charge is being deposited in the substrate. This excess charge then diffuses to the subcollector/substrate junction, where it is collected.

In the context of SEE testing, this excess charge outside the DTI would result in an artificially larger sensitive area for these SiGe HBTs. For this device, the physical area of the subcollector/substrate junction is $4.94 \times 10.98 = 54.24$ μm^2. Assuming that the sensitive area extends by the same amount in the Y direction, the measured

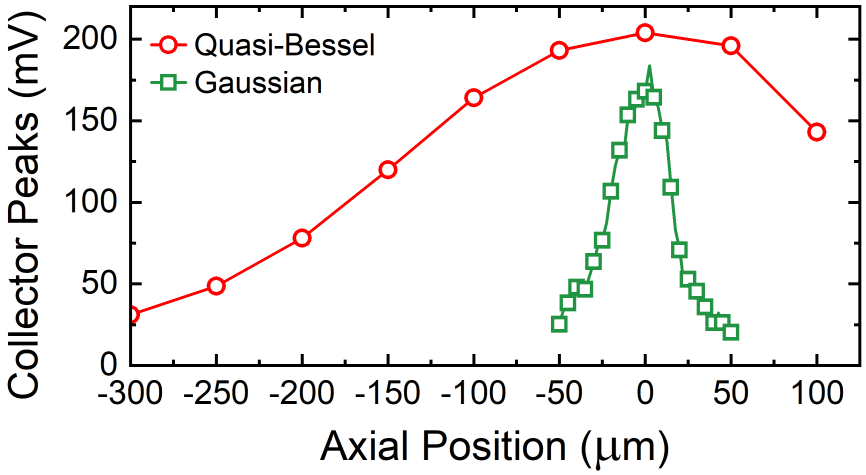

Fig. 16: Collector transient peaks as a function of axial position for the quasi-Bessel beam and the Gaussian beam. Note that the QBB has a much longer axial range compared to the Gaussian beam.

sensitive area with the QBB would be $> 520\ \mu m^2$ compared to $\approx 160\ \mu m^2$ for the Gaussian beam. As a point of comparison, the event cross-section can be calculated for the transients induced by a Xe ion, which have similar amplitudes, from Table 1 to be $\approx 142\ \mu m^2$. Thus, the excess charge generated by the QBB will result in a severely overestimated sensitive area for the devices or circuits being tested.

That excess charge is, however, a result of the long axial component of the QBB. Fig. 16 shows the transient peak amplitudes measured at the collector terminal as a function of axial position for both the QBB and the Gaussian beam. As expected, the data show that the QBB has a longer charge deposition profile in the axial direction compared to the Gaussian beam. This characteristic of the QBB is advantageous when testing a device or circuit that has junctions of different thicknesses. In this scenario, small changes in the axial position where the beam is focused might affect the measurement results. Having a beam profile that is slow-changing in the axial direction will remove these issues from the measurement.

Of primary interest are the resulting SETs induced by TPA using a QBB. Fig. 17 shows data for transients induced by TPA using both a QBB and a Gaussian beam, and by heavy ions. For each panel in Fig. 17, a representative transient from a

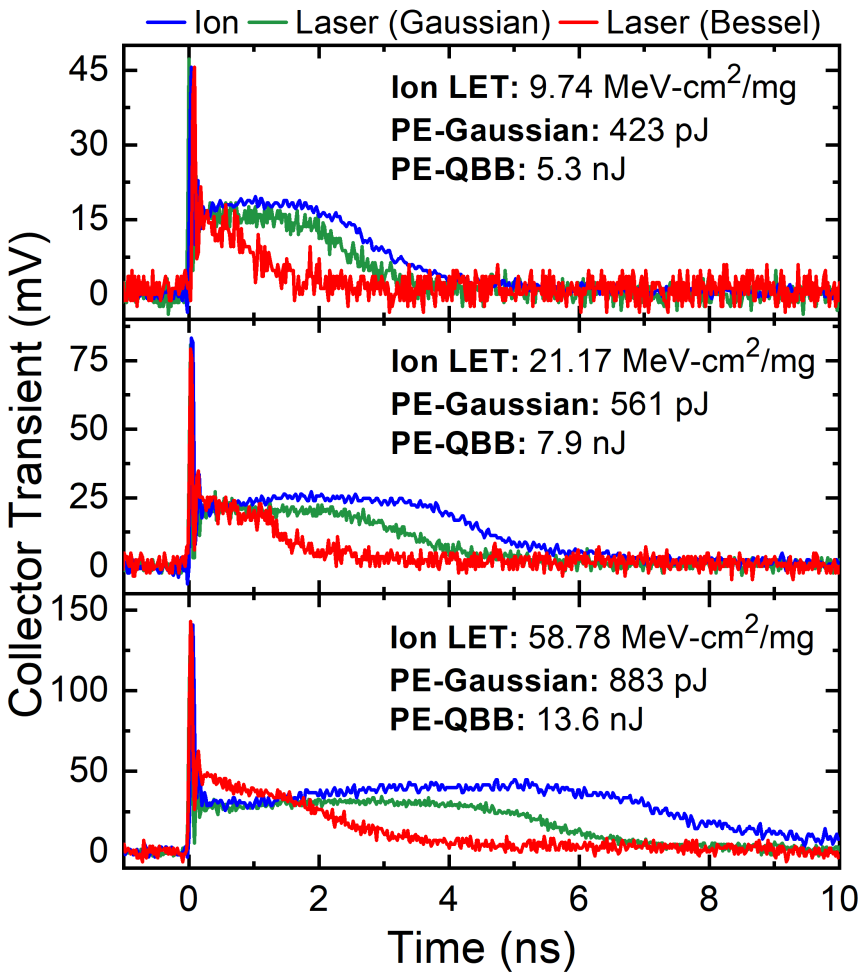

Fig. 17: Measured transients for a heavy ions, a Gaussian laser beam, and a quasi-Bessel laser beam for various ion LETs and laser pulse energies. The data for each panel were chosen based on matched transient amplitude.

heavy ion resulting from emitter-centered strikes (i.e., largest amplitudes) was chosen. Then, the laser pulse energy was tuned for each laser beam (i.e., the Gaussian and quasi-Bessel beams) until the transient amplitude matched the one for the heavy-ion data. Interestingly, despite the longer charge deposition profile and larger amount of deposited charge for the QBB, the transient duration is smaller when compared to an SET with the same amplitude produced by the Gaussian beam. For these transients, the slow diffusion tail will contribute to the bulk of the collected charge. A shorter transient duration would then lead to a smaller amount of collected charge. The differences in these transients will be further explored using TCAD simulations

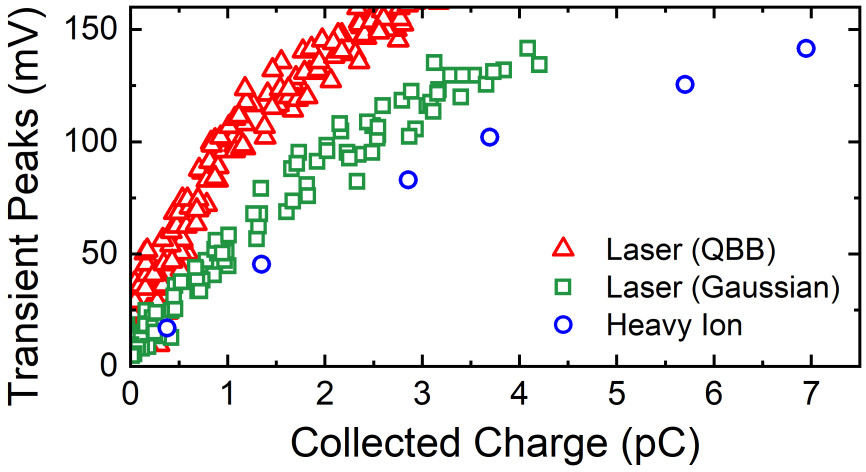

Fig. 18: Measured collector transient peaks as a function of collector collected charge for a Gaussian beam, a quasi-Bessel beam, and heavy ions.

below.

Given that the amplitudes of these transients are matched, the data in Fig. 17 suggest that the relationship between the transient amplitude and the collected charge is different between QBB and the Gaussian beam. This relationship is shown in Fig. 18, where the transient peak amplitudes of the collector terminal are plotted as a function of collected charge in the same terminal. The heavy-ion data is included for comparison. In the previous section, it was shown that this relationship between transient peak amplitude and collected charge in SiGe HBTs could be modified by changing the spot size of a Gaussian beam [5]. The data in Fig. 18 show that the Gaussian beam, which has the larger spot size, more closely reproduces the relationship between peaks and collected charge in the heavy-ion data. During this experiment, there was no attempt to optimize the spot sizes for either of the beams. A natural question results: Would changing the spot size of the QBB affect the relationship between the transient peak amplitude and the collected charge? The dependence of this relationship on spot size will be explored using TCAD simulations below.

2.3.3 TCAD Simulations

To further explore the differences in transient shapes between the QBB and the Gaussian beam, 2D TCAD simulations were performed using the Synopsys Sentaurus tool. For these simulations, the *dc* and *ac* characteristics of a 2D SiGe HBT model with a CBEBC layout were calibrated to those of the process design kit provided by the foundry. All terminals were grounded during the simulations to match the experimental conditions. The substrate thickness in simulation was 100 μm. The QBB was approximated by a heavy-ion track with a constant LET in the axial direction and a Gaussian profile in the radial direction, a fair representation for this particular geometry [96]. The Gaussian beam was modeled using the physical model interface of Sentaurus to implement the equations of a TPA Gaussian beam [65]. An example of the charge deposition profiles resulting from these simulations is shown in Fig. 19.

To verify the reason for the shorter transients when using the QBB compared to the Gaussian beam, an SET was simulated using the same spot sizes as the experiment. Fig. 20 shows the resulting electrostatic potential contours taken 0.1 ns after the time of peak charge deposition. For these simulations, the pulse energies were adjusted until the transient amplitudes were matched. These electrostatic potential contours show that the deposited charge deforms the potential in the substrate, creating a potential "funnel". These funnels can lead to faster charge collection by increasing the electric field around the charge track [97]. Note that the funnel for the QBB extends farther into the substrate than for the Gaussian beam, which would lead to faster charge collection and a shorter transient response. These simulation results support our conclusions regarding the experimental data.

One of the key results from the experimental data was that the relationship between the transient peak amplitudes and the collected charge is important, as shown in the previous section. To see whether this relationship can be altered by changing the spot size of the QBB, the spot size and pulse energy of both beams were swept

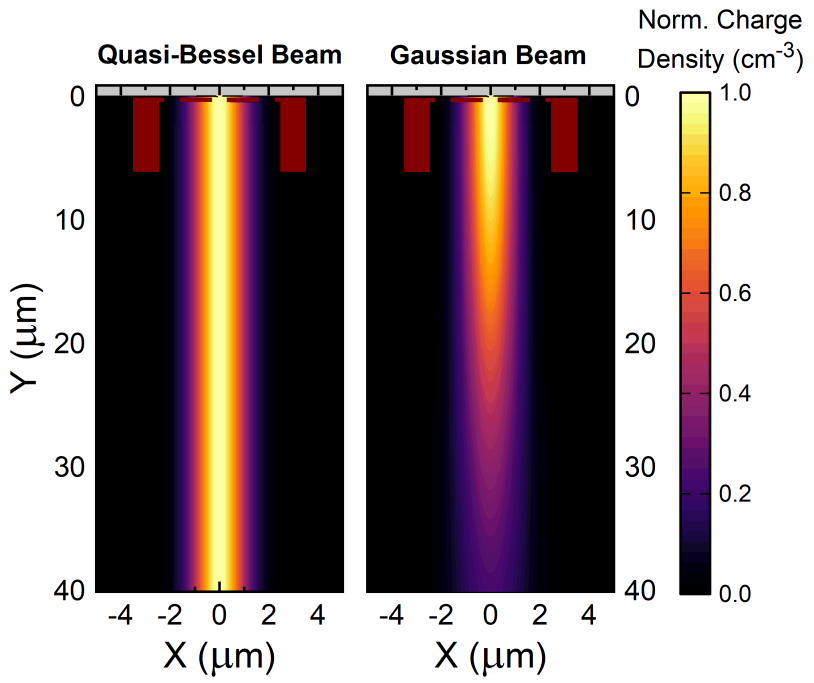

Fig. 19: Comparison of simulated charge density profile for a quasi-Bessel beam (left) and a Gaussian beam (right).

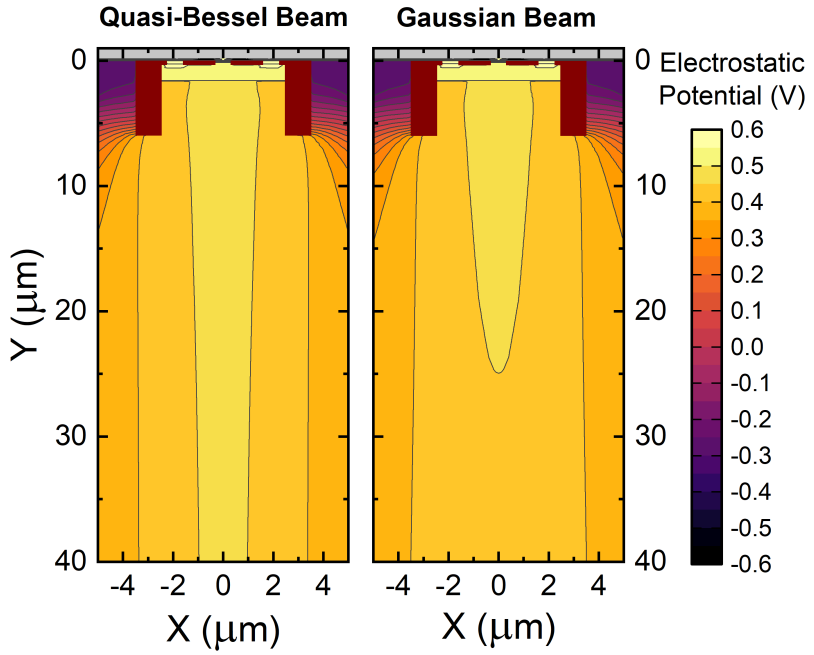

Fig. 20: Comparison of simulated electrostatic potential contours after 0.1 ns of peak charge deposition for a Quasi-Bessel beam (left) and a Gaussian beam (right). The contours shown are for charge deposition profiles that result in SETs of the same amplitude.

in TCAD. The transient peak amplitudes are plotted as a function of their corresponding collected charge for the Gaussian beam and the QBB in Figs. 21 and 22, respectively. First, the simulations reproduce the experimental trends previously observed for Gaussian beams. When the spot size is increased, the collected charge of a transient for a given peak amplitude also increases. The ability to modify this relationship by changing the spot size stems from the fact that the collector peak amplitude and the collected charge in SiGe HBTs are a result of carriers interacting with different locations in the device. The transient peak is generated when the intrinsic device is shunted by the excess carriers, while the bulk of charge collection is a result of the deposited charge diffusing to the subcollector/substrate junction. Typically, the transient peak is determined by the peak carrier density and the collected charge is proportional to the deposited charge. Thus, by increasing the spot size, the peak carrier concentration is reduced for a given amount of deposited charge, which will result in a reduction of the peak amplitude.

The data in Fig. 22 show that it is possible to modulate the relationship between transient peaks and collected charge by changing the spot size of the QBB. This result suggests that another possibility for the shorter duration of the transients generated by the QBB is the difference in spot size between the QBB and the Gaussian beam. The physical origin of these differences is currently being explored using additional data and simulations, and is the subject of future work. One thing to note is that it appears as though the transient peaks and collected charge have the same relationship for spot sizes of 2 and 3 μm. The exact cause of this behavior remains unclear and additional simulations and experiments are required to fully explain the observations.

The results suggest that it is plausible that the transient waveforms generated by the QBB can be matched to ion data by further increasing the laser spot size. This outcome is desirable due to the benefits associated with using QBBs for PL-SEE testing. One of these benefits is that the laser-equivalent LET can be easily calculated

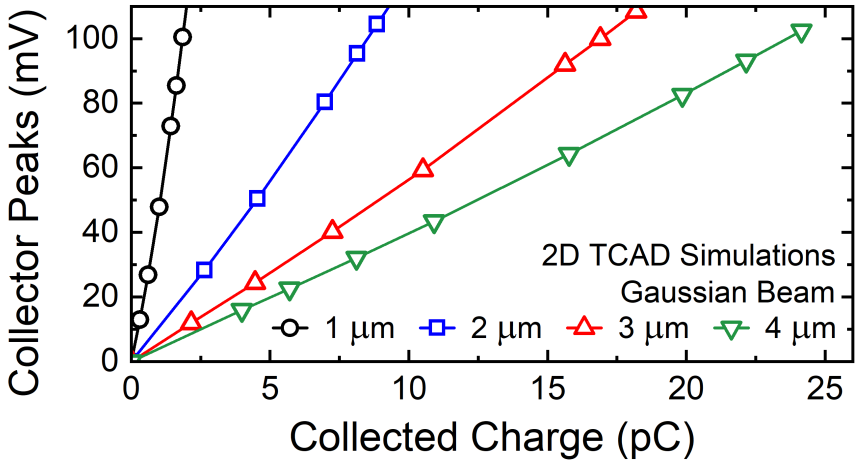

Fig. 21: Simulated collector transient peaks as a function of collector collected charge for different spot sizes of a Gaussian beam.

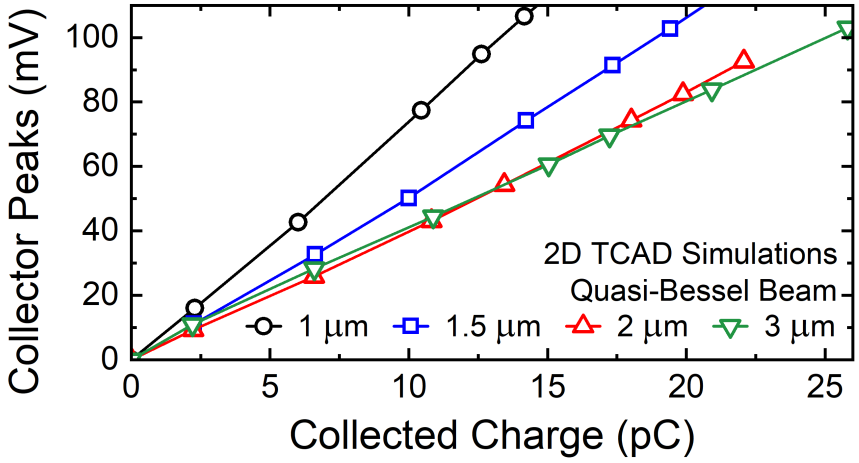

Fig. 22: Simulated collector transient peaks as a function of collector collected charge for different spot sizes of a Quasi-Bessel beam.

and compared with heavy-ion LET [82]. For the Gaussian beam, calculating the laser-equivalent LET is not as straightforward [65]. Thus, from an experimental perspective, the QBB would be preferred as a predictive tool for SETs.

2.4 Summary

This chapter has demonstrated two different approaches to correlating ion- and laser-induced SETs in SiGe HBTs.

The first approach focused on identification, extraction, and error reduction of

waveform features to determine the most appropriate optical geometry for TPA-based, PL-SEE testing. The ability to alter the induced charge distribution by modifying the laser parameters is a key enabling factor in this approach. Using this procedure, the optimal focused spot size for the devices under test, *npn* SiGe HBTs in GlobalFoundries' 5AM platform, was determined to be 1.89 μm (HW1/e^2). Excellent waveform correlation was achieved for laser and heavy-ion transients. In addition, an empirical relationship between laser pulse energy and heavy-ion LET was obtained from the data.

The second approach focused on using QBBs and the first measurements of laser-induced SETs in SiGe HBTs using QBBs were shown. The data show that the transient tails for these transients are shorter when compared with transients of the same amplitude induced using Gaussian beams and heavy ions. TCAD simulations show that this difference is partially due to the potential deformation on the collector-substrate junction, which alters how quickly charge is collected. Further, simulations show that it may be possible to extend the duration of the transients produced by QBBs, to better mimic heavy ion data, by changing the spot size. Additional work is still needed to further explore the effect of spot size on the SETs induced by QBBs. Overall, this novel technique of using QBBs for SEE testing presents several advantages over the more traditional Gaussian beams.

The common factor between these two approaches is that they both manipulate optical geometries to change the relationship between the deposited charge and the peak carrier density of the charge deposition profiles. These approaches are not restricted to SiGe HBTs and can be applied to a variety of semiconductor devices and technology platforms. This ion/laser calibration process can lead to the creation of a "library" containing the optical geometries for each technology platform, thereby allowing experimenters to obtain quantitative information on ion-induced transients

from laser-based experiments at a fraction of the cost. The development of such capabilities would strongly increase the role of PL-SEE testing in the radiation hardness assurance process.

CHAPTER III

ASSESSING THE EFFECTS OF SINGLE-EVENT TRANSIENTS IN RF CIRCUITS

3.1 Introduction

With the advancement of monolithic solutions for electronic circuits and systems, which provide higher performance at a lower cost, wireless communication has become ubiquitous in modern-day applications. Developments in this field have enabled applications such as satellite navigation, broadband digital communications, mobile satellite services and even environmental monitoring, all of which require in-orbit electronics. Further, once a satellite is in orbit, the communications system is the only way of interfacing with the spacecraft either to retrieve information or fix a newly discovered issue. To ensure the proper operation of these systems in space, the effect of ionizing radiation on their performance must be well characterized and understood.

However, the impact of ionizing radiation on the performance of RF circuits carrying modulated data remains relatively unexplored. In particular, the study of SEEs on wireless communications systems is limited, partly due to the difficulty in measuring and quantifying their effect on system performance.

Most of the work done throughout the years on how SEEs can affect data storage and transfer has been focused on digital circuits and systems. This trend is a result of the relatively straightforward way to experimentally characterize the effects on SEEs on digital systems. Although there are many variables when testing such systems, in general, the approach is similar. A bit pattern is either written onto a memory element or fed at the input of a digital circuit. The circuit is then exposed to ionizing radiation and the contents of the memory, or the output of the circuit, are compared

to the original bit pattern. Any differences observed can be characterized as SEUs or bit errors. The main error metric used for these systems is typically bit error rate (BER) as a function of ion LET. With information about the radiation environment encountered by a specific spacecraft and the results of these experiments the sensitivity of a given system to ionizing radiation can be determined. For RF circuits and systems, the experiments are not so straightforward.

The architecture for a direct-conversion RF receiver is shown in Fig. 23. A modulated RF signal with a complex envelope is received by the antenna. If a heavy ion or another charged particle deposits charge in one of the sensitive nodes of the LNA, the resulting transient will show as a voltage spike at the output of the LNA. A closer look at this waveform shows changes in the amplitude and phase of the original signal. However, it is unclear whether the received data was corrupted by this event. To verify if an SEU has occurred, the signal needs to be downconverted, digitized, and mapped into bits in the digital domain – only then would bit upsets be apparent. At this point, all information of changes in phase and amplitude of the signal from the SET would have been lost. This information could be useful in developing new RHBD techniques at the circuit and system level.

In this chapter, a new technique to characterize and assess the effects of SETs on RF systems carrying modulated data is presented. The method relies on using a tool that RF circuits and systems designers are familiar with: an I-Q or constellation diagram. In addition, a new error metric with the name of transient error vector magnitude is proposed instead of bit error rate. The assessment technique and error metric are explored using TCAD mixed-mode simulations and RF data flow simulations.

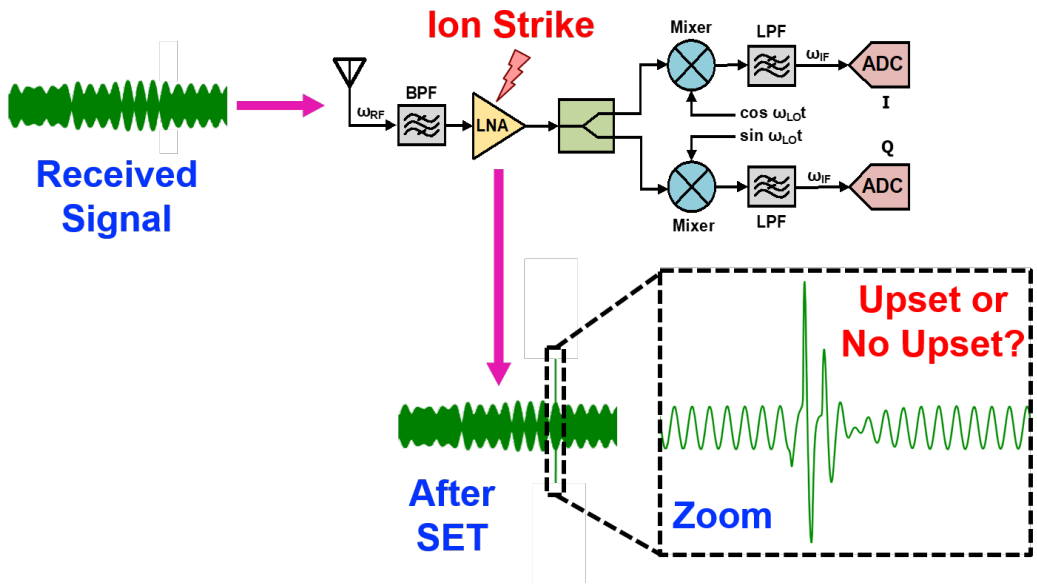

Fig. 23: Diagram of the effects of SETs on modulated data in a direct-conversion receiver. An RF signal with modulated data comes into the antenna and its amplitude and phase are disturbed by an SET generated in a sensitive node of the LNA. It is unclear whether these disturbances will result in corruption of the data.

3.2 Technical Background

In this section, the basics of RF modulation and construction of I-Q diagrams are discussed.

3.2.1 Quadrature Amplitude Modulation (QAM)

In a quadrature phase shift keying (QPSK) digital modulation scheme, which is mathematically identical to 4-QAM, a binary data stream is divided in sets of two consecutive bits, making a symbol. These symbols are then represented using quadrature phases of the carrier as

$$x(t) = \alpha_1 A_c \cos \omega_c t + \alpha_2 A_c \sin \omega_c t \tag{2}$$

where $\alpha_1 = (-1)^{b_I}$ and $\alpha_2 = (-1)^{b_Q}$ for QPSK, with b_I and b_Q being the two data bits, and A_c is a scaling constant [98]. Since two bits are transmitted at once, for a given data rate, the occupied bandwidth is halved, or, equivalently, for a given bandwidth, the data rate can be doubled. This type of modulation is also known as

an M-ary modulation scheme since instead of transmitting binary bits, M possible symbols can be transmitted, which is equivalent to transmitting $k = \log_2 M$ bits at once.

Higher order modulation schemes could be generated, such as 16-QAM and 64-QAM, by allowing α_1 and α_2 to take additional values. For example, for 16-QAM, α_1 and α_2 can take values of ± 1 and ± 3. With these values, one symbol now carries a set of four bits, which reduces the bandwidth by a factor of four for a given data rate. However, for a given carrier power, the symbols are closer to one another in the I-Q diagram, thus making them more susceptible to corruption from noise, distortion and, in this case, SETs.

3.2.2 I-Q Diagram

A constellation diagram, or I-Q diagram, for the demodulated signals can be generated to aid in the visualization of the received symbols. In addition, the I-Q diagram can show analog impairments that distort the received data, such as gain or phase mismatch in the circuit, providing more information than a digital metric such as bit error rate. To construct this diagram, an X-Y scatter plot can be generated by plotting Q vs. I, where, for QAM modulation, $I = \alpha_1 A_c$, and $Q = \alpha_2 A_c$, and the values of α_1 and α_2 depend on the order of the modulation scheme. Alternatively, the diagram can be explained as a polar plot of the amplitude and phase of the signal at a given time. An example of how this diagram is constructed is shown in Fig. 24.

As mentioned above, BER is used to compare the performance between multiple digital systems. Instead of evaluating the BER in the digital domain, we propose using I-Q diagrams to analyze the potential for data corruption.

In the field of RF and communications system, these diagrams are used to identify problems in the system such as amplitude or phase mismatch between the I and Q components. The resulting impairments of the demodulated analog signals can be

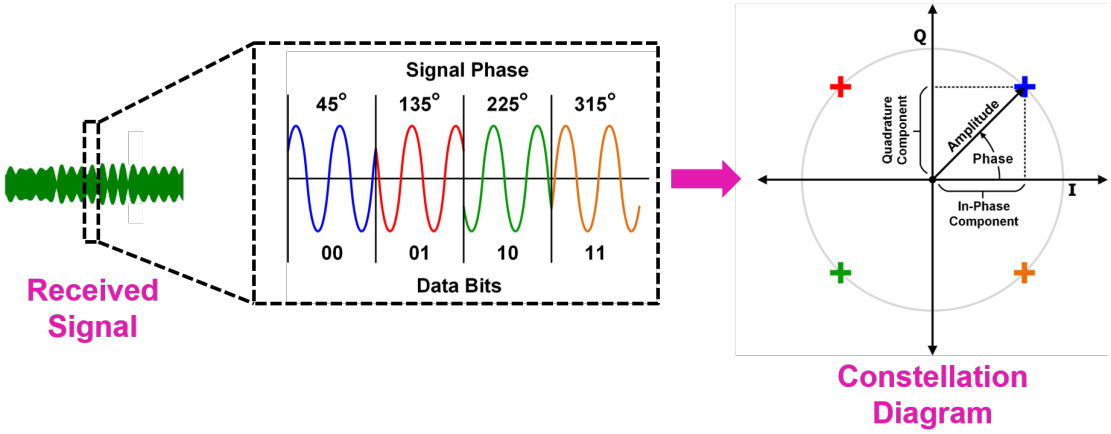

Fig. 24: Schematic diagram showing the process for constructing an I-Q diagram for a signal with QPSK modulation. The bits are encoded in the phase of the signal, and a polar plot is used to represent the received symbols.

directly observed from these diagrams. An example of how these diagrams change with added noise, amplitude imbalance or phase imbalance are shown in Fig. 25. Given the utility of these plots in evaluating issues in the signal chain, this diagram could also be helpful in the context of assessing the effects of SETs on RF circuits.

3.3 Circuit Description

For this investigation, a direct-conversion receiver (RX) with zero intermediate frequency (IF), also known as a homodyne architecture, will be used for analysis and simulation. The system architecture of such a receiver is shown in Fig. 26. Homodyne receivers have several advantages over heterodyne (non-zero IF) receivers [99, 100]. Primarily, this architecture removes the need for an image-rejection filter and simplifies the analog readout circuitry. However, it is more susceptible to leakage from the local oscillator (LO) and to DC offsets. This topology was chosen for analysis since it is one of the simpler receiver topologies, making it a good candidate to demonstrate the proposed testing methodology. This section focuses on the low-noise amplifier (LNA) and the downconversion mixers used to generate the I and Q components for QPSK.

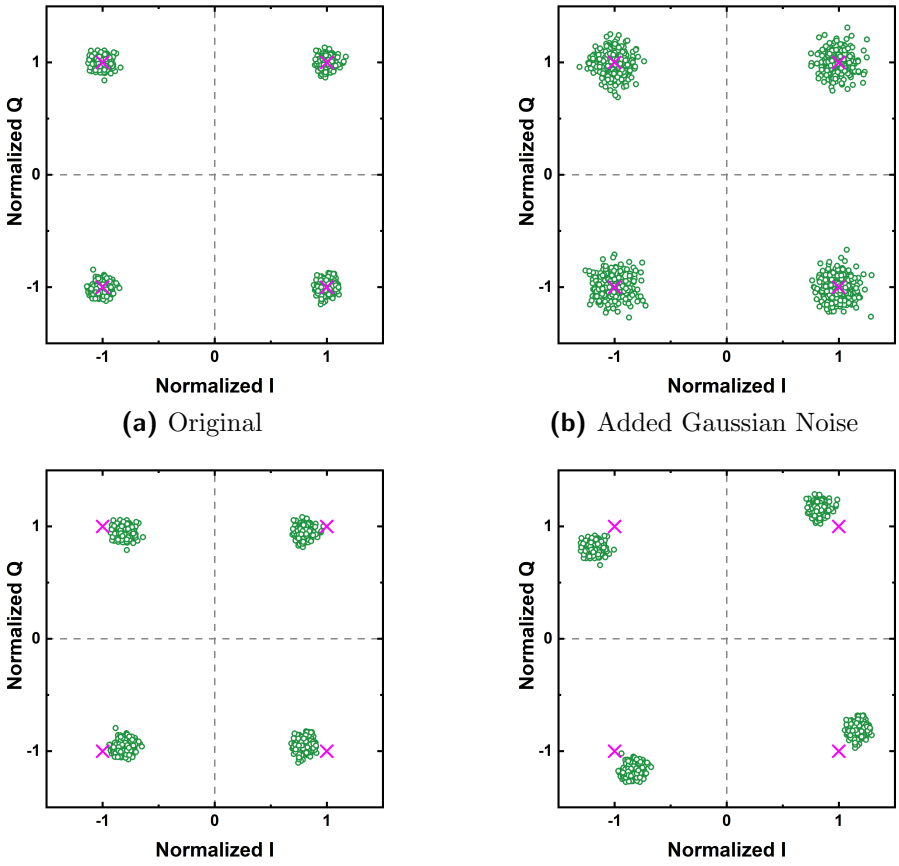

(a) Original **(b)** Added Gaussian Noise

(c) Amplitude Imbalance **(d)** Phase Imbalance

Fig. 25: Simulated I-Q diagrams showing impairments to the received signal. The magenta crosses are the ideal constellation points for the received symbols, which are shown in green dots. Distinct diagrams can be seen for the a) original constellation, and for distortions due to b) added Gaussian noise, c) amplitude imbalance, and d) phase imbalance.

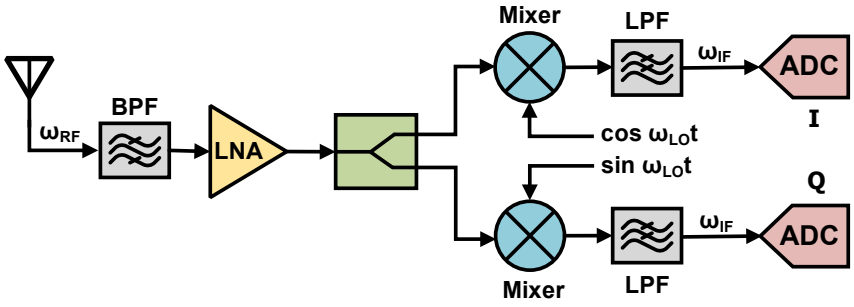

Fig. 26: Simplified schematic of a direct-conversion receiver architecture.

The direct-conversion RX was designed using a third-generation, 130-nm SiGe BiCMOS process (GlobalFoundries 8HP) which features SiGe HBTs with unity-gain

Table 4: Summary of Performance Metrics for the Designed LNA.

Specification	Value
Center Frequency	2.5 GHz
Noise Figure at 2.5 GHz	1.64 dB
Gain (S_{21}) at 2.5 GHz	13.54 dB
Input P1dB	-14.45 dBm
IIP3	-11.25 dBm
Supply Voltage	2.5 V
P_{DC}	3.13 mW

cutoff (f_T) and maximum oscillation (f_{MAX}) frequencies of 200 and 285 GHz respectively [101]. A simplified schematic of the designed circuit is shown in Fig. 27. The LNA uses a cascode topology with inductive emitter degeneration for improved input matching. The core is biased at a current density $J_C \approx 0.3$ mA/μm^2. This LNA topology was chosen as it reduces the Miller capacitance of the common-emitter device and provides great isolation between the input and output nodes.

The downconversion mixers are single-balanced with load capacitors to filter out high-frequency mixing products, and output buffers to prevent loading of subsequent stages. The transconductor in the mixer is biased at a current density $J_C \approx$ 2.88 mA/μm^2. The circuits are designed for a center frequency of 2.5 GHz. For a direct-conversion RX with zero IF, a signal from a local oscillator (LO) with a frequency of 2.5 GHz was used.

The circuits presented in this section are an improved version of the one presented in [3]. In this work, the LNA gain and the mixer conversion gain were improved. A summary of the LNA and mixer performance is shown in Tables 4 and 5, respectively.

3.4 Theoretical Analysis

The remainder of this section presents a high-level qualitative analysis of the propagation of SETs through the signal chain of the direct-conversion RX in order to predict and explain distortions in the I-Q diagram resulting from an SET interfering

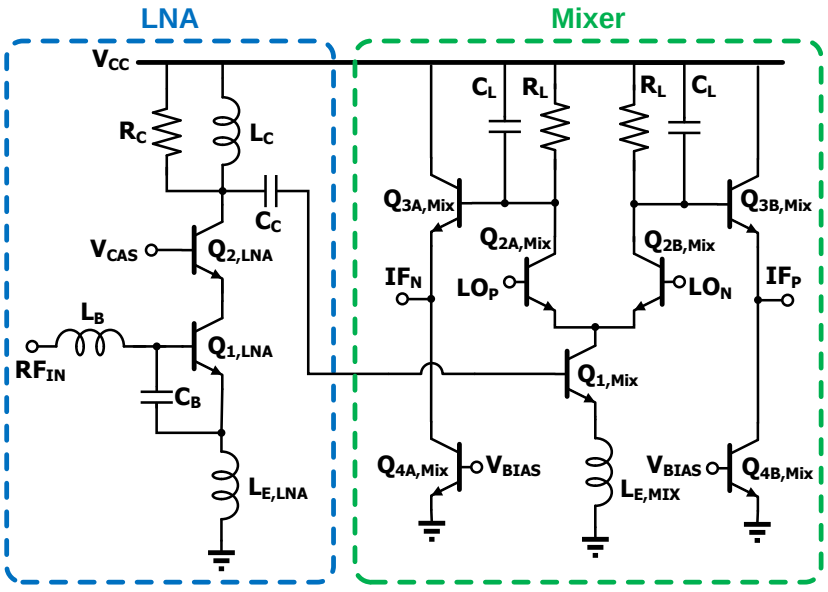

Device	Size
$Q_{1,LNA}$	4 × (5 µm × 0.12 µm)
$Q_{2,LNA}$	4 × (5 µm × 0.12 µm)
$Q_{1,Mix}$	1 × (2 µm × 0.12 µm)

Device	Size
$Q_{2,Mix}$	1 × (1 µm × 0.12 µm)
$Q_{3,Mix}$	1 × (1 µm × 0.12 µm)
$Q_{4,Mix}$	1 × (1 µm × 0.12 µm)

Fig. 27: Transistor implementation of the direct-conversion receiver showing only one of the two mixers (after [3]).

Table 5: Summary of Performance Metrics for the Designed Mixer.

Specification	Value
RF Frequency	2.5 GHz
LO Frequency	2.5 GHz
LO Power	0 dBm
Noise Figure (Dual Side Band)	10.02 dB
Conversion Gain	10.36 dB
Input P1dB	-12.2 dBm
IIP3	-2.6 dBm
Supply Voltage	2.5 V
P_{DC}	20.81 mW

with a QAM signal [3].

3.4.1 LNA Strikes

In the following analysis, we assume a low input power, as is the case for most applications. Previous work has shown that for low input power, SETs presented at

the output of the LNA can be approximated as a superposition of the input signal v_{in} and the generated SET signal, $v_{SET}(t)$ [38]. The output of the LNA, and thus the input to the transconductor of the active mixer, may be denoted by

$$v_{in,Mix}(t) = G_{LNA} \times v_{in,LNA}(t) + v_{SET}(t) \tag{3}$$

where G_{LNA} is the voltage gain of the LNA.

For the LNA topology chosen, the SETs will have a negative polarity [41]. If this effect is represented in the circuit at the output node of the LNA as a transient voltage with negative polarity, $v_{SET}(t)$, then the base-emitter voltage, v_{BE}, of the transconductor will be reduced. This will reduce the bias current of this device, reduce g_m, and cause the points in the I-Q diagram constellation to contract (i.e., move closer to the origin). If the magnitude of the SET is large, the transistor can turn off, collapsing the constellation to zero for a certain period of time [3].

3.4.2 Mixer Strikes

The mixer demodulating the in-phase component has been chosen for analysis. Since both mixers are identical, and the only difference is the phase of the applied LO signal, the analysis will be the same for the mixer demodulating the quadrature component and generality of the analysis is not lost. In the following discussion, $v_{SET}(t)$ is assumed to have a negative polarity, which agrees with data from previous experimental studies [40].

The analysis begins by considering strikes to the g_m device or transconductor, labeled $Q_{1,Mix}$ in Fig. 27. Based on the simulation setup, it can be assumed that the duration of the SET is much longer than the period of the LO signal, T_{LO}, such that the pulse width $\tau > 2 \times T_{LO}$. These assumptions are further explained in Section 3.5, but the result is that the transient will be sampled and presented at each output [39]. The transient at the transonductor, v_{SET}, has a negative polarity, which increases the bias of the switching transistors. The resulting output voltage due to $v_{SET}(t)$ has the

form

$$v_{out,Mix}(t) = v_{in,Mix} \times g_m R_L \times (A_{LO} \cos \omega_{LO} t - v_{SET}(t)) \tag{4}$$

where g_m is the transconductance of the input device, R_L is the load resistor at the mixer output, ω_{LO} is the LO frequency and A_{LO} is the LO amplitude.

Most mixer implementations have a low-pass filter load to suppress high-frequency components above the IF frequency. In a down-conversion mixer the IF frequency is lower than the LO frequency. Therefore, the LO frequency component will be removed and the transient generated at the transconductor will appear as a common-mode output. If a balun is placed at the output of the mixers, and the single-ended signal is used for processing, the common-mode component will be removed, and the transient will produce no effect on the constellation diagram. On the other hand, if the differential signal is fed directly into a differential IF amplifier, as required by some applications, then the amplifier will cancel out the common-mode component if it can handle the typically large signals produced by SETs. If the amplifier does not have enough dynamic range, then there is a potential concern for saturation or change of bias which could result in data corruption.

In an actual circuit, although there will be some suppression of the LO power at the output due to this low-pass filter, there will always be some LO component at the output. If this power is large enough, the transient generated at the transconductor will appear at the output with a dual polarity, as shown in Fig. 28. In this case, the distortion to the constellation diagram will depend on when the signal is sampled, and can not be easily predicted. Taking multiple samples of the output signal and averaging them in the digital system should reduce the effect of this transients, although it places higher design difficulty in the analog-to-digital converters used to sample the signal since now they would have to be able to sample at a frequency twice the LO frequency [3].

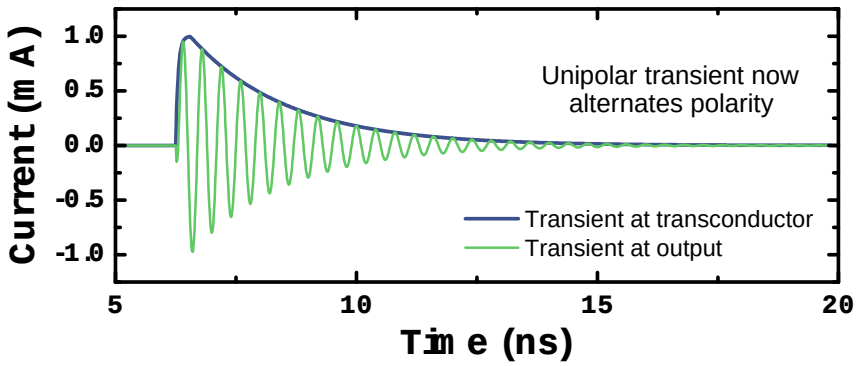

Fig. 28: Time-domain plot of a generated SET before and after being multiplied with the LO signal by the switching devices in the mixer. Note how the transient goes from a single polarity to dual polarity.

Another effect occurs when the amplitude of the SET is large enough to change the operating region of the switching devices from forward-active to saturation. Since the mixer is steering current between both branches, the transient current produced by v_{SET} will flow through the active branch and produce an additional voltage drop at the collector of the switch device. If this device begins operating in the saturation region, the mixer conversion gain will be temporarily reduced [98], resulting in a compressed constellation. This effect should only be observed at higher LETs.

SETs generated by strikes on the switching transistors will directly appear at the output of the mixer. Furthermore, since both switching devices form a differential pair, and the total current must be equal to the current in the transconductor, the transient generated by the struck switch device will steal current from the other switching device, resulting in an opposite polarity transient on the other branch of the circuit. This results in the transient being a differential signal which will not be canceled when the output is taken differentially. Since $v_{SET}(t)$ has a negative polarity, the constellation will translate to higher or lower values depending on the struck device. For example, if $v_{IF} = v_{IFp} - v_{IFn}$, and the switching device connected to the v_{IFn} is struck, there will be a positive transient on v_{IFp} and the constellation will shift to more positive values. The opposite is true for strikes on the device

connected to v_{IFp} [3].

3.5 Simulation Setup

The circuit shown in Fig. 27 was designed and simulated using Keysight Advanced Design System (ADS). A data flow simulation was performed using an ideal QAM modulator block connected directly to the input of the designed receiver (i.e., forming an ideal channel). All simulations were performed with the same pseudo-random bit stream of 10,000 symbols at a symbol rate of 32 MBd, unless specified otherwise, which is used to generate all constellation diagrams. This results in a bit rate of 64 Mbps and 128 Mbps for QPSK and 16-QAM, respectively. The data pulses have been shaped using a root raised cosine (RRC) filter in both the transmitter and receiver with a roll-off factor of 0.5 to limit the data bandwidth. The data were then modulated on a 2.5-GHz carrier with a signal power of -35 dBm. The data were demodulated by the designed receiver and sampled by an ideal component. A total of 15 samples per symbol were taken and averaged to obtained the presented constellation diagrams.

To confirm the theory discussed above, the use of a periodic SET current source connected to different nodes in the system is proposed. For this simulation, it is desired that the transient waveforms decay to zero within the duration of one symbol, which would be equivalent to the RX being struck by a heavy-ion once for every data symbol received. This is achieved by choosing a data rate slower than the transient duration. This approach allows for visualization of the effects that SETs have on the data by using an I-Q diagram. The limitation of this approach is that it does not take into account multiple bit upsets due to a single transient, nor does it take into account distortion due to long diffusion tails that span multiple symbols.

The SET waveforms were obtained from mixed-mode heavy-ion strike TCAD simulations using the Synopsys TCAD suite. In mixed-mode simulations, a circuit netlist

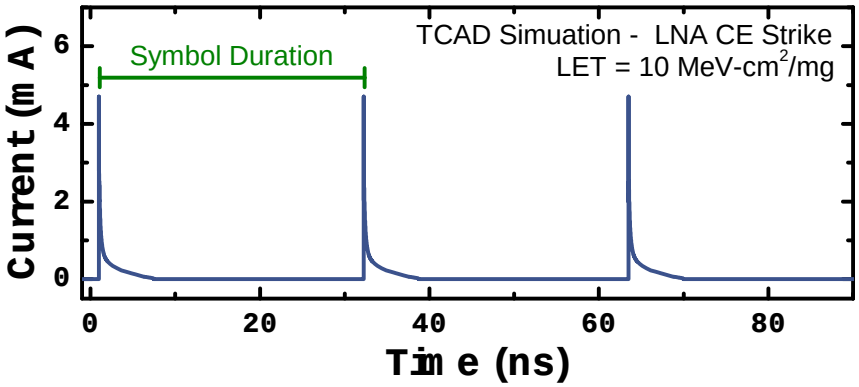

Fig. 29: Time-domain plot of the periodic SET current injected into the common-emitter device in the LNA. Similar waveforms were injected in other devices of the circuit (after [3]).

is built using a 2-D TCAD model calibrated to the 8HP Cadence design kit. The circuit is then biased to the *dc* operating point, and an ion-strike simulation was performed on each device of the circuit. The resulting device transients were then extracted and repeated in the time domain, such that an SET occurs once for every symbol. Fig. 29 shows a transient resulting from this process when the common-emitter device of the LNA circuit is struck by a heavy ion with a linear energy transfer (LET) of 10 MeV-cm^2/mg. Similar transients were generated by ion strikes in different devices of the receiver. The current source was implemented in ADS by specifying time-current pairs in an ideal current source component. The current sources were then connected between each of the HBT device terminals (i.e., collector, base, emitter, substrate) and ground. This simulation methodology has shown excellent agreement with experimental data for these type of circuits [44]. It is important to note that when using a synchronized, pulsed radiation source experimentally, striking every symbol could lead to oscillations in the circuit. Therefore, it would be prudent to strike a given ratio of symbols, with enough time in between strikes to prevent oscillations. Since this was not observed in the simulation environment, the data presented here show strikes for every symbol [3].

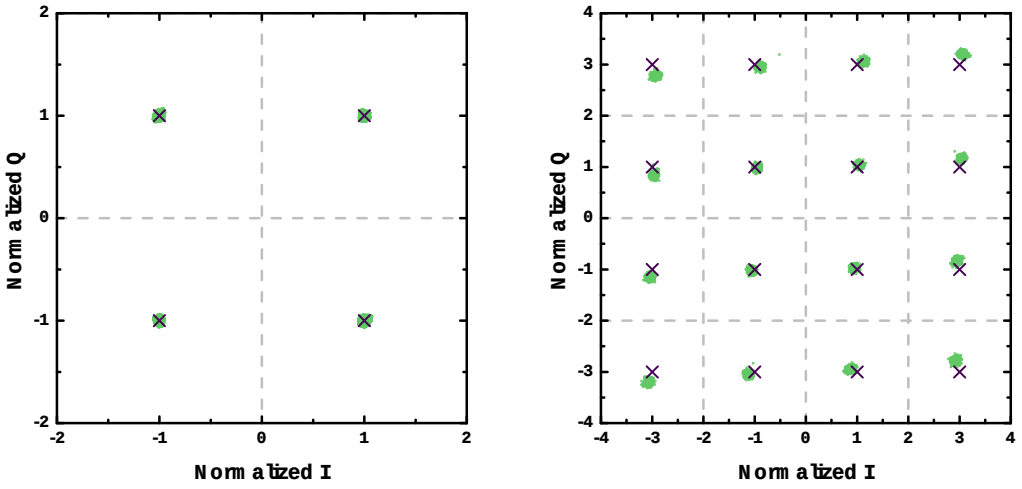

(a) QPSK **(b)** 16-QAM

Fig. 30: Simulated undistorted I-Q diagram at the output of the receiver for the a) QPSK and b) 16-QAM modulation schemes. The dark purple crosses are the ideal constellation points for the received symbols, which are shown in green dots.

3.6 Simulation Results

3.6.1 Receiver Constellation

The implemented receiver was simulated, and the resulting undistorted (i.e., without SETs) I-Q diagram, normalized to the average symbol power, is shown in Fig. 30. Two different modulation schemes, QPSK and 16-QAM, are presented to highlight the increased sensitivity of the circuit to SETs when higher order modulation schemes are used. The green dots are the received constellation symbols while the dark purple crosses are the ideal constellation points. All of the presented constellations have been normalized to this symbol power. The grey dashed lines represent the boundaries between symbols, therefore only distortions that drive a symbol to cross these lines will result in data corruption.

3.6.2 LNA Strikes

Typical implementations of LNAs use parallel devices in their common-emitter and common-base stages for several reasons (e.g., improve linearity, and achieve simultaneous power and noise matching). In the presented implementation, both the common-emitter and the common-base stages are composed of four parallel devices. However, it is very unlikely that two heavy ions pass simultaneously through a sensitive node in the circuit. Therefore, only one device was struck with a heavy ion in the TCAD simulations.

Fig. 31a and Fig. 32a, show the normalized I-Q diagram, for QPSK and 16-QAM modulated signals, respectively. Shown in green dots are the results from simulated SETs on the common-emitter device of the LNA, $Q_{1,LNA}$ in Fig. 27, whereas the dark purple crosses show the ideal constellation points. As predicted by the theory, the constellation diagram contracts during an SET. It can be observed that there is no corruption to the received data for QPSK modulated signals. However, since 16-QAM symbols are closer together for the same input power, the plot shows that after an SET occurs, the symbols will be identified erroneously, resulting in data corruption [3].

3.6.3 Mixer Strikes

The normalized constellation resulting from ion strikes to the transconductor, $Q_{1,Mix}$ in Fig. 27, are shown in Fig. 31b and Fig. 32b for QPSK and 16-QAM modulated signals, respectively. The ideal constellation points are shown as dark purple crosses. In this case, the low-pass filter at the output does not suppress the LO power enough, so the output transient will be a bipolar transient such as the one shown in Fig. 28. Therefore, the constellation shows dispersion around the ideal symbols, as expected. Note that the dispersion is mostly in the in-phase component, since this is the mixer

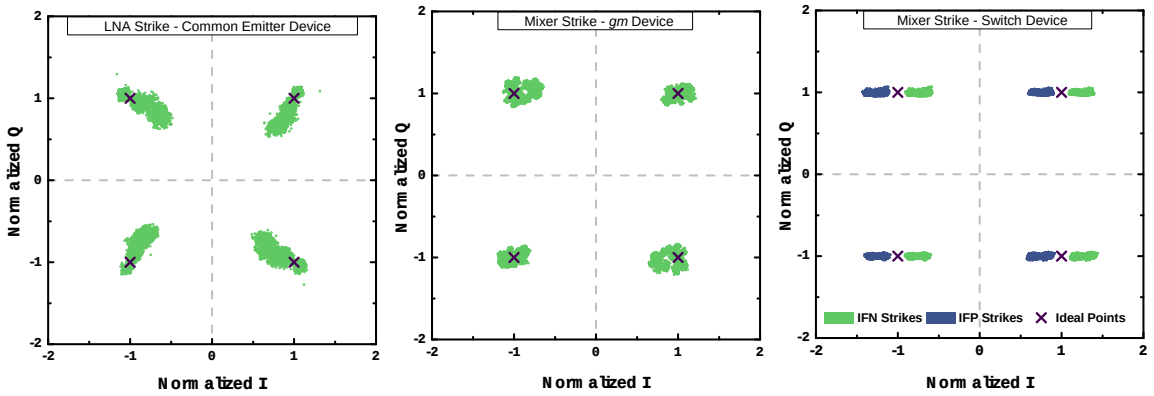

(a) LNA Strikes **(b)** Mixer Strikes – g_m device **(c)** Mixer Strikes – switch device

Fig. 31: Simulated I-Q diagrams for a QPSK modulation scheme when there are heavy-ion strikes on a) the LNA common emitter device; b) the g_m device of the mixer; and c) the switch device of the mixer. The pre-distorted ideal constellation points are shown with dark purple crosses, while the distorted points due to SETs are shown in green dots. The LET used for all simulations is 10 MeV-cm^2/mg.

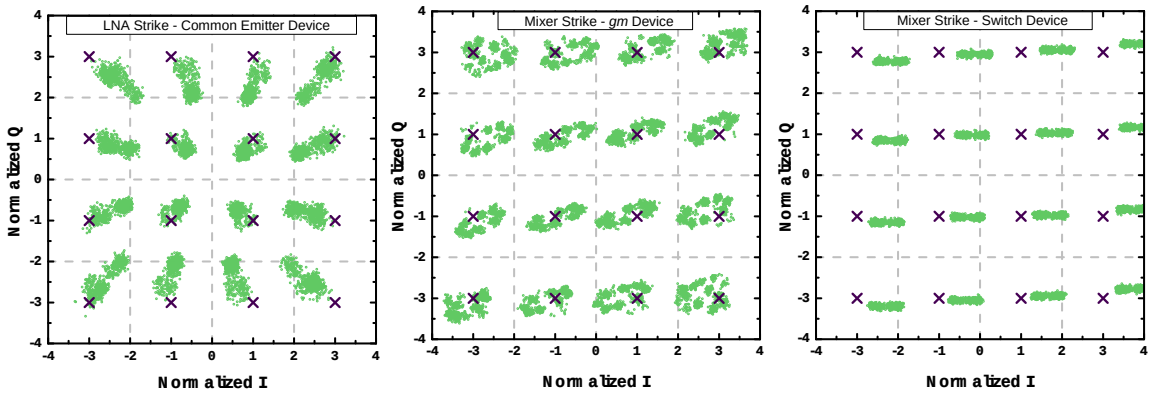

(a) LNA Strikes **(b)** Mixer Strikes – g_m device **(c)** Mixer Strikes – switch device

Fig. 32: Simulated I-Q diagrams for a 16-QAM modulation scheme when there are heavy-ion strikes on a) the LNA common emitter device; b) the g_m device of the mixer; and c) the switch device of the mixer. The pre-distorted ideal constellation points are shown with dark purple crosses, while the distorted points due to SETs are shown in green open circles. The LET used for all simulations is 10 MeV-cm^2/mg.

that is being struck by SETs. There will be some distortion of the quadrature component due to the transient signal leaking from the in-phase mixer via the base of the transistor to the base of the g_m transistor in the quadrature mixer. This was confirmed in simulation by adding ideal isolators between the LNA and mixers. Note

that, similar to the LNA strikes, there is no symbol corruption for the QPSK constellation. However, due to the higher sensitivity of 16-QAM to SETs, some of the received symbols will be corrupted.

Fig. 31c shows the constellations resulting from heavy-ion strikes to the switching device connected to v_{IFn} ($Q_{2A,Mix}$) in green dots, and the device connected to v_{IFp} ($Q_{2B,Mix}$) in dark blue dots, for QPSK modulated signals. As predicted by circuit theory, the constellations get translated in the positive direction for strikes to the device connected to v_{IFn}, and in the negative direction for strikes to the device connected to v_{IFp}. The resulting constellation for 16-QAM modulated signals is shown in Fig. 32c for strikes on the device connected to v_{IFn}. The constellation resulting from strikes on the device connected to v_{IFp} has been omitted for clarity of the shown data, but shows the same trend as that for the QPSK case. Again, note how 16-QAM symbols are more susceptible to corruption than QPSK symbols [3].

3.7 Transient Error Vector Analysis

3.7.1 Defining Transient Error Vector

In a constellation diagram, the spread of the received symbols around the ideal point is given by the signal-to-noise ratio (SNR) of the system, as illustrated in the simulated RX constellation of Fig. 25. If a heavy ion strikes the circuit, amplitude and phase changes to the carrier signals will lead to distortions similar to those discussed in the previous sections. We can define a transient error vector (TEV) and calculate its magnitude (TEVM) by comparing the distorted I-Q diagram to the ideal constellation points. We define TEVM as,

$$\text{TEVM} = 100 \times \sqrt{\frac{\frac{1}{N}\sum_{k=1}^{N}(Q_k - Q_0)^2 + (I_k - I_0)^2}{\frac{1}{N}\sum_{k=1}^{N} Q_0^2 + I_0^2}} \tag{5}$$

where N is the number of received symbols, Q_k and I_k are the normalized magnitudes of the distorted I-Q points, and Q_0 and I_0 are the ideal values of the I-Q points for the undistorted constellation.

Table 6: Transient Error Vector Magnitude and Equivalent Bit-Error Rate for Different Ion-Strike Locations.

	TEVM		BER	
Strike Location	QPSK	16-QAM	QPSK	16-QAM
No Strike	1.81	5.24	0	5.08×10^{-18}
LNA – CE	22.19	31.67	3.29×10^{-6}	5.92×10^{-2}
Mixer – g_m	11.27	16.51	3.53×10^{-19}	2.54×10^{-3}
Mixer – switch	19.14	26.22	8.73×10^{-8}	3.30×10^{-2}

By this definition, for a given SNR, a bigger TEVM means the node being struck with the heavy ion will have a higher probability of symbol corruption. Similarly, for two different circuits with a similar TEVM, a lower SNR means a higher probability of symbol corruption. Figs. 31a–31c and Figs. 32a–32c show that the largest distortion to the I-Q diagram results from ion strikes to the LNA. To quantify this, the calculated TEVM values for each strike location, for both QPSK and 16-QAM are shown in Table 6. There are a few things to note about the results in this table. First, the TEVM when there is no SET is low for both modulation schemes. This is expected since the only source of error is the noise power introduced by the circuit, which is the same throughout all the simulations. In addition, all of the TEVM values for 16-QAM are larger than their QPSK counterparts. This is also expected since the 16-QAM points are closer to each other in the unnormalized constellation than the QPSK points, since both signals were modulated using the same carrier power, and there is a higher potential for data corruption. Finally, the TEVM values obtained for LNA strikes are larger for both modulation schemes than those for strikes at other locations. This is not surprising since the LNA carries the signals with the smallest amplitude, and shows the highest distortion in the constellation diagrams. Although the usefulness of TEVM has been shown, it is desirable to convert this value to an expected bit-error rate (BER). The error vector magnitude can be directly related to

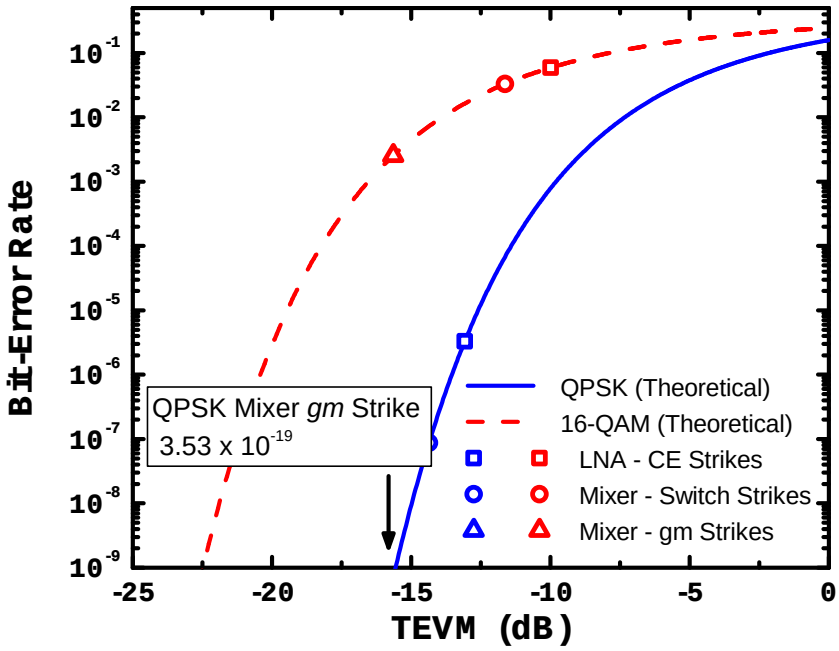

Fig. 33: Bit-Error Rate as a function of Error Vector Magnitude for both QPSK and 16-QAM.

BER by [102],

$$\text{BER} \approx \frac{2\left(1-\frac{1}{L}\right)}{\log_2 L} Q\left(\sqrt{\left[\frac{3\log_2 L}{L^2-1}\right]\frac{2}{\text{EVM}_{\text{RMS}}^2 \log_2 M}}\right) \tag{6}$$

where L is the number of levels in each dimension of the M-ary modulation system, $\text{EVM}_{\text{RMS}} = \text{TEVM}/100$, and $Q(x) = \frac{1}{2}\text{erfc}(x/\sqrt{2})$, with $\text{erfc}(x)$ being the complementary error function. This relationship is shown in Fig. 33 for both QPSK and 16-QAM. The plot shows the direct relationship between BER and TEVM, and the increased sensitivity for 16-QAM modulated signals as compared to QPSK.

The equivalent BER has been calculated for each of the obtained TEVM values and have been listed in Table 6. As expected, for increasing TEVM, the BER also increases. This is intuitive, since higher TEVM means that the received symbols are farther apart than their ideal constellation points. Thus, there is a higher probability of a symbol being mistranslated to the equivalent bit stream. The values in this table have also been plotted in Fig. 33, to provide an indication of where these values land in the theoretical curve [3].

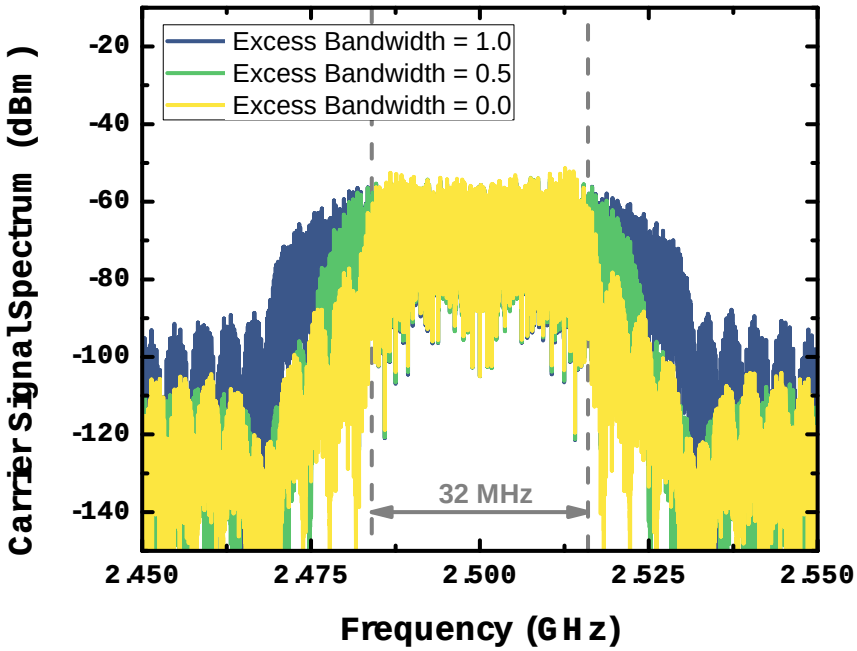

Fig. 34: Spectra of the QPSK modulated data for different excess bandwidth parameter from the root raised cosine filters.

3.7.2 Effects of Data Bandwidth on EVM and TEVM

In order to explore the effects of data bandwidth on the values for EVM and TEVM, the excess bandwidth of the RRC filter at the transmitter and receiver was modified. The excess bandwidth of the RRC is directly related to the roll-off factor and is defined as the bandwidth occupied by the signal beyond the Nyquist frequency, $\frac{1}{2T}$, where T is the symbol rate [103]. Excess bandwidths of 35% to 50% are common. This value is typically expressed as a percentage of the Nyquist frequency, although in this work we specify it as a ratio. Fig. 34 shows the modulated data bandwidth for different values of excess bandwidth. The higher the excess bandwidth of the RRC, the easier it is for the receiver to demodulate the data [104]. Fig. 35 shows EVM for QPSK modulation and TEVM for common emitter strikes as a function of excess bandwidth. The figure also shows the ratio of TEVM to EVM. It is important to recall that the TEVM value will have contributions from receiver non-idealities (i.e., those that contribute to EVM), and from the heavy-ion strikes. The data show

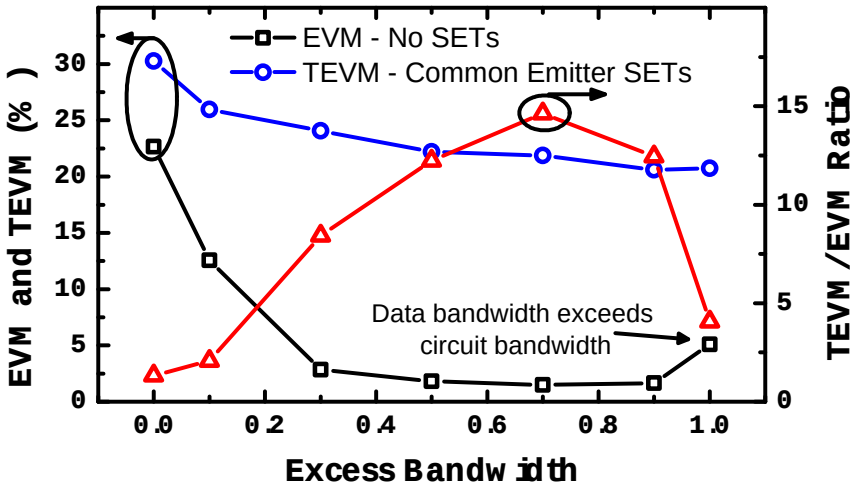

Fig. 35: Simulated EVM and TEVM as a function of the excess bandwidth parameter of the root raised cosine filter.

that for zero excess bandwidth, the EVM values are very high, and the TEVM is dominated by these high EVM values. As the excess bandwidth is increased, both the EVM and TEVM values become smaller, and the contributions of the heavy-ion strikes to TEVM become more dominant, as shown by the increasing ratio of TEVM to EVM. As the excess bandwidth is increased to 1, the data bandwidth begins to exceed the circuit bandwidth, increasing the EVM. The simulation results suggest that, for QPSK modulation, as long as the data bandwidth is large enough for the circuit EVM to be reasonable, and small enough such that it is within the bandwidth of the receiver, it will have little effect on the TEVM values for a given ion-strike location. However, other symbol rates and modulation schemes should be further explored to verify whether this trend holds.

3.7.3 Effects of Data Rate on EVM and TEVM

The testing methodology proposed in this section, and verified in simulation, assumes that the SET duration is contained within the symbol duration, that the repetition rate is equal to the symbol rate, and that the SET is synchronized to the data. Although for a pulsed radiation source the data could be synchronized with the SET

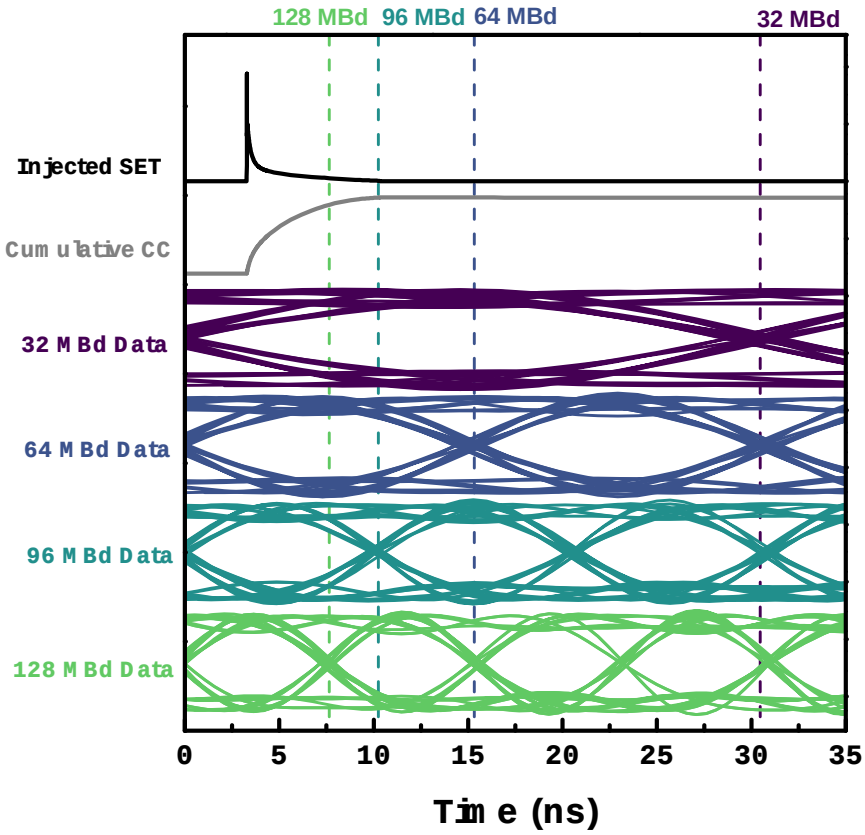

Fig. 36: Comparison between the duration of the injected single-event transient current and the duration of data symbols for several data rates. The dashed lines delimit the symbol duration for each data rate

pulses by synchronizing data triggers and using tunable delays, the other assumptions may be difficult to realize experimentally since the SET duration is determined by both the device and circuit response, and the repetition rate may not be an easily tunable parameter. Therefore, it is pertinent to study the effect of data rate on both the EVM and TEVM for the system. Additional QPSK simulations were performed at symbol rates of 64, 96 and 128 MBd, or at a data rate of 128, 192 and 256 Mbps, respectively. The SET repetition rate was kept constant, to emulate the aforementioned experimental limitations. An excess bandwidth parameter of 0.5 was selected for these simulations.

For a given SET repetition rate, the collected charge per symbol will decrease for increasing data rates since the symbol time is smaller. However, the collected charge

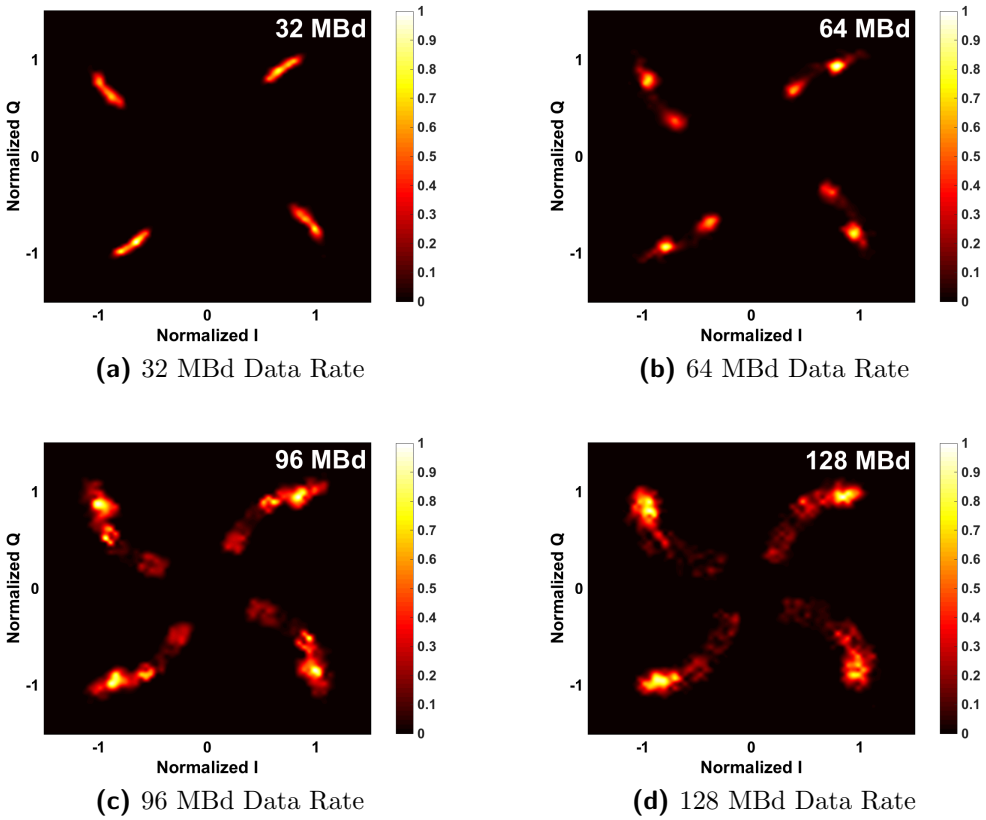

(a) 32 MBd Data Rate

(b) 64 MBd Data Rate

(c) 96 MBd Data Rate

(d) 128 MBd Data Rate

Fig. 37: Simulated I-Q diagrams for a QPSK modulation scheme with periodic heavy-ion strikes on the LNA common emitter device at a repetition rate of 32 MHz, for symbol rates of a) 32 MBd, b) 64 MBd, c) 96 MBd, and d) 128 MBd. The intensity plots show the normalized distribution of received symbols. The LET used for all simulations is 10 MeV-cm^2/mg.

due to a single SET will now be distributed through multiple symbols. This concept is shown graphically in Fig. 36 where the SET, cumulative collected charge, and symbol durations are compared for the different simulated data rates. To observe the effects of uneven collected charge across symbols, the received symbols were sorted into 64 bins to emulate a 6-bit ADC following the designed circuit in the architecture shown in Fig. 26. The counts were then normalized to the maximum count in a single bin and smoothed using linear interpolation between the bins. The final data were plotted as intensity maps in Fig. 37.

The formation of distinct groupings in the data is expected, and results from

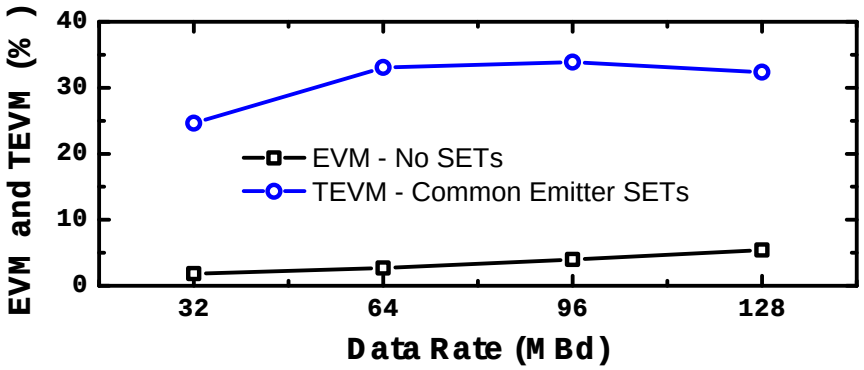

Fig. 38: Simulated EVM and TEVM as a function of symbol rate.

the duration of the SET. Note from Fig. 36 that at 32 MBd, the SET duration is considerably less than the duration of the symbol. This means that when averaging the 15 samples in the received symbols, some of the samples will still contain the undistorted data, which makes the distortion due to SETs appear less severe. The two distinct groupings formed in the constellation for the 64 MBd symbol rate is due to the fact that the SET decays to almost zero within one symbol and is repeated at a rate of 32 MHz. However, for the 96 and 128 MBd case, the tail of the SET is long enough to disrupt the following symbol. This could be thought of a smaller SET affecting the second symbol, forming the additional groupings of data observed.

The spread in the density of the data as the symbol rate increases is also expected. Transmission of higher data rates requires higher bandwidth. However, since the circuit has a fixed bandwidth, increasing the symbol rate would change the effective excess bandwidth, making it smaller as the symbol rate increases. This will show as a spread of the data and an increase of EVM, as discussed in the previous section.

The simulated EVM and TEVM values are plotted as a function of data rate in Fig. 38. As expected from the previous discussion, the EVM values monotonically increase for the undistorted constellation with increasing data rate. In addition, the simulated TEVM values increase from 32 to 96 MBd, but slightly decreases at 128 MBd. This is due to the number of symbols that are unaffected by the SET

at a repetition rate of 32 MHz. The data suggest that, when using the proposed methodology to evaluate the most sensitive parts of the system to heavy-ion strikes, it is recommended that a data rate slow enough for the SETs to decay within one symbol be selected. Note that, since the overall trend of constellation distortions is the same across data rates, applying radiation-hardening techniques and verifying them at a slower data rate using this methodology should still be a valid approach.

3.7.4 Effects of SET Phase on TEVM

Throughout this work, the phase of the periodic SET has been fixed with respect to the received symbols. However, since a real SET will occur at a random point in time, it is pertinent to explore the effect of SET phase on TEVM. First, it is important to remember that in typical receiver architectures, an ADC will sample the IF output and translate the analog signal into bits. Because the ADC will take samples at discrete times, it is important to shift the phase of the SET in multiples of the ADC sampling rate to allow for a fair comparison. This concept is depicted in Fig. 39, where a timing diagram for a 128 MBd symbol rate is overlaid with SETs being injected at samples 0, 4, 8, and 12. Note that if this is not satisfied, the TEVM would be worse when the ADC sample is taken either at or just after the transient peak, since the sample would capture the strongest disturbance on the circuit by the heavy ion. This was verified in simulation by changing the SET phase by steps smaller than the ADC sampling rate, which resulted in the TEVM values being the highest when the samples coincided with the transient peak.

After the peak was aligned to the ADC sampling rate, additional simulations were performed in which the phase of the injected SET was shifted by a single sample. The TEVM was then calculated for each case and is plotted as a function of sample number in Fig. 40, overlaid on the symbol timing diagram for reference. The simulation results show that the receiver is more vulnerable to data corruption when the SET occurs

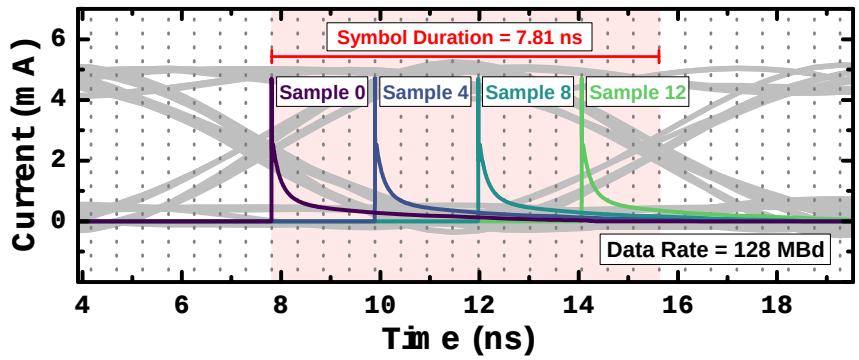

Fig. 39: Timing diagram for a 128 MBd symbol rate showing the relative phase of the injected SETs with respect to the symbol samples. The symbol duration is denoted by the shaded red section. The vertical dashed lines denote the sampling times.

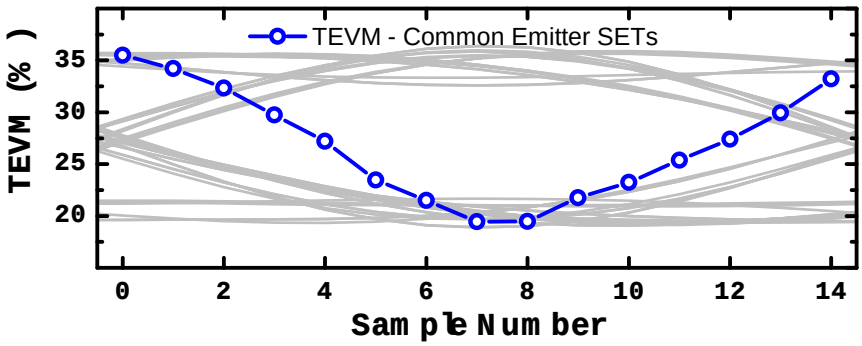

Fig. 40: TEVM resulting from periodic heavy-ion strikes on the LNA common emitter device when the injected transient peak is shifted with sample number.

close to the symbol transitions. Although further experimentation is required to determine the cause of this trend, a likely explanation is that this is a result of the RX architecture. Because the selected homodyne architecture has a DC output that toggles between two values for QPSK modulation, the symbols are more susceptible to corruption closer to the symbol transitions since the magnitude of the output is lower. This should be further explored by performing additional simulations or experiments with a heterodyne RX architecture where the information is not encoded in the DC values.

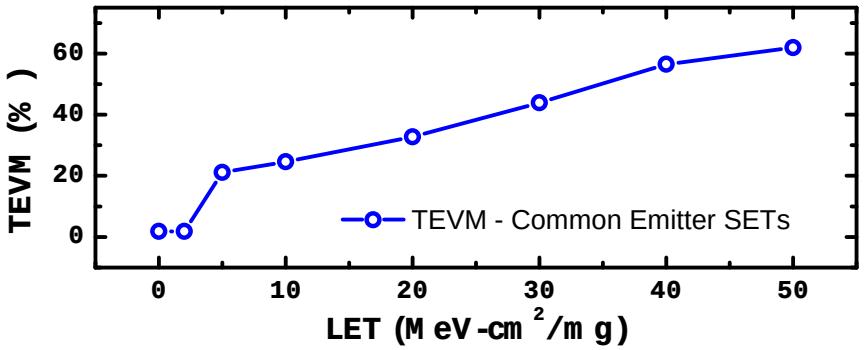

Fig. 41: Simulated TEVM as a function of heavy-ion LET for a 32 MBd data rate.

3.7.5 Effects of LET on TEVM

For all of the previously presented simulations, a heavy-ion energy of 10 MeV-cm^2/mg was used for the TCAD simulations. This energy was chosen since it resulted in modest device-level transients, while still showing the clear trends in the circuit-level simulations. Naturally, it is of interest to explore the dependence of TEVM on LET. Additional simulations were performed at a data rate of 32 MBd for several heavy-ion energies. The resulting TEVM values are plotted as a function of LET in Fig. 41, where an LET = 0 MeV-cm^2/mg is calculated from the undistorted constellation (i.e., no SETs).

As expected, the TEVM values increase with increasing LET. Although there is a slight increase in transient peak at the device level, most of the change in TEVM results from an increase in the diffusion tail. A larger and longer diffusion tail will have a stronger effect on more samples, which will increase TEVM values.

3.7.6 Assessment of Radiation Hardening by Design Techniques

The proposed methodology of evaluating distortions in the I-Q diagram to assess the SET sensitivity of an RF system can be useful whenever analog information on how data are being corrupted is required. Contrary to bit-error rate, analyzing the I-Q diagram provides specific information of changes to amplitude and phase to the carrier that could provide insight into developing new mitigation strategies.

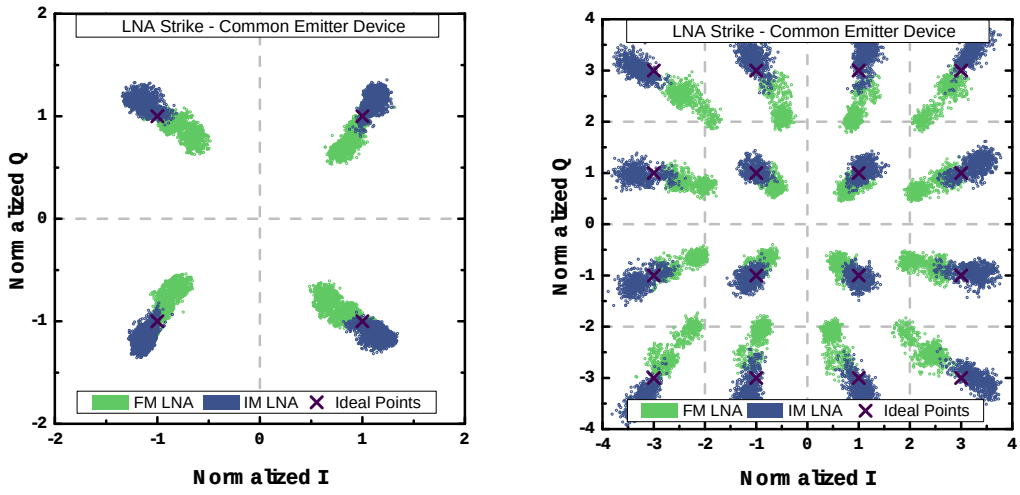

(a) QPSK **(b)** 16-QAM

Fig. 42: Simulated distortions to I-Q diagram for SETs on the common-emitter device of the LNA for both forward-mode (FM) and inverse-mode (IM) cascode operation for a) QPSK, and b) 16-QAM.

In order to confirm that this methodology can be used to evaluate RHBD techinques, the same receiver was simulated by using inverse-mode (IM) operation in the LNA [42]. This circuit design technique that has been shown to be successful in mitigating SETs in a number of RF circuits [40, 41, 43]. IM operation electrically swaps the physical emitter and collector terminals, resulting in an improved SET response due to the physical isolation of the sub-collector to the substrate [42]. For these simulations, the cascode device in the LNA is operated in inverse mode. The output matching network was adjusted to compensate for the difference in capacitance between the collector-base and emitter-base junctions.

Fig. 42a shows the distortions to the constellation diagram when the common-emitter transistor is struck with the periodic current source. It can be seen that the distortions resulting from SETs are less severe for the IM LNA, for the LNA in forward-mode (FM) operation. This improvement has been quantified by TEVM and the equivalent BER in Table 7. The change in response is due to a lower SET peak and duration resulting from using IM devices. The improvement in SET response

Table 7: Comparison of TEVM and Equivalent BER for Ion Strikes on the Common-Emitter under Forward and Inverse Mode Device Operation.

	TEVM		BER	
Strike Location	QPSK	16-QAM	QPSK	16-QAM
LNA – FM	22.19	31.67	3.29×10^{-6}	5.92×10^{-2}
LNA – IM	15.63	11.86	7.88×10^{-11}	6.13×10^{-5}

of this circuit using IM devices has been shown experimentally using a pulsed-laser system [41].

3.8 Summary

In this chapter, a new methodology to test RF systems by using a pulsed radiation source has been proposed and demonstrated through the use of simulations. These simulations show the effectiveness of using I-Q diagrams to visualize the effects of ionizing radiation on modulated data. In addition, a new error metric for RF systems has been proposed. Instead of using BER, TEVM can be calculated from the distorted I-Q diagrams as an error metric for SEEs in RF systems. The effects of data bandwidth, data rate, SET phase, and heavy-ion LET were explored and their effects on EVM and TEVM discussed. The efficacy of this metric was verified by applying it to IM operation, a known RHBD approach for SiGe HBTs. The use of this methodology and TEVM as a metric for radiation hardness assurance, could lead to new and more efficient hardness assurance protocols for RF communication systems.

CHAPTER IV

MITIGATION OF SINGLE-EVENT TRANSIENTS

4.1 Introduction

In previous chapters, it has been shown that RF systems are subject to data corruption due to SETs induced by energetic particles. Ensuring the robustness of the communications system in a spacecraft is crucial since failure of this system might compromise the entire mission. These transients are generated in the active devices and can propagate through the receiver chain [6]. Data corruption could result in undesired behavior of the spacecraft, especially if a command signal that is received from a base station has been affected. Therefore, mitigation strategies for SETs are needed for these critical circuits.

A typical approach for preventing data corruption from SETs or SEUs is to use triple-modular redundancy (TMR). In this system-level design technique all critical components are triplicated and a majority voter is used to determine if data has been corrupted. This technique works because of the infinitesimally small probability that energetic particles will strike two identical nodes in two different systems at the same time. One drawback of this approach, however, is the mandatory increase in size, weight, power and cost (SWaP-C), which can be exacerbated in RF systems.

Contrary to CMOS logic blocks, RF systems have large amounts of static power consumption and triplicating the system may be not be feasible. Furthermore, since data are modulated on high-frequency carriers, dividing the already small RF signal received by the antenna of the spacecraft into multiple paths can be challenging. Specifically, reducing interconnect loss and ensuring matched impedances throughout a triplicated system will be more difficult at higher frequencies. Thus, alternative

radiation hardening techniques must be implemented.

In this chapter, three techniques to mitigate the effects of SETs in RF systems are studied focusing on: 1) sensing SETs using RF power detectors; 2) mitigating SETs by using *pnp* devices in LNAs; and 3) mitigating SETs by using SiGe HBTs on SOI platforms. In the following sections, these three SET mitigation techniques are discussed in detail, and are demonstrated using a mix of simulation and experimental data.

4.2 Detecting Single-Event Effects in RF Systems

One approach to mitigate SETs in RF circuits is to detect when they occur. By detecting these events, error correction techniques could be selectively deployed. If error correction techniques are not sufficient, data retransmission could be automatically triggered.

Previous work has shown that it is possible to design analog circuits to sense SETs by monitoring changes in voltage or currents in a circuit [105,106]. In addition, several methods for transient detection in the digital domain have been proposed [107]. However, no methods for sensing SETs in RF systems were found in the literature.

RF power detectors are typically used in a variety of applications, including: millimeter-wave radiometry [108], envelope detection [109], and built-in-self-testing of RF systems [110, 111].

In this section, the use of RF power detectors to sense the occurrence of an SET in RF communications systems is demonstrated. By sampling a small fraction of the signal from the main data path into a power detector, information about the signal-to-noise and distortion ratio (SINAD) can be obtained. This information can be used by the digital subsystem to implement detection-driven data correction protocols. The proposed concept is illustrated in Fig. 43, which shows the same simplified schematic of a direct-conversion RF receiver shown in Chapter 3 with the addition of the power

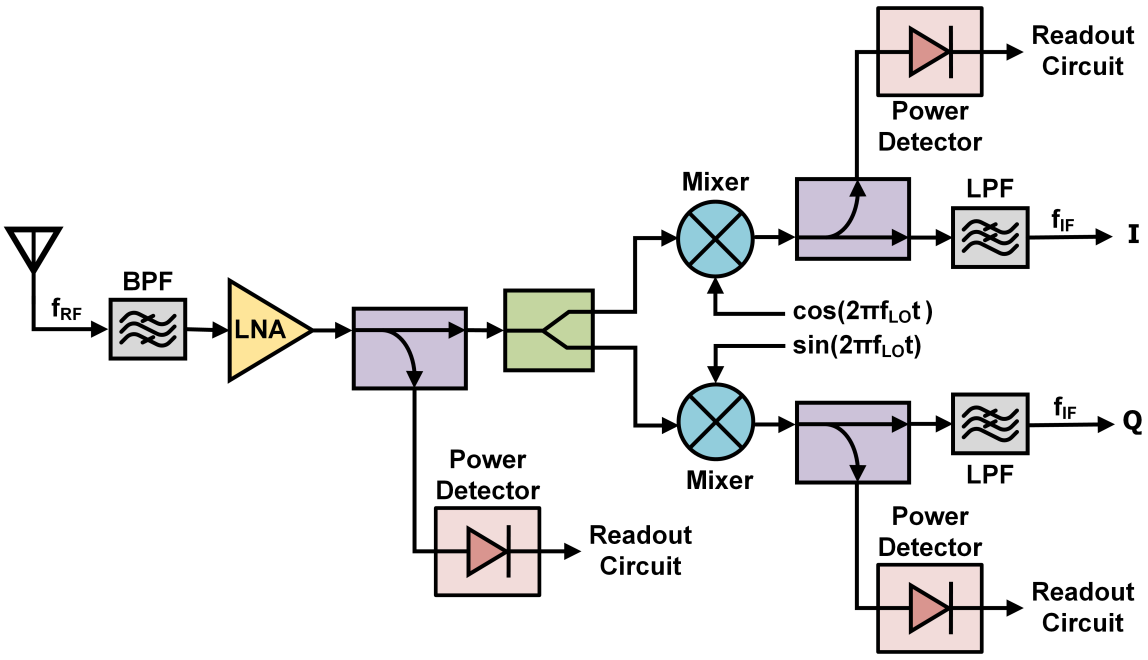

Fig. 43: Simplified schematic of a typical direct-conversion receiver showing the band-pass filter (BPF), low-noise amplifier (LNA), mixers, and low-pass filters (LPF). Directional couplers are used in multiple nodes to sample a portion of the signal and feed it to power detectors for sensing single-event transients.

detector. For this approach, the RF receiver includes several directional couplers between each stage that direct a small fraction of the main signal to the input of an RF power detector. In this case, the output of each detector could be connected to an analog-to-digital converter that would monitor changes in the output voltage of the detector. The use of several detectors at different stages in the receiver allows to determine the block in which the SET originated.

The work in this section has three major goals: 1) demonstrate, for the first time, the use of RF power detectors to detect SETs originated in an LNA; 2) obtain an analytical expression for the detector response to SETs; 3) establish best design practices for optimizing power detectors for sensing SETs. Experimental data and simulations show that power detectors can be used as a system-level SET detection tool to provide diagnostic information for SET mitigation.

4.2.1 Circuit Design and Fabrication

The presented circuits were designed using GlobalFoundries' 8HP platform, a 130-nm SiGe BiCMOS process that features SiGe HBTs with f_T/f_{MAX} of 200/285 GHz. The power detector consists of an inductively-degenerated common-emitter SiGe HBT, $Q_{1,\mathrm{Det}}$, with a relatively large load resistor ($R_{C,Det} = 1\,\mathrm{k}\Omega$) and an output shunt capacitor to filter out the fundamental tone of the input signal. An inductor on the base was used to compensate for the input capacitance and improve the input matching at the frequencies of interest. A schematic and photomicrograph of the fabricated detector are shown in Fig. 44. A reference path, which uses an identical SiGe HBT with a shunt capacitor at the RF input, is also included in the circuit. Typically, the differential output voltage is monitored (i.e., $V_{REF} - V_{OUT}$). This compensates for drift in the zero-power output voltage due to temperature swings or any damage resulting from total ionizing dose (TID).

In this work, our RF circuit being monitored by the detector consists of a low-noise amplifier (LNA) to serve as a proof of concept. A schematic of the LNA and a photomicrograph are shown in Fig. 45. The LNA was implemented using a cascode topology and was designed for simultaneous power and noise matching [112]. This topology was chosen because it provides higher gain and improved isolation between the input and output nodes when compared to a single common-emitter configuration, and is commonly used at these frequencies. The core is biased at a current density of $J_\mathrm{C} = 0.93\,\mathrm{mA}/\mu\mathrm{m}^2$, which results in the minimum achievable noise figure (NF_{min}). To simplify experimental testing, the LNA and detector were integrated on-chip and the output of the LNA was directly connected to the input of the power detector using a $50\,\Omega$ on-chip microstrip line (i.e., no coupler was used in this experiment).

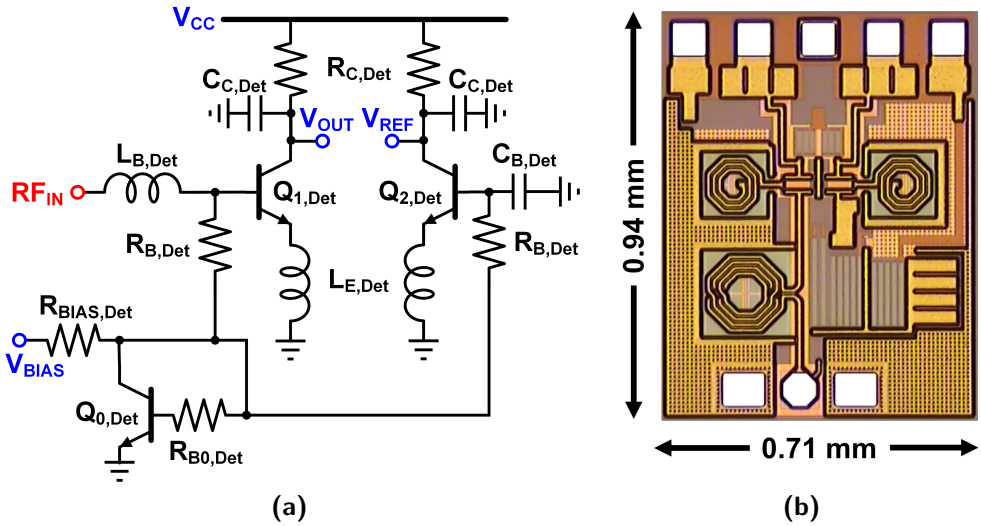

Fig. 44: (a) Schematic and (b) photomicrograph of the designed and fabricated RF power detector measuring 0.71 mm × 0.94 mm including bondpads.

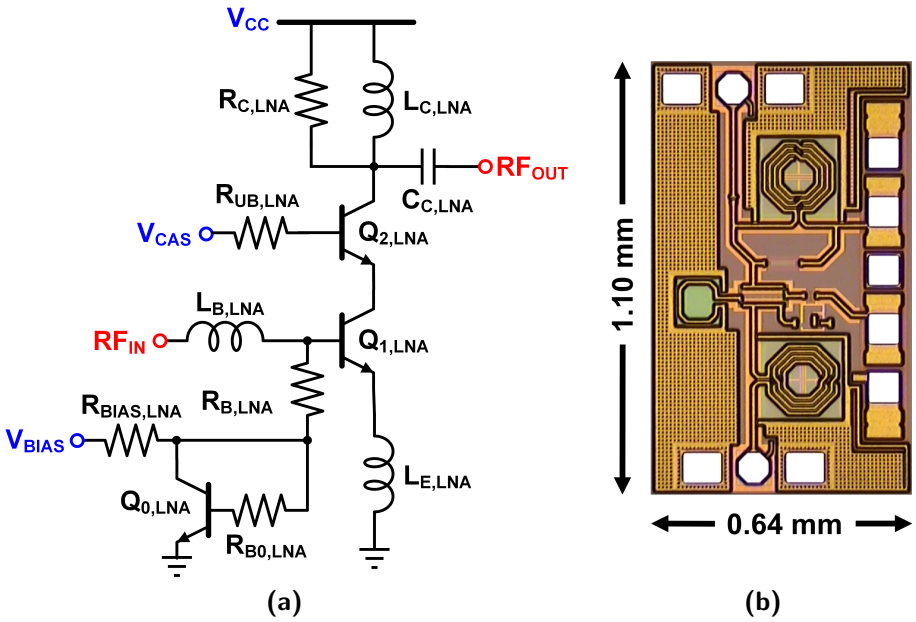

Fig. 45: (a) Schematic and (b) photomicrograph of the designed and fabricated low-noise amplifier (LNA) measuring 1.1 mm × 0.64 mm including bondpads.

4.2.2 Theory of Circuit Operation

The following discussion presents a theoretical analysis of the operation of an RF power detector. The analysis can then be expanded to demonstrate the goal of SET detection. It is assumed that all devices are operating in the forward-active region

and that there are no *dc* offsets between the output and reference paths when no RF input is applied.

For a constant-amplitude, continuous-wave input signal at a single frequency, the change in the differential output voltage of the detector can be expressed by [113],

$$\Delta V_{out} = R_{C,Det} I_S e^{V_{BE}/V_T} \left(e^{V_{RF}\cos(2\pi f_{RF} t)/V_T} - 1 \right) \tag{7}$$

$$= R_{C,Det} I_C \left(e^{V_{RF}\cos(2\pi f_{RF} t)/V_T} - 1 \right) \tag{8}$$

where $R_{C,Det}$ is the load resistor, I_S is the reverse saturation current, V_{BE} is the *dc* bias voltage of the common-emitter device, $V_T = kT/q$ is the thermal voltage, V_{RF} is the amplitude of the input signal, and f_{RF} is the frequency of the sinusoidal wave.

By using the Taylor series expansion, truncated to the first three terms, the exponential can be approximated by,

$$e^{V_{RF}\cos(2\pi f_{RF} t)/V_T} \approx 1 + \frac{V_{RF}\cos(2\pi f_{RF} t)}{V_T} + \frac{V_{RF}^2 \cos^2(2\pi f_{RF} t)}{2V_T^2}$$

With this approximation, the mean value can be calculated:

$$f_{RF} \int_0^{1/f_{RF}} e^{V_{RF}\cos(2\pi f_{RF} t)/V_T} dt \approx 1 + \frac{V_{RF}^2}{4V_T^2} \tag{9}$$

Substituting this result into Eq. (8), the following relation is obtained:

$$\Delta V_{out} = R_{C,Det} I_C \frac{V_{RF}^2}{4V_T^2} \tag{10}$$

This response shows a quadratic dependence of the output voltage on the amplitude of the input sinusoid, which, when converted to input power, translates into a linear relationship. The change in output voltage as a function of input power is a common performance metric for power detectors, also known as the responsivity $\Re$, and is defined by,

$$\Re = \frac{\Delta V_{out}}{P_{in}} = \alpha R_{C,Det} I_C \tag{11}$$

where α has units of W^{-1} and is a constant that relates the input voltage to input power while considering the effects of impedance mismatch [113]. The measured ΔV_{OUT} of the presented power detector as a function of input power, as well as its responsivity, are shown in Fig. 46, for multiple bias voltages. The plot shows a linear dependence of the change in output voltage with respect to change in input power. Deviations from the linear operation at low input powers are due to small *dc* offsets between the output and reference paths, while deviations at high input powers are due to the SiGe HBT on the output path entering the saturation region of operation.

Although the preceding theory was applied to a CW input, the procedure follows from analysis of the detector circuit. Therefore, a similar analysis can be used to obtain an expression for the change in output voltage due to SETs by starting with the same basic relation,

$$\Delta V_{out,SET} = R_{C,Det} I_C \left(e^{V_{SET}(t)/V_T} - 1 \right) \tag{12}$$

where $V_{SET}(t)$ is the SET signal in the time domain. Since this function can vary depending on the part of the circuit that is struck by a heavy ion, the derivation of a universal expression is not possible. However, the expression for the change in output voltage when transients are generated in the presented LNA has been derived in Section 4.2.5.

4.2.3 Experimental Setup

Laser-induced transients on the RF circuits were measured at the U.S. Naval Research Laboratory using the through-wafer two-photon absorption experimental setup explained in detail in Section 2.2. For this particular experiment, the focused spot size was approximately 1 μm.

Two different PCBs were used for this experiment, one set of boards contained a die with just an LNA attached, while another set of boards contained a die with an integrated LNA and detector. Thus, the results shown for the LNA-only and detector

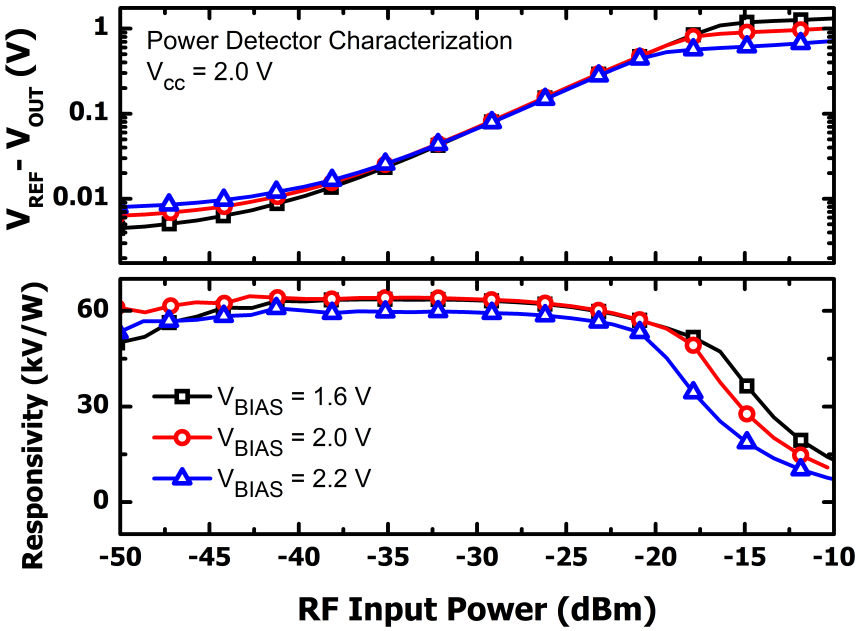

Fig. 46: Measured differential output voltage ($V_{REF} - V_{OUT}$) of the SiGe HBT power detector versus RF input power.

output measurements were taken using different die, although we note that die-to-die performance variations are generally minimal in SiGe technology. All circuits were biased using Keithley 2400 source measure units. For some of the results indicated, a CW signal was delivered to the input of the LNA using an HP 83712A synthesized CW generator; in all other cases, the inputs of the circuits were terminated using 50 Ω through a *dc* block.

4.2.4 Experimental Results and Discussion

4.2.4.1 LNA Output Transients

The common-emitter and common-base devices of the LNA were struck with the TPA laser and all the data shown are for emitter-center strikes, except for the 2-D raster scans. Shown in Fig. 47 are the SETs for strikes to the common-emitter device for different laser energies. The data show that the transients exhibit a dampened oscillatory response with a similar time-constant for all laser energies. To verify the

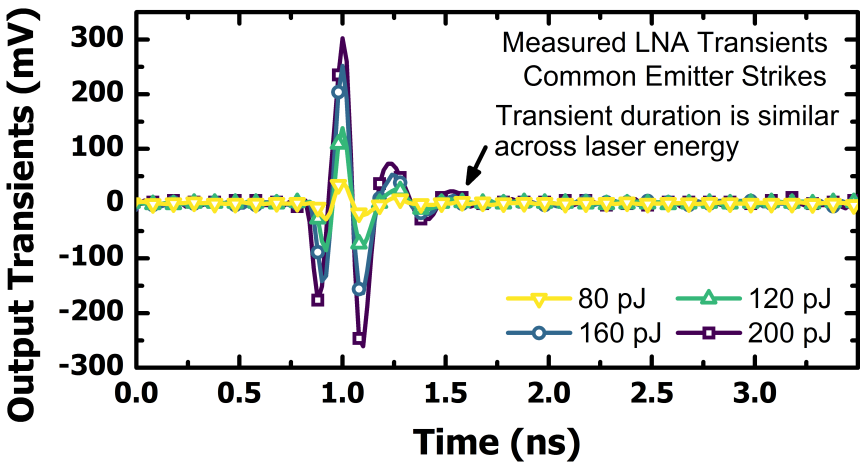

Fig. 47: Output transients in the time domain generated by striking the common-emitter device of the LNA with multiple laser energies.

source of this response, the double-exponential model presented in [114] was implemented in MATLAB and fitted to the SETs observed at the collector of a single SiGe HBT device when subjected to the TPA laser. This fitted transient, was convolved with the impulse response of the output matching network and the resulting signal was compared to TPA-generated SETs measured at the output of the presented LNA. This comparison, which shows excellent agreement between simulations and measurements, can be observed in Fig. 48. The results from these simulations indicate that, for a narrow-band RF circuit, such as the LNA designed for this study, any matching networks utilized at the output will shape the SET generated at the device level, by shaping the frequency spectrum of the transient at the output node. Therefore, it can be inferred that the circuit-level SETs for a narrow-band system at these low frequencies will be in the band of interest and cannot be filtered out. To further confirm this statement, the power spectra of representative measured transients were calculated in MATLAB using the Fast Fourier Transform (FFT) and are shown in Fig. 49. The small-signal gain of the amplifier is overlaid in a dashed line for comparison. The data show that an increase in laser pulse energy results in a monotonic increase in SET spectral power within the frequency band of interest. This is a significant result

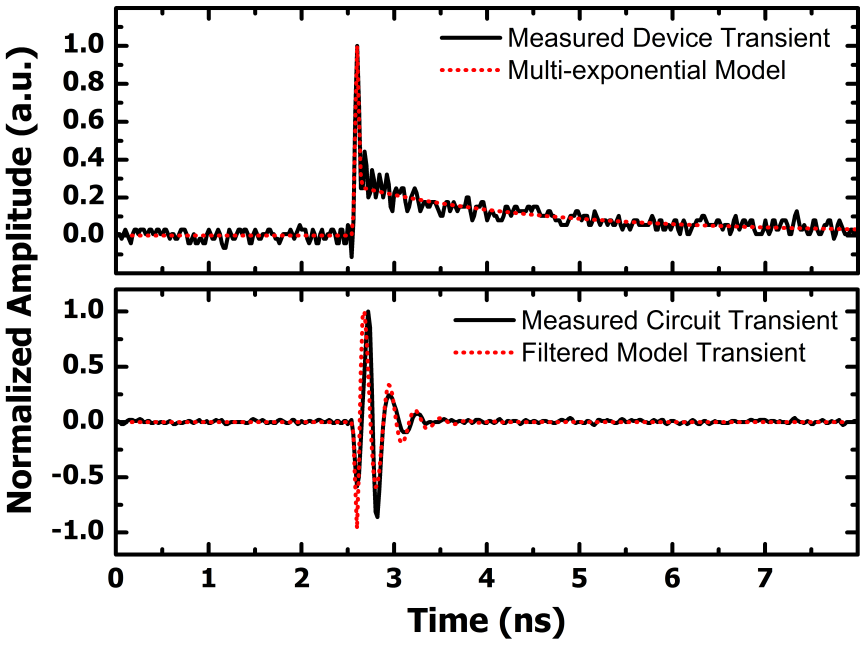

Fig. 48: Normalized amplitudes of measured SiGe HBT collector transients and double-exponential model (top), and measured LNA output transients compared to device transients filtered with a narrow band-pass filter (bottom).

as it confirms two major observations: 1) analog or digital filters cannot be used to attenuate the SETs as they would also attenuate the signals carrying data; and 2) power detectors tuned to detect signals in the frequency bands of interest will also detect SETs as they will reside in the same frequency bands after being shaped by matching networks.

4.2.4.2 Power Detector Output Transients

To evaluate the efficacy of utilizing a power detector for sensing SETs generated by strikes on the LNA, two different test boards were employed: one with an LNA, and another with an integrated LNA and power detector. TPA transients were captured at the LNA output for one test board, and at the power detector output for the other board.

First, it is important to verify whether the detector can capture transients generated throughout the entire device and not just the most sensitive area. To accomplish

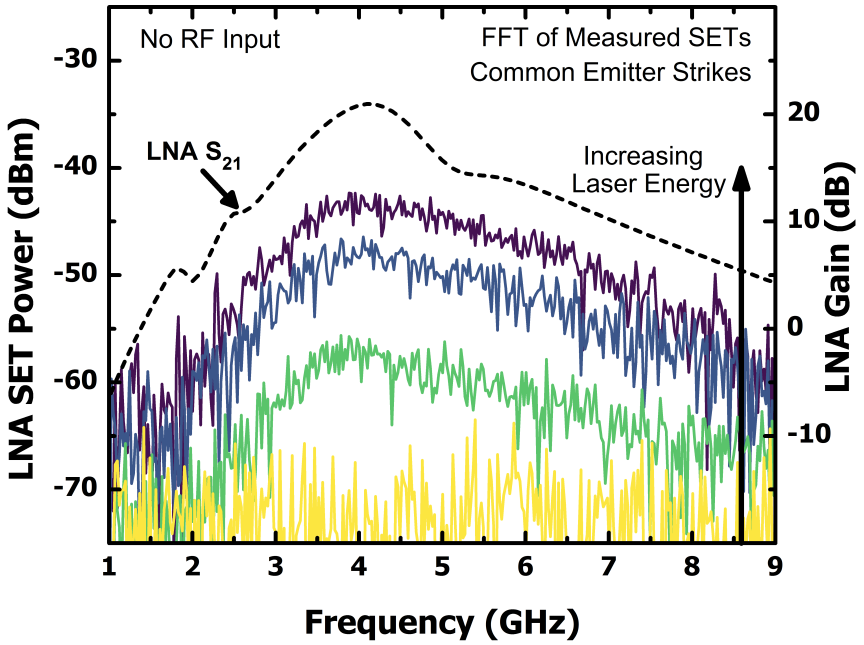

Fig. 49: Power spectra of the measured LNA output transients as a function of frequency for multiple laser energies.

this, the laser energy was fixed at approximately 120 pJ and the beam was scanned across the device, recording transients at each X-Y position. The SET peaks were then normalized to the maximum recorded amplitude and plotted on 2-D raster scans, which are shown in Fig. 50a. The data show that the power detector output can cover the entire sensitive area of the device. This is important because it means that transients generated by off-centered strikes will still be detected. In addition, the FWHM duration for LNA transients and detector transients as a function of position is plotted in Fig. 50b. The data show that detector transients are considerably longer than LNA transients, making it much easier to design the readout circuitry, since this relaxes the required sampling rate.

It is also of interest to verify how well the detector can track the amplitude of the generated SETs in the LNA. To do this, the laser was positioned at the most sensitive area of the common-emitter and common-base devices in the LNA and the laser pulse energy was swept from 110 pJ to 215 pJ. The transient peaks for the LNA output and the detector output are plotted on Fig. 51. The figure shows that for

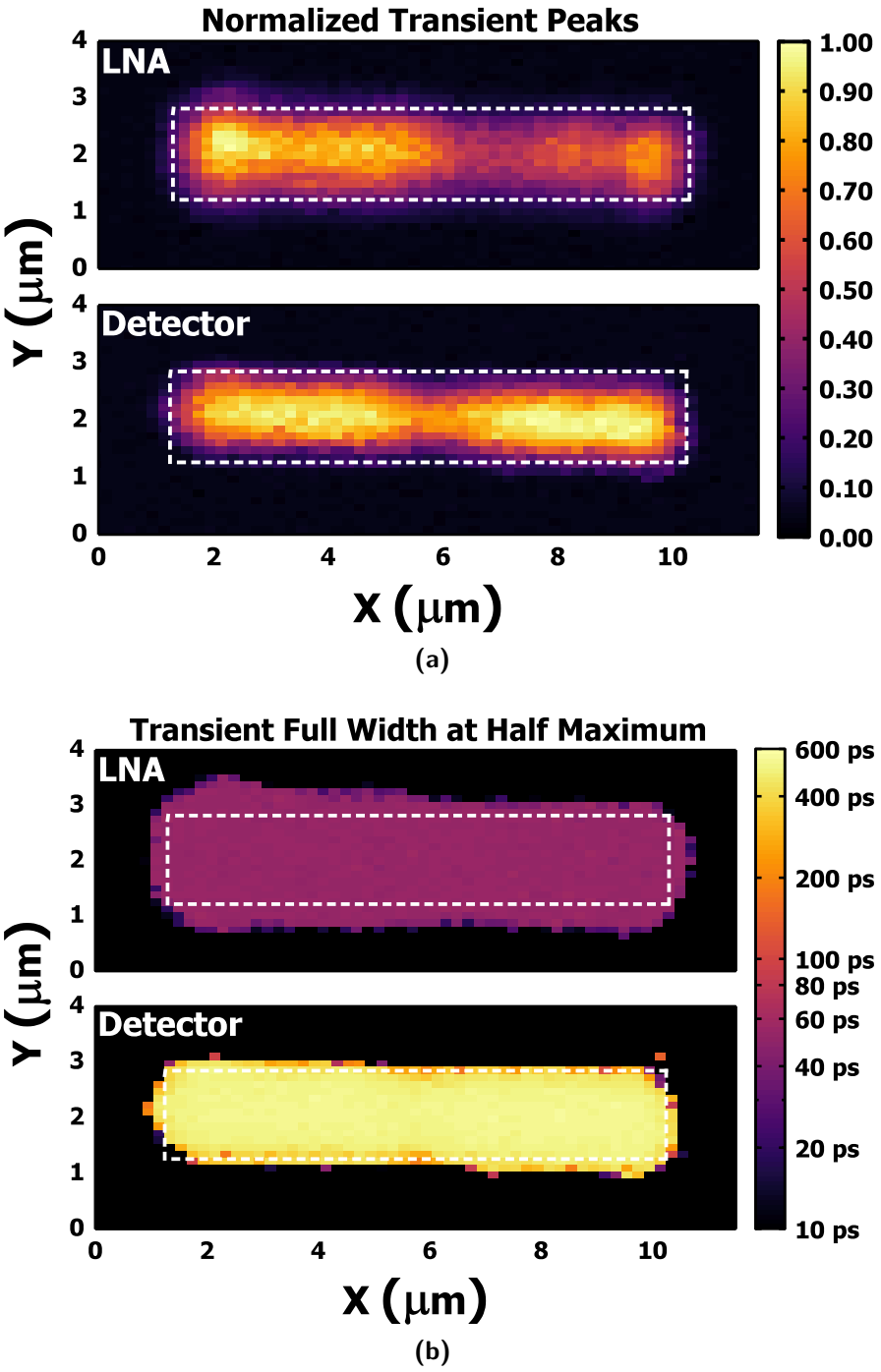

Fig. 50: 2-D raster scan showing the (a) normalized transient peaks and (b) transient FWHM of the common-emitter device in the LNA when the output is taken from the LNA (top) and the power detector (bottom). A laser pulsed energy of 120 pJ was used. The white dashed lines outline the intrinsic region of the device.

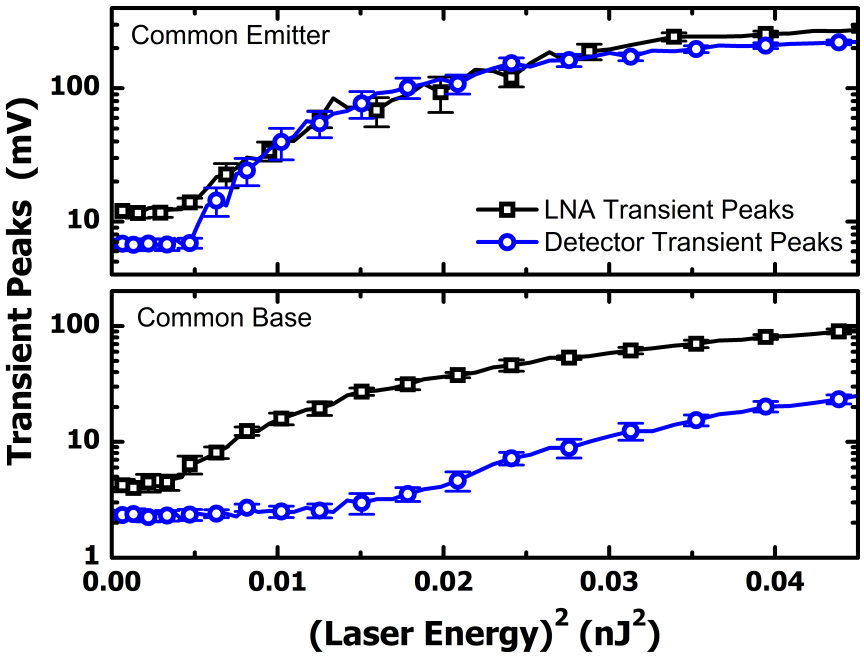

Fig. 51: Magnitude of output transient peaks measured at the LNA output and the detector output as a function of laser energy when each device in LNA is struck.

common-emitter and common-base strikes above a certain, yet different, energy level, the detector output voltage tracks with the amplitude of the generated transient.

To further explore this apparent detection threshold, the power spectra of the SETs generated at the LNA output were obtained by applying the FFT to the time-domain signals. The detector output peaks for common-emitter and common-base devices were re-plotted as a function of the calculated LNA SET power in Fig. 52. It can be observed that for SET powers below -35 dBm the detector is not responsive enough to transients generated by the LNA, regardless of the device struck. This explains the threshold observed in Fig. 51. Note that this threshold is related to the circuit performance shown in Fig. 46, which shows a saturation of the output voltage at a similar input power.

4.2.5 SET Modeling and Responsivity Calculation

In Section 4.2.2, the theory of the detector circuit operation was presented and an expression for changes in output voltage due to a CW input was derived. A similar

procedure can be followed to obtain an equivalent relationship for responsivity due to SETs. The main difference is that, for SET detection, the analysis should be performed in terms of peak amplitude, since the output of the detector would be a transient change in voltage, and it is easier to measure peaks than it is to sample the entire transient. In addition, the output capacitor used to filter the fundamental frequency of the input signal must be taken into account since the transients will be generated in the same frequency band as the signal. The analysis begins with a similar equation for the output voltage, with the addition of a term to account for the charging time of the output capacitor,

$$\Delta V_{out,SET} = R_{C,Det} I_C \left(e^{\frac{v_{SET}(t)}{V_T}} - 1 \right) \left(1 - e^{\frac{-t}{\tau_C}} \right) \tag{13}$$

where $\tau_C = R_{C,Det} C_{C,Det}$.

The experimental laser results showed that the transients generated at the LNA have a dampened oscillatory response, which can be represented using a functional form for v_{SET} given by,

$$v_{SET}(t) = A e^{-t/\tau} \cos(\omega t) \tag{14}$$

where A is the amplitude of the SET, τ is the decay time constant, and $\omega = 2\pi f_0$ is the fundamental oscillation frequency of the SET, which is determined by the output matching network of the LNA.

Similar to the previously presented derivation of $\Re$, the Taylor series expansion can be used to approximate the exponential in the expression for $\Delta V_{out,SET}$. In this case, instead of obtaining the average value for the output voltage, the peak value will be used instead. This is achieved by setting $t = 0$ in Eq. (14). In addition, since the capacitor voltage cannot change instantaneously, the output voltage will begin to change until the SET amplitude decays to a point where it will no longer force the capacitor voltage to decrease, after which, the capacitor will start discharging and return to its *dc* voltage. The peak value will be obtained at some time $t = t_0$. The

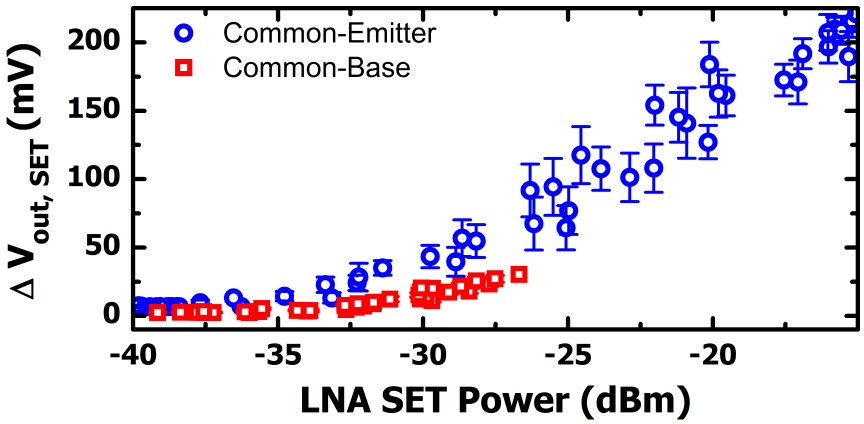

Fig. 52: Magnitude of the detector output transient peaks as a function of LNA output transient power when the devices on the signal path are struck with the laser.

expression for detector output peaks will be given by,

$$\Delta V_{out,SET,Pk} = R_{C,Det} I_C \left(\frac{A}{V_T} + \frac{A^2}{2V_T^2} \right) \left(1 - e^{\frac{-t_0}{\tau_C}} \right) \tag{15}$$

To write this expression in terms of input power, the RMS value for $v_{SET}(t)$ must be obtained by integrating from $t = 0$ to $t = 5\tau$, where the exponential decays to 0.67% of the initial value. The resulting expression is given by,

$$v_{SET,RMS}(t) = A \sqrt{\frac{1}{20} \left(1 + \frac{1}{1 + \tau^2 \omega^2} \right)} \tag{16}$$

Using the same α defined in Sec. 4.2.2, the peak amplitude can be expressed in terms of the input power, P_{in}, as,

$$A = \sqrt{\frac{40 V_T^2 \alpha P_{in}}{1 + \frac{1}{1+\tau^2\omega^2}}} \tag{17}$$

Substituting this expression into Eq. (15), the change in output voltage can be expressed in terms of input power by,

$$\Delta V_{out,SET,Pk} = R_{C,Det} I_C \left(\sqrt{\frac{40 \alpha P_{in}}{1 + \frac{1}{1+\tau^2\omega^2}}} + \frac{20 \alpha P_{in}}{1 + \frac{1}{1+\tau^2\omega^2}} \right) \left(1 - e^{\frac{-t_0}{\tau_C}} \right) \tag{18}$$

To verify this expression against the experimental data shown in Fig. 52, appropriate values for τ and ω must first be determined. The experimental data presented

in Section 4.2.4 showed an increase in transient amplitude for increasing laser energy, while the oscillation frequency, ω, and decay time constant, τ, showed no dependence on laser energy. This experimental result allows for the use of a single value for τ and ω, which can be determined from fitting the expression in Eq. (14) to individual transients obtained for multiple laser energies. A good fit was achieved for transients at all laser energies, and the fitting parameters used are plotted as a function of the laser energy squared in Fig. 53. From this plot, average values for ω and τ can be obtained as $2\pi f_0 = 24.5 \times 10^9$ rad/s and 169 ps, respectively.

The values necessary to fit Eq. (18) to experimental data have been obtained. To simplify the discussion, the parameters β and G will be defined as follows,

$$\beta = \frac{1}{1+\tau^2\omega^2} \tag{19}$$

$$G = R_{C,Det} I_C \tag{20}$$

which simplify Eq. (18) to,

$$\Delta V_{out,SET,Pk} = G\left(\sqrt{\frac{40\alpha P_{in}}{1+\beta}} + \frac{20\alpha P_{in}}{1+\beta}\right)\left(1 - e^{\frac{-t_0}{\tau_C}}\right) \tag{21}$$

The value for t_0 can be determined by considering a square pulse, with a pulse width $= t_0$, as an input to the detector. An expression for RMS amplitude can be obtained over a duration of 5τ to be consistent with the RMS value obtained for $v_{SET}(t)$. By equating the RMS value of the pulse to the RMS value of $v_{SET}(t)$, it can be determined that $t_0 = \tau$.

This equation was used to fit the experimental data in Fig. 52. The parameter β was set to 0.055 since it was obtained from experimental fit of LNA transients and is therefore assumed to be fixed. The parameters G, α and t_0 were varied until the analytical curve fit the measurement data, and the resulting fit is shown in Fig. 54. The shaded red regions designate the range of power levels for which the detector deviates from its linear response for a CW wave input, which will be the ranges for

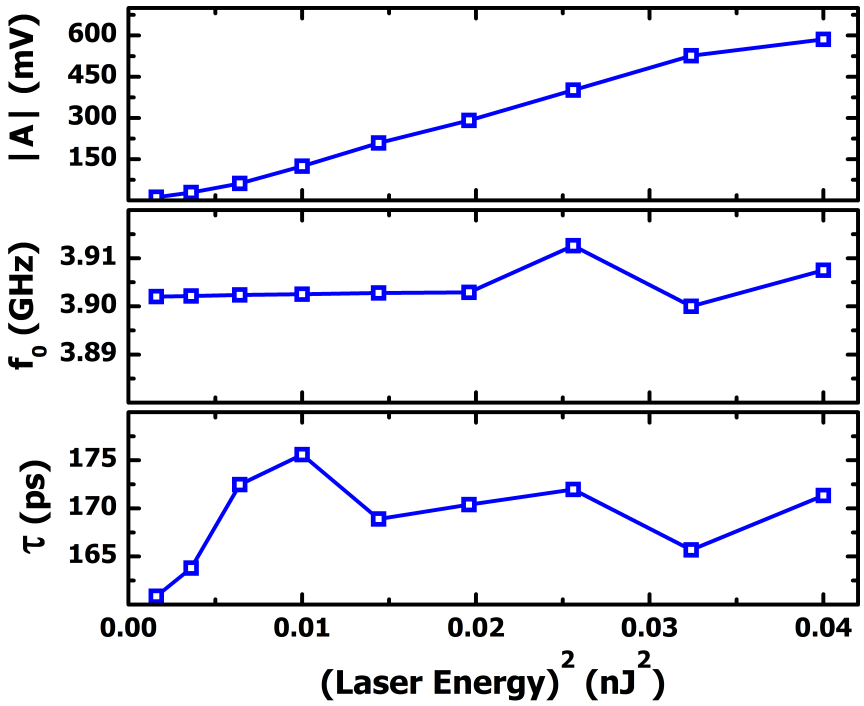

Fig. 53: Parameters used to fit Eq. (14) to experimental data as a function of laser energy.

which the analytical model is not valid. The resulting values for G, α and t_0 were 1,045.7 mV/V, 40,260 W^{-1}, and 156 ps, respectively. The obtained values for G and t_0 closely match the circuit gain and the LNA SET time constant, while the obtained value for α falls within the range of values obtained when several samples of the power detector were characterized. The fact that these parameters match circuit performance metrics and LNA SET characteristics proves that the derived equation results in an excellent fit to the experimental data. This analytical equation could be used to calculate the power and amplitude of the generated SET for the measured change in output voltage of the detector.

The main approximation used in the development of this model is the Taylor series expansion in Eq. (15). The reader will note that, when the Taylor series is truncated to a second-order polynomial, the mathematical approximation will quickly deviate from the original equation. However, Eq. (13) does not take into account device non-linearities and changes in responsivity due to device saturation. These

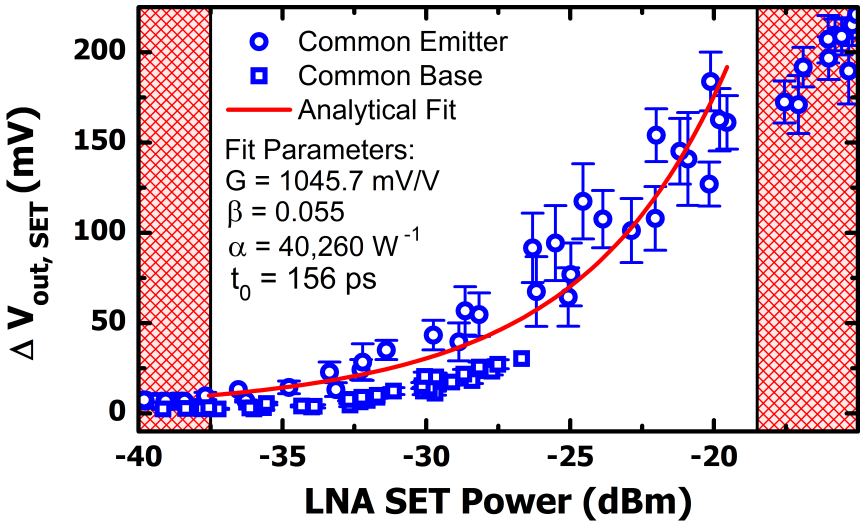

Fig. 54: Comparison of analytical fit to experimental data using Eq. (21).

two approximations, have opposite effects on the resulting expression for the output voltage of the detector (i.e., the truncated series will result in smaller values, while the exclusion of non-linearities will result in larger values). This results in an acceptable model for the power detector presented in this work. More terms may be required for a different power detector design.

In addition, the typical detector responsivity equation derived in Section 4.2.2, which shows that the output voltage is proportional to the input power (i.e., a quadratic relation to the input voltage), is only applicable to low RF powers. At higher input powers, the detector output voltage is proportional to the input voltage [115–117]. The same concept applies to when the circuit is used for SET detection. Although the model developed in this section can be used to fit the data with very good agreement, a more rigorous approach would define a piecewise linear functional relationship. This approach would result in an extended model that would take into account device-level non-linearities and could cover a greater range of input powers, which is of importance when a detector with high dynamic range is used.

4.2.6 Detector Design and Optimization

Up to this point, all of the presented results have assumed the performance of the circuit to be constant. From the theory derived in Section 4.2.2, there are three major parameters that can change the responsivity of the circuit: impedance mismatch, contained in the parameter α; bias current, I_C; and load resistance, $R_{C,Det}$. Introducing additional impedance mismatch between the detector input and the output of the preceding stage will result in a decreased responsivity. Although introducing some mismatch can result in extended bandwidth in some RF circuits and systems, for a narrow-band system such as the one presented in this section, this is typically undesirable, and will not be considered in this study. However, since the goal is to detect transients, the output capacitance is also important, as it will determine the rise time, and by extension the peak, of the detector output. Therefore, the three parameters examined in this section are the load resistance, the load capacitance and the bias current.

When optimizing detectors for SET measurements it is important to recall that, contrary to a CW input which produces a *dc* output, the expected output in this scenario will also be a transient. If the bias current is kept constant, increasing the output resistance and capacitance values will increase the RC time constant at the output of the detector, increasing the rise time and, therefore, reducing the output transient peak. At the same time, for a given input SET, increasing collector resistance will result in a larger peak amplitude at the output. There are two tightly coupled, yet competing factors in this problem. For a given SET voltage input into the detector, a transient current will be generated at the collector of the common-emitter device. Since the output capacitor is meant to filter out the fundamental frequency of the RF signal, then $\tau \ll \tau_C$, and Eq. (21) can be re-written by using a

Taylor series expansion truncated to the first two terms as,

$$\Delta V_{out,SET,Pk} = I_C \left(\sqrt{\frac{40\alpha P_{in}}{1+\beta}} + \frac{20\alpha P_{in}}{1+\beta} \right) \left(\frac{\tau}{C_{C,Det}} \right) \tag{22}$$

This shows that the output transients should be independent of load resistance, and inversely proportional to load capacitance.

Since it is not possible to directly change the load resistance and capacitance of the detector without fabricating multiple circuits, the effects of varying these values were verified using Cadence and mixed-mode TCAD simulations. 2-D SiGe HBT TCAD models have been developed using the Synopsys TCAD suite and calibrated to match the *dc* and *ac* characteristics of the Cadence 8HP process design kit (PDK) compact models. Circuit-level ion-strike simulations were performed on the common-emitter device of the LNA using an LET of 10 MeV-cm^2/mg. The output voltage transients were extracted and used as an input to the detector by using a voltage source that takes values from a lookup table. Transient simulations were performed in Cadence to observe the detector response to a transient input.

The simulation results in Fig. 55a show that the detector output transients are independent of load resistance, until the *dc* collector voltage decreases enough to drive the transistor into saturation, after which the output decreases. These simulation results confirm the expression shown in Eq. (22), which assumes that the device is biased in the forward-active regime. Note, however, that increasing the load resistance will increase the responsivity of the detector, and may cause the detector response to saturate in the presence of an RF signal (i.e., the signal carrying the modulated data).

As previously mentioned, the output capacitor acts as a low-pass filter to suppress the RF signal at the output of the power detector. Since the SET lies in the same frequency band as the RF signal, it will also be suppressed, as shown by Eq. (22). Fig. 55b shows the simulated normalized output of the detector as a function of

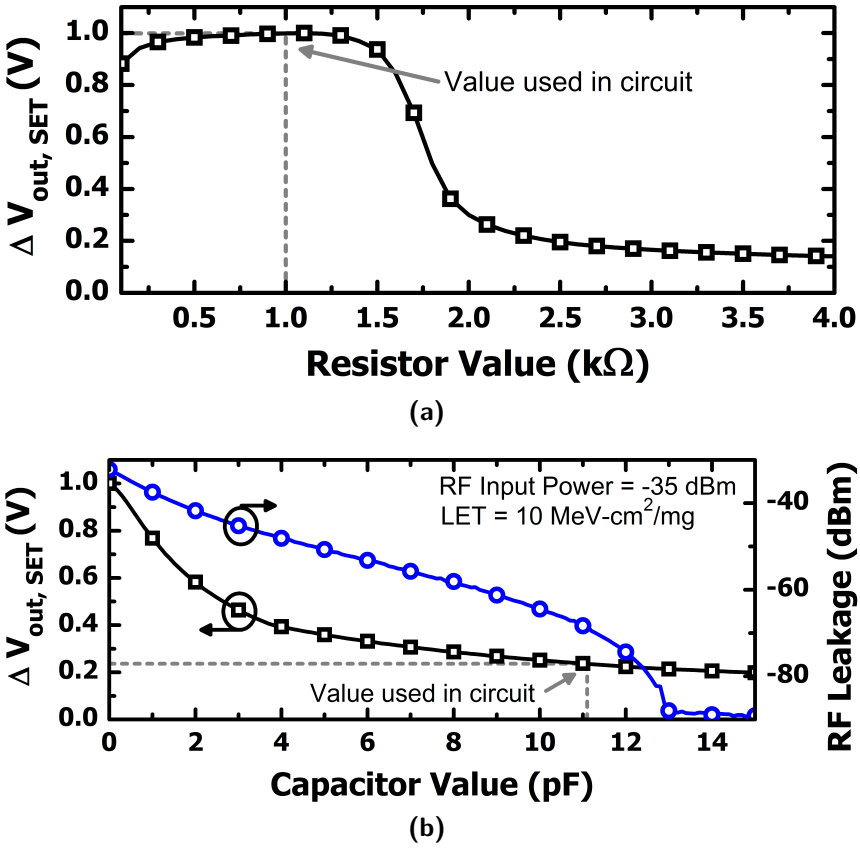

Fig. 55: Simulation of power detector output when the input is a transient produced on the output of the LNA by a heavy-ion strike in the common emitter device for several (a) resistor and (b) capacitor values. For capacitor value sweep, the leakage from a CW signal is included when the input RF power is -35 dBm.

increasing output capacitance values. The simulation results show an inverse relationship between the output voltage of the detector due to SETs and capacitance value, which is in agreement with the expression obtained from circuit analysis. Also shown in Fig. 55b, is the RF power at the output of the detector as a function of output capacitance value for an RF input power of -35 dBm. The data show that for decreasing capacitor value (which increases the change in output voltage due to SETs), the power of the RF signal detected at the output of the detector increased. Therefore, an inherent trade-off exists between transient responsivity and suppression of the RF signal at the output.

To explore the dependence of circuit performance on bias current, the circuit was

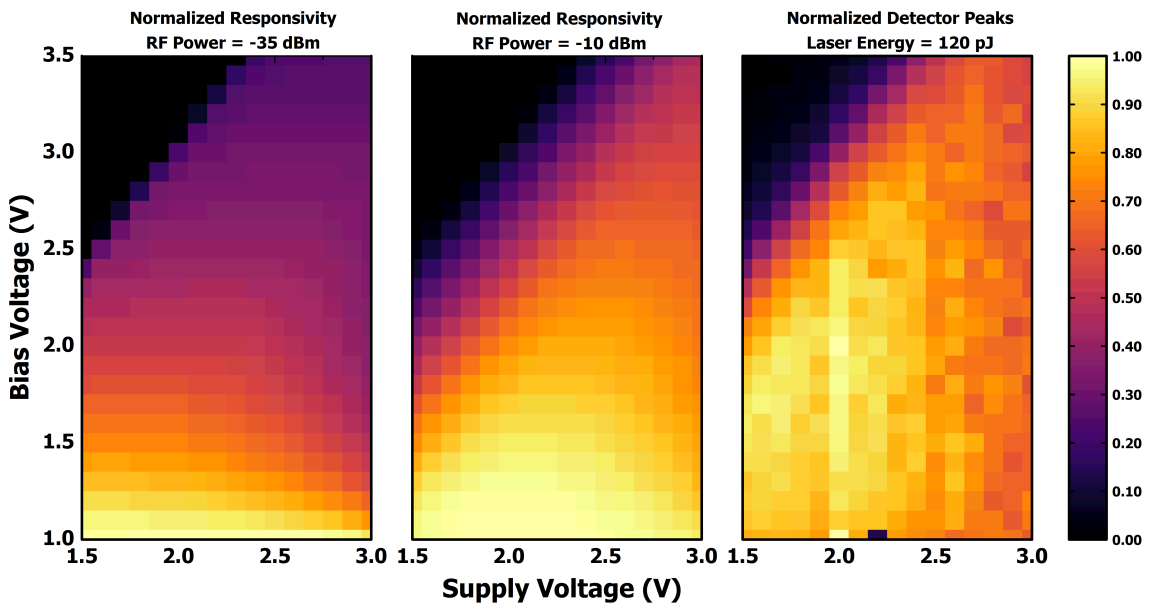

Fig. 56: Comparison of the simulated detector responsivity at an RF input power of -35 dBm and -10 dBm to the measured detector output transient when the laser is focused on the common-emitter device of the LNA. The laser energy used was 120 pJ.

simulated by sweeping the bias voltage. For these simulations, the supply voltage was also swept, since a higher supply voltage will result in higher detector linearity with respect to input power. Responsivity values were obtained for input powers of -35 dBm and -10 dBm, normalized to the peak simulated responsivity, and plotted in Fig. 56 as a function of bias and supply voltage. In addition, TPA results for the same bias and supply voltages were obtained. In these measurements, the laser was focused on the most sensitive part of the common-emitter device in the LNA and the output of the detector was monitored. The detector output peaks were normalized to the highest measured peak and also plotted in Fig. 56. Both responsivity simulations and TPA measurements show a similar dependence on bias and supply voltage.

The data suggest that designing detectors with higher responsivities will make it easier to detect SETs, an intuitive result. However, a trade-off exists between detector responsivity and linearity. Increasing responsivity to the highest achievable value to improve SET detection could cause the detector to saturate with the data signal, leading to decreased sensitivity in SET detection. In such a case, the coupling factor

of the directional couplers could be reduced to avoid saturation of the detector (i.e., a smaller sample is taken from the main signal). Therefore, having knowledge of the expected signal levels at different points in the RF system is crucial to ensure proper design of detectors.

Note that in addition to the bias current and load resistor, transistor sizing can also affect circuit performance, with smaller devices typically yielding higher responsivities. Further studies should be performed to investigate trade-offs between transistor sizing and transient responsivity.

4.2.7 SET Sensitivity with Input Data

Since the output of the RF circuit or system to be monitored will be fed into the detector via a directional coupler, the RF signal going through the system will also be coupled to the detector input. Therefore, it is pertinent to explore the SET response when an RF input is present. This was achieved by focusing the laser on the common-emitter device of the LNA and applying a CW RF signal to the input of the LNA. The output of the power detector was recorded for multiple laser energies and RF input powers. The transient peaks as a function of laser energy are plotted in Fig. 57. The curves show that the change in output voltage increases as a function of laser energy, as expected. For a given laser energy, higher RF input power produces a smaller change in the output voltage. This result indicates that the power detector is capable of indicating the relative power of the generated SET with respect to the power of the RF signal. This is very useful in a scenario where the effects of the SET on the data going through the system are well characterized, since it can allow for the deployment of mitigation techniques that are dependent on the severity of the impact of the generated SET.

Error detection and correction encoding are ubiquitous in communications protocols for most space systems, as they allow for the recovery of corrupted data due to

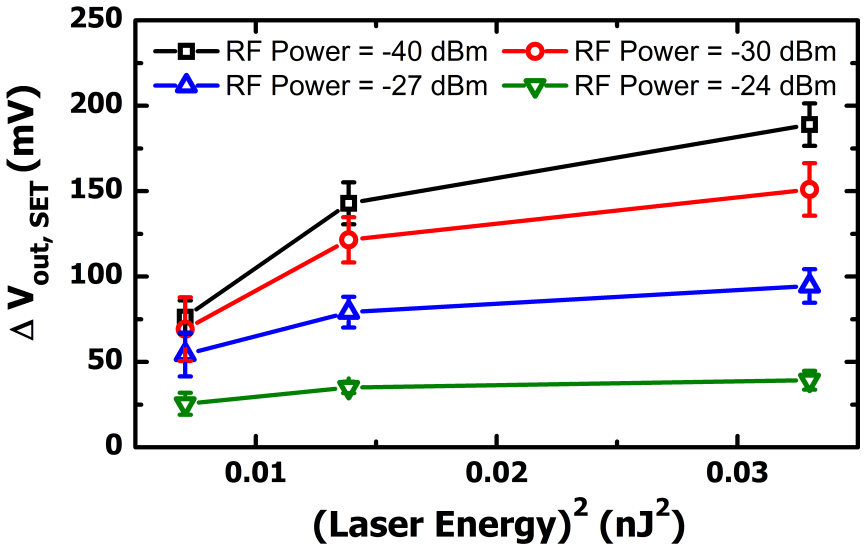

Fig. 57: Measured changes in detector output voltage as a function of laser energy for several values of RF input power.

noise, channel interference, and other phenomena that may compromise the proper reception of the transmitted data stream [118]. It is difficult to determine whether these encoding techniques, which are intrinsic to data transmission and processed by digital systems, are sufficient to mitigate SEUs resulting from ion strikes on the RF receiver. Although they can significantly reduce bit-error rates at the expense of bandwidth or data rate, to say that they are sufficient to mitigate all SEUs requires assumptions of modulation scheme, data encoding scheme, carrier frequency, data rate, among others. However, regardless of these parameters, a power detector could be used to provide additional information to the digital system on the occurrence of SETs, which could be used to: a) confirm that the data correction has been properly achieved (i.e., the affected bit is the one corrected); b) trigger data re-transmission protocols in the event that recovery is not possible; and c) potentially develop new error-correction methodologies with similar robustness and smaller bandwidth penalties than current approaches.

4.2.8 Mitigating Detector Transients

Since the power detector utilizes forward-biased SiGe HBTs, it is also susceptible to SETs. Under normal operation of the detector, the reference path remains unchanged, regardless of whether an SET hits the system of interest or not. Therefore, any transients generated in the reference path would just be ignored by the readout circuit. In addition, a transient generated by a heavy-ion strike in the bias device will propagate through both the output and reference paths, and can be ignored by the readout circuit. However, if a heavy ion passes through the device connected to the detector output, the transient generated could result in a false-positive detection event, since the readout circuitry will not be able to discern between hits to the RF system and hits to the detector itself. A potential mitigation strategy is to implement a concept similar to triple-modular-redundancy (TMR). However, instead of having three different detectors, one detector with three different output paths and one reference path can be used to reduce power consumption. A majority voting circuit can be implemented in the digital subsystem after the readout circuitry. In this implementation, a 3-way power divider would be placed after the directional coupler.

To verify this approach, mixed-mode TCAD simulations were performed. The detector was modified to add two additional output paths. Instead of using a directional coupler, the output capacitor of the LNA was split in three, and connected to each of the detector inputs. Fig. 58 shows the output of the three detector branches when the LNA is struck with a heavy ion compared to when one of the detector paths (Output 1) is struck. For strikes on the LNA, the simulation results show almost identical output transients on all three detector outputs. In contrast, when the heavy ion passes through the detector, only one output, the one connected to the struck device, shows a transient. These results show that SETs on the detector can indeed be mitigated using a pseudo-TMR approach.

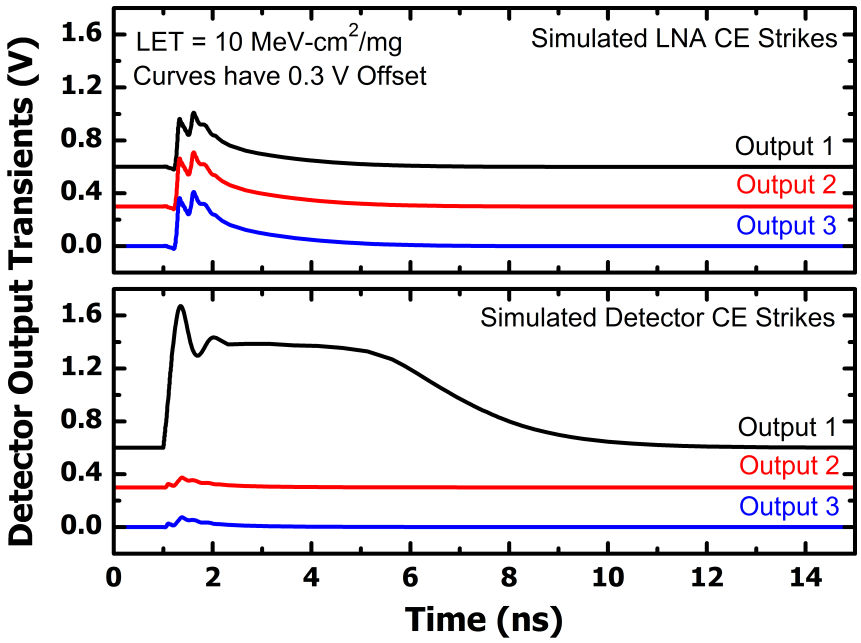

Fig. 58: Simulated detector output transients for heavy-ion strikes on the common-emitter device of the LNA (top) and the common-emitter device of the power detector (bottom). The curves in each plot are offset by 0.3 V for clarity.

4.3 Using Complementary SiGe HBT Platforms to Mitigate Single-Event Transients

Another way of mitigating SETs in RF circuits is to reduce the amplitude and collected charge of the transients. Previous work has shown that one approach to mitigate SETs in SiGe HBTs is to design circuits using *pnp* SiGe HBTs, as they showed an improved SET response compared to *npn* devices, both at the device [34] and circuit level [119–121]. For some of the circuits in previous work [120,121], the improvement in SET response came at no cost to performance, since these circuits operate at lower frequencies. However, the *ac* performance of the *npn* and *pnp* SiGe HBTs, although intended to be "matched," is not identical, which will lead to differences in circuit performance as the frequency of RF operation is increased. In practice, the *pnp* SiGe HBTs will have lower peak f_T/f_{MAX} and higher NF_{min}, which would degrade the performance of the RF receiver. Thus, an inherent tradeoff between RF performance

and SET robustness emerges when considering *pnp* SiGe HBTs as a mitigation technique. However, no studies were found in the literature that focused on investigating the SET response of LNAs designed using *npn* and *pnp* SiGe HBTs in the same platform.

In this section, simulation tools are used to compare the tradeoffs between RF performance and SET robustness in LNAs designed for emerging RF communications systems. Two LNAs designed using only *npn* and only *pnp* SiGe HBTs are evaluated. The circuits are simulated with data modulated on an RF carrier to assess the impact of SETs in an RF receiver. The results indicate that although the *npn* LNA has higher performance it is also more sensitive to SETs when compared to its *pnp* counterpart. The choice between using *npn* or *pnp* devices in RF designs will heavily depend on application requirements and data modulation scheme.

4.3.1 Design Procedure

Two single-stage cascode LNAs with the same topology were designed, one only using *npn* SiGe HBTs and the other only using *pnp* SiGe HBTs, as shown in Fig. 59. The circuits were designed on the SG25H3P platform by IHP Microelectronics [122]. This complementary bulk SiGe:C BiCMOS process features 0.25 μm "performance-matched" *npn* and *pnp* devices with a peak f_T/f_{MAX} of 110 GHz/180 GHz and 90 GHz/120 GHz, respectively [123]. The *pnp* LNA was designed to operate with a negative supply and all n-well connections are tied to ground (i.e., the highest potential).

To enable a fair comparison between both circuits, they were designed for simultaneous power and noise matching using the methodology outlined in [112]. Although this methodology has certain drawbacks [124] and additional circuit design techniques could be employed to improve these circuits, it was chosen for the present work because it provides a robust algorithmic path for design that results in LNAs with good

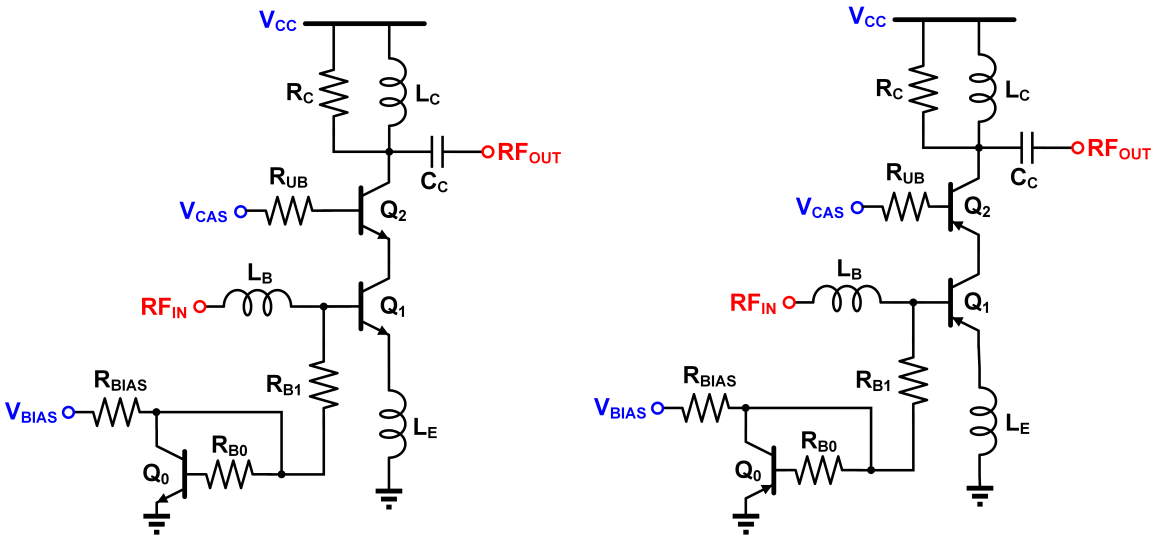

(a) *npn* Low-Noise Amplifier **(b)** *pnp* Low-Noise Amplifier

Fig. 59: Schematic of the designed low-noise amplifiers using (a) only *npn* devices and (b) only *pnp* devices. A negative supply is assumed for the *pnp* design.

performance. Following this procedure ensures that both circuits were designed in a systematic way to allow for a direct comparison between their performance. The LNA design process is described below. Throughout each step of this design process, the emitter areas for Q_1 and Q_2 (as shown in Fig. 59) have been kept equal. A Q-factor equal to 10 was used for all inductors in the following designs since this is a conservative estimate of what can be achieved for an integrated inductor at 5 GHz [125–127].

Selecting Current Density First, the optimum collector current density ($J_{C,opt}$) that ensures minimum achievable noise figure (NF_{min}) must be selected. A one-finger, minimum-sized ($0.84 \times 0.22\ \mu m^2$) device was selected and the V_{BE} of the lower device in the cascode core was swept, while fixing the V_{CE} of the cascode to 2 V with the upper base also connected to 2 V. Both devices in the cascode configuration must be simulated in this step because the $J_{C,opt}$ of the cascode structure is different from that of Q_1 [128]. The maximum available gain (MAG) and NF_{min} are plotted as a function of J_C in Fig. 60. Note that for both designs, significantly higher LNA gain can be achieved by biasing at a higher collector current density with a marginal increase to

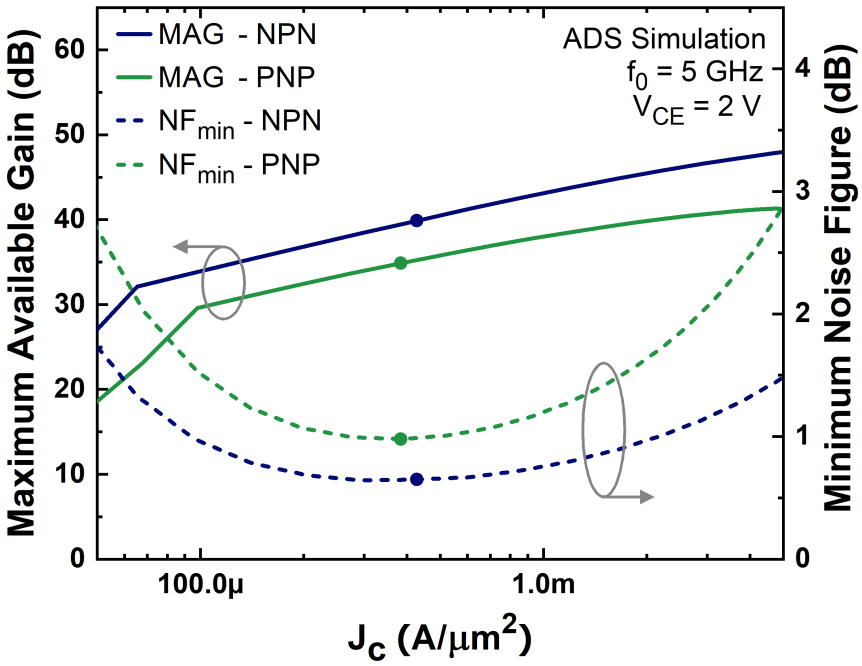

Fig. 60: Maximum available gain and minimum achievable noise figure as a function of collector current density. The dots on the lines show the chosen bias point for each LNA.

noise figure (NF). However, for the purposes of the present study, the value for $J_{C,opt}$ (i.e., minimum NF_{min}) was selected for both cases. The values for $J_{C,opt}$ for *npn* and *pnp* cascode cores are 425.4 μA/μm^2 and 383.3 μA/μm^2, respectively.

Selecting Device Size The emitter area of the cascode devices was then scaled so that the optimum source resistance ($R_{S,opt}$) is close to 50 Ω while maintaining the J_C selected in the previous step. In the fabrication process used for the present study, both the emitter width and the emitter length are fixed, and therefore devices in parallel must be used. The optimum source resistance for noise matching of a single transistor is given by [28],

$$R_{s,opt} = \frac{f_T}{f}\sqrt{\frac{2r_b}{J_C \times A_E}\frac{kT}{q}}, \tag{23}$$

where f_T is the unity-gain cutoff frequency of the device, f is the operating frequency, J_C is the current density at which the device is biased, A_E is the total emitter area,

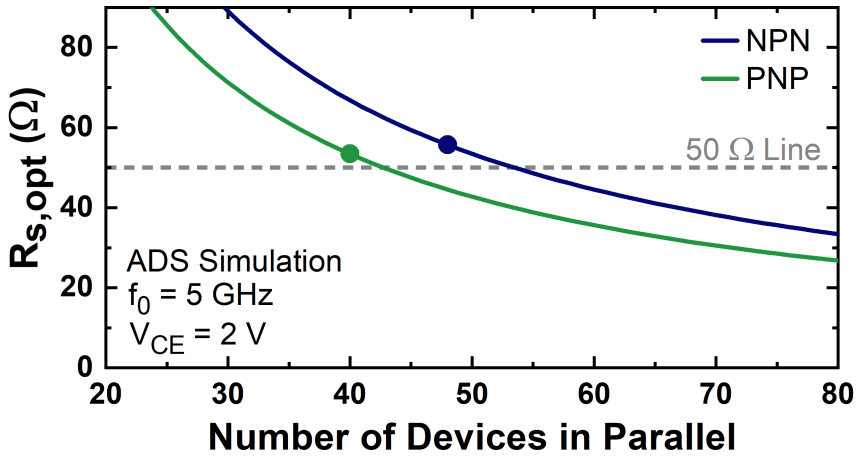

Fig. 61: Optimum source resistance for noise matching as a function of number of parallel devices. The dots on the lines show the chosen sizes for each design.

and r_b is the base resistance. From the equation, it can be observed that by increasing the total emitter area, or in this case, the number of parallel devices, the optimum source resistance can be decreased. Fig. 61 shows $R_{S,opt}$ as a function of the number of parallel devices for the *npn* and *pnp* cascode structures, when biased at $J_{C,opt}$. Note that for the *pnp* cascode, fewer parallel devices are required to achieve 50 Ω due to the fact that this device has a lower f_T. The number of parallel devices for the *npn* and *pnp* devices that resulted in an $R_{S,opt}$ closest to 50 Ω were 48 and 40, respectively. These sizes yield an $R_{S,opt}$ slightly higher than 50 Ω, which will account for the series resistance presented by the finite quality factor of the base inductor added in the following steps. Furthermore, these device sizes allow for a symmetrical layout design. The *npn* cascode core was implemented by using four 12-finger devices, while the *pnp* core was implemented using five 8-finger devices, since 8-fingers was the maximum available for *pnp* devices. The large number of devices required will increase the power consumption, which is the main tradeoff when using this design procedure.

Selecting Emitter Degeneration Inductor The emitter degeneration inductor (L_E) is selected to match the real part of the input impedance. The value of L_E is

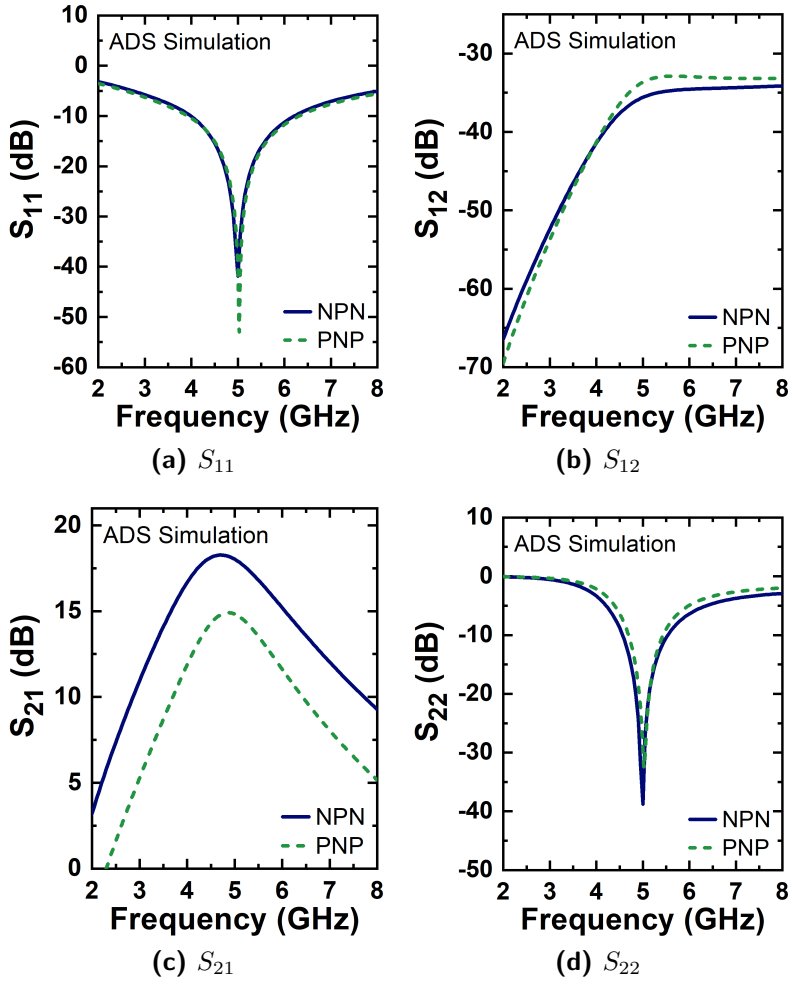

Fig. 62: Comparison of simulated S-parameters for the designed low-noise amplifiers.

given theoretically by,

$$L_E = \frac{50}{2\pi f_T} \tag{24}$$

where f_T is the cutoff frequency of cascode structure, for the selected emitter length biased at the selected J_C. Although this equation gives a good estimate of the required inductance, in practice, the required value will be affected by the quality factor of the inductor. An S-parameter simulation was performed, where the value of L_E was swept until the real part of the input impedance was matched to 50 Ω. This process resulted in values for L_E of around 280 pH and 420 pH for the *npn* and *pnp* designs respectively.

Selecting Series Base Inductor The series base inductor, L_B, is selected to cancel the reactive part of the input impedance. It is given theoretically by,

$$L_B = \frac{1}{\omega^2 C_{BE}} - L_E \tag{25}$$

where ω is the operating frequency, C_{BE} is the base-emitter capacitance of the bottom device in the cascode structure (i.e., Q_1 in Fig. 59), and L_E is the emitter inductor selected in the previous step. The value of L_B was chosen by sweeping L_B in an S-parameter simulation until the reactive component of the input impedance was canceled. This resulted in L_B values of around 2.38 nH and 2.2 nH for the *npn* and *pnp* designs, respectively.

Adding a Collector Resistor Because the output impedance of the cascode structure is high, output matching can be very difficult. A collector resistor can be added to, not only ease output impedance matching, but also to improve stability, at the cost of reducing peak gain. For both designs, a collector resistor of 500 Ω was chosen as it resulted in reasonable inductor values for output matching. Note that another possible choice would have been to choose the resistors so that the LNAs had the same gain at 5 GHz. To achieve the same gain, the resistor of the *pnp* LNA would have to be much larger, the bandwidth of the output matching network would be reduced, and there is a higher potential for the circuit to be unstable. The implications of having matched gain are discussed in Section 4.3.5. For the rest of the discussion in this section, the same resistor values of 500 Ω are used instead.

Implementing Output Match The output impedance matching is realized by using an L-network with a shunt inductor (L_C) and a series capacitor (C_C). These values were selected using S-parameter simulations. The values for L_C were around 2.38 nH and 2.15 nH for the *npn* and *pnp* designs, respectively. The series capacitors, which also serve as a DC block for the following stage, resulted in values of 300 fF

and 270 fF for the *npn* and *pnp* designs, respectively.

Finalizing the Design The cascode core was biased using a current mirror with ratio 1:4 for the *npn* LNA and 1:5 for the *pnp* LNA. The bias resistors, R_{B1} and R_{B0} were designed to also have these ratios to correct for differences in base current between the core and the current mirror. The resistor R_{B1} also serves as an RF choke and was chosen to be 2.5 kΩ. The bias resistors R_{BIAS} were selected to be 1.15 kΩ and 1.8 kΩ for the *npn* and *pnp* designs, respectively. A 10 Ω resistor was added on the upper-base node of each circuit to improve stability to potential oscillation. The stability of both circuits was verified using the S-Probe technique, also known as the Gamma-Probe technique [129].

4.3.2 Simulated Circuit Performance

After the designs were complete, the performance of both circuits was simulated using Keysight's ADS. The simulated S-parameters of the designed circuits are shown in Fig. 62. Both circuits achieve an input and output return loss (S_{11} and S_{22}, respectively) lower than 10 dB at the center frequency, and a reverse isolation (S_{12}) greater than 30 dB across the simulated frequencies. The main differences between both designs lie in the gain (S_{21}). Using the same design procedure, the *npn* LNA achieved a gain of 18.0 dB, while the *pnp* LNA achieved a gain of 14.8 dB at 5 GHz. This result is not surprising since the maximum available gain of the *npn* LNA core at the selected bias, was larger than that of the *pnp* core. Even though the *pnp* LNA has lower gain, it also shows a lower input-referred P1dB compression point by 1 dB, as shown in Fig. 63.

The simulated NF as a function of frequency is shown in Fig. 64. The *npn* LNA shows a NF of 1.7 dB at 5 GHz, while the *pnp* LNA shows a NF of 2.1 dB at the same frequency, a difference of 0.4 dB.

While the *npn* design exhibits better performance in almost every RF metric, it

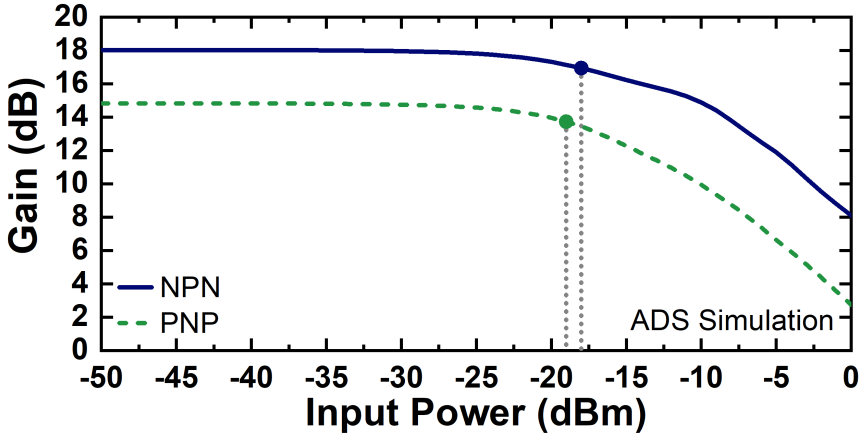

Fig. 63: Comparison of simulated single-tone linearity for the designed low-noise amplifiers.

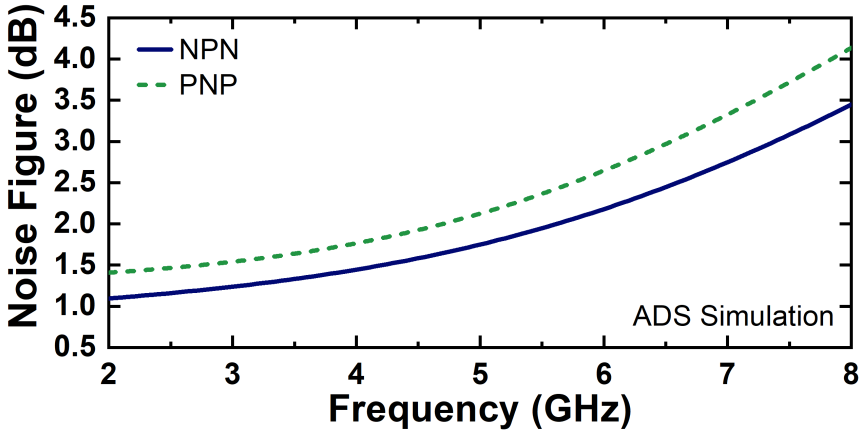

Fig. 64: Comparison of simulated noise figure for the designed low-noise amplifiers.

also consumes more *dc* power with a total of 9.6 mW compared to 6.8 mW for the *pnp* design. A summary of the RF performance of both circuits is shown in Table 8. It is worth noting that, although some of these metrics could be improved by selecting a different topology, bias, or layout scheme, the purpose of this study is to obtain circuits with good performance that were designed following the same procedure, thus ensuring a fair comparison.

4.3.3 Mixed-Mode TCAD Simulations

2-D TCAD models have been developed using the Synopsys TCAD suite and calibrated to match the *dc* characteristics of the Cadence IHP SG25H3P process design

Table 8: Comparison of Performance Metrics for LNAs Designed With *npn* and *pnp* SiGe HBTs.

Specification	*npn* LNA	*pnp* LNA
Center Frequency	5 GHz	5 GHz
Noise Figure at 5 GHz	1.7 dB	2.1 dB
Gain (S_{21}) at 5 GHz	18.0 dB	14.8 dB
Input P1dB	-18 dBm	-19 dBm
Supply Voltage	2 V	-2 V
P_{DC}	9.6 mW	6.8 mW

kit (PDK) compact models. In addition, the models have been calibrated to show the relative improvement in SET response of *pnp* devices compared to *npn* devices. For this calibration, we used laser-induced transients measured at the U.S. Naval Research Laboratory. A detailed description of the experimental setup and additional results obtained for these devices can be found in [34]. Fig. 65 shows the comparison between measured and simulated transients in the collector terminal. The transients have been normalized to the maximum amplitude of the *npn* transients for comparison. Note that a similar amplitude reduction was obtained in measurement and simulation when comparing *pnp* and *npn* transients. The amplitude of the SETs for the *pnp* devices was smaller than the *npn* devices across all simulated LETs, as shown in Fig. 66.

One drawback of using 2-D TCAD models is that the diffusion component present in the experimental data cannot be accurately captured. However, since the diffusion component of the *npn* devices is larger than the *pnp* devices (shown in Fig. 65a), this suggests that the simulation results shown in this section are underestimating the improvement obtained from using *pnp* devices. In addition, the model does not capture any charge sharing that occurs between adjacent devices. For the *pnp* device, any charge that diffuses through the substrate will be collected by the n-well, and will have a smaller impact on the collector terminal [34]. Thus, this is another source of error that would be underestimating the difference in the SET response between

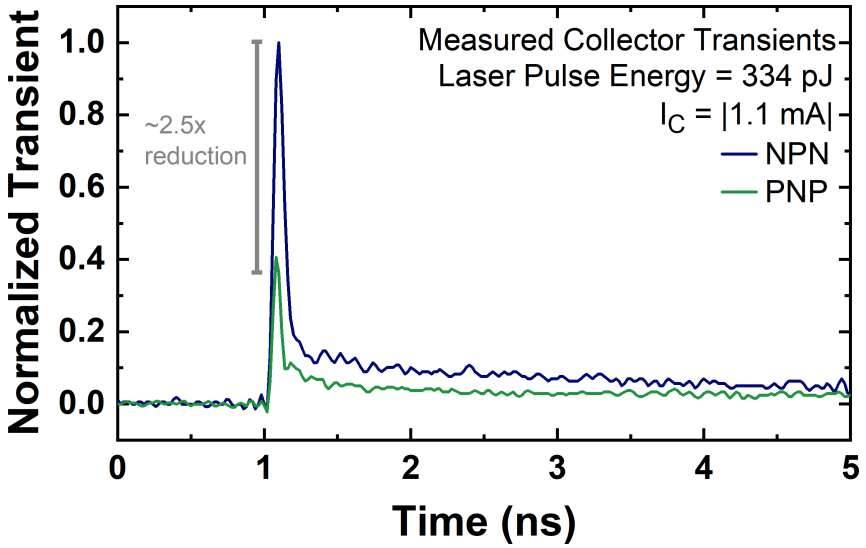

(a) Measurement Results

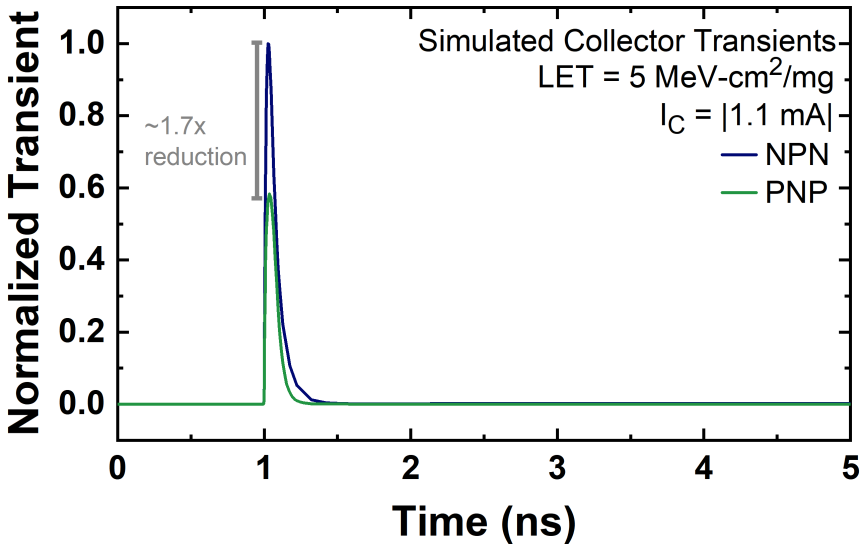

(b) Simulation Results

Fig. 65: Comparison of measured and simulated transients for individual *npn* and *pnp* SiGe HBT devices.

npn and *pnp* devices.

The calibrated models were then used to perform mixed-mode heavy-ion simulations, in which the TCAD model of the struck device is solved self-consistently within the operating RF circuit. In this type of simulation, a physics-based transistor model is placed in a circuit netlist. The circuit equations and physics-based device equations are solved simultaneously.

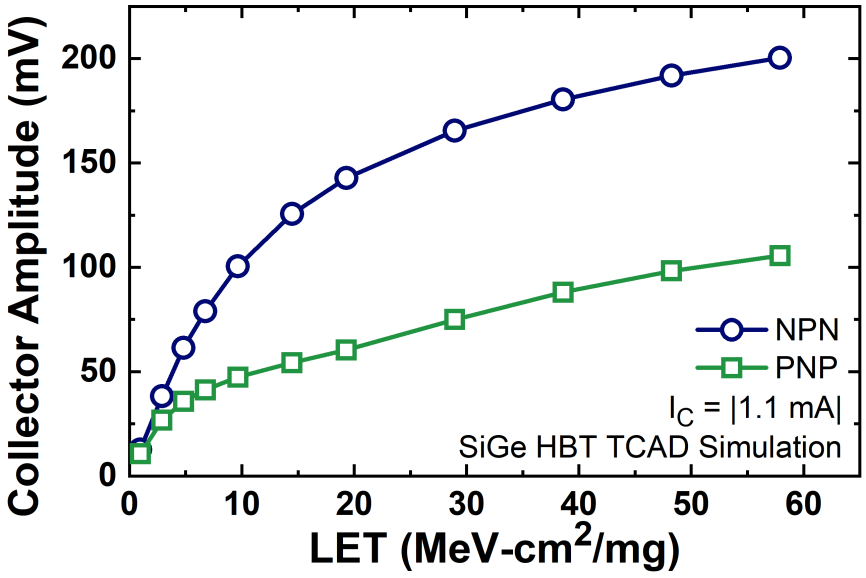

Fig. 66: Peak amplitude of simulated transients as a function of linear energy transfer when a simulated heavy ion passes through the *npn* and *pnp* devices.

In these simulations, both the input and output were terminated with 50 Ω, and the induced transients are measured at the output node of the LNAs. Fig. 67 shows the output transient for both designs when a simulated heavy ion with an LET of 10 MeV-cm^2/mg passes through the common-emitter device of each LNA. The data show a 1.9× reduction in transient peak for the *pnp* heavy-ion strikes compared to strikes on equivalent *npn* devices. Note that the resulting decrease in transient peak is not a result of the reduced gain in the *pnp* LNA. During a heavy-ion strike, the struck device is flooded with carrier densities that are comparable to the doping levels in the device. Therefore, typical transistor behavior is not expected during this time. Instead, previous work has shown that the improvement stems from the presence of the n-well in the *pnp* devices [34]. It is important to mention that the transients produced by each circuit will have a similar shape, since this is determined by the output matching network [7], but opposite polarity due to the change in power supply polarity. In Fig. 67, the polarity of the *npn* SET has been inverted.

To explore the effects of heavy-ion linear energy transfer (LET) on the produced SETs, the LET was swept in simulation. All heavy-ion-induced transients had a

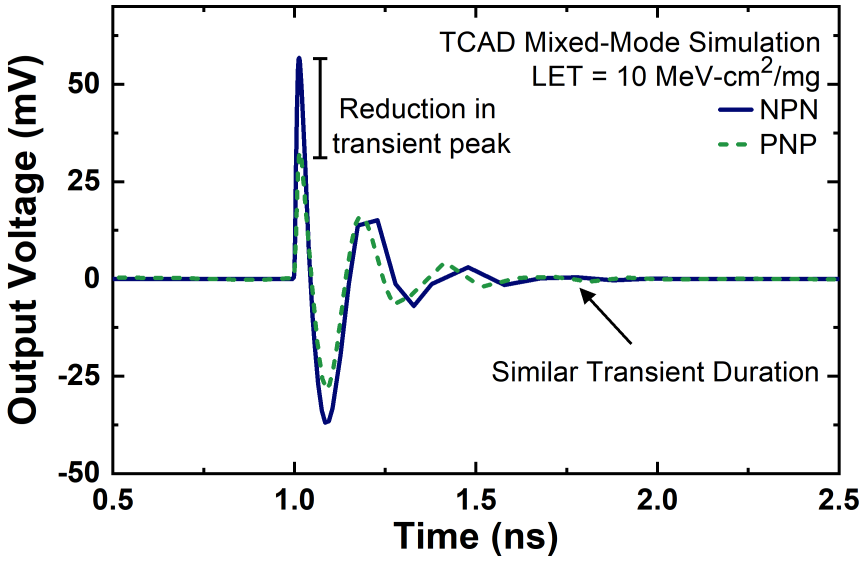

Fig. 67: Comparison of single-event transient captured at the output of the low-noise amplifiers when a simulated heavy ion with an LET of 10 MeV-cm^2/mg passes through the common-emitter device.

similar shape to that shown in Fig. 67, and their individual plots have been omitted for brevity. Fig. 68 shows the peak to peak amplitude of the SETs as a function of LET. As expected, the amplitudes monotonically increase with increasing LET, and begin to saturate as the device and circuit non-linearities begin to limit the response. The data show that the transient peaks produced by strikes on the *pnp* circuit are significantly lower than those produced by strikes on the *npn* circuit across all simulated LETs. In addition, the collected charge for both circuits monotonically increases with increasing LET and is lower for the *pnp* LNA when compared to the *npn* LNA across all simulated LETs.

These results show that the *pnp* LNA will be more robust to SETs compared to the *npn* LNA designed using the same procedure. This increased robustness, however, comes at the cost of circuit performance. Thus, in the context of RF communications systems, the impact of these transients on modulated data must be examined.

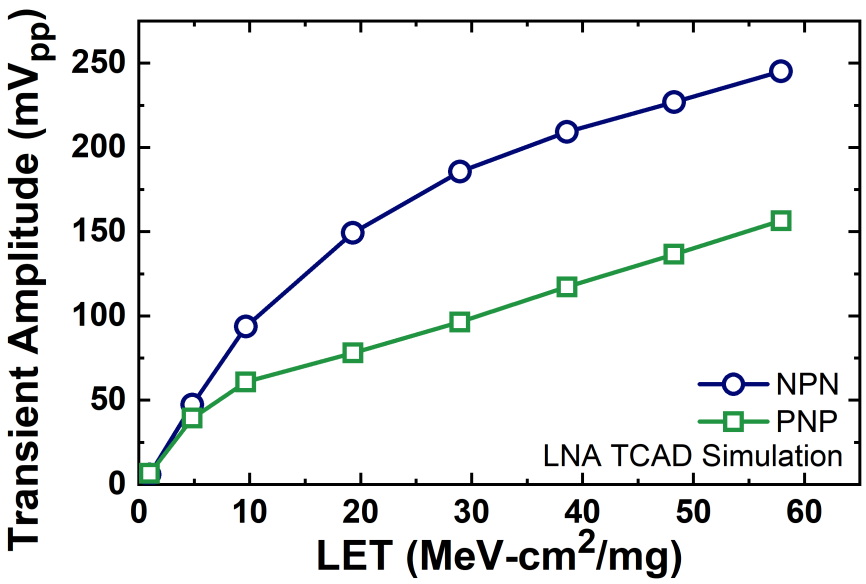

Fig. 68: Peak-to-peak amplitude of simulated transients as a function of linear energy transfer when a simulated heavy ion passes through the common-emitter device of the *npn* and *pnp* LNAs.

4.3.4 Impact of SETs on Modulated Data

To verify how SETs impact modulated data in an RF communications systems, additional simulations following the approach in Chapter 3 were performed. In this section, two modulation schemes are considered: QPSK and 16-QAM.

A data flow simulation was performed in ADS using either an ideal QPSK or QAM modulator connected through an ideal channel to the input of the designed LNAs. The RF signal was downconverted by a pair of ideal mixers with a conversion gain of 10 dB, and no additional noise contribution. All simulations were performed with the same pseudo-random bit stream of 1,000 symbols at a symbol rate of 100 MBd, which is used to generate the constellation diagrams for comparison. The data was modulated on a 5 GHz carrier with a signal power of -35 dBm. A periodic SET current was injected to the nodes of the common emitter device of the LNAs and the pulse was repeated such that one SET was injected per received symbol. The current source was implemented in ADS by specifying time-current pairs in an ideal current source component. The current sources were then connected between each

of the HBT device terminals (i.e., collector, base, emitter) and ground. The SET waveforms were obtained from the mixed-mode heavy-ion strike TCAD simulations shown in the above sections. The limitations of this approach have been previously discussed [6], but it is an effective way to make comparisons between two RF systems.

The results of these simulations are shown in Fig. 69 for QPSK and in Fig. 70 for 16-QAM. All of the constellation diagrams shown in this section been normalized to the *npn* constellation without any SETs (i.e., all received signal amplitudes were divided by A_c of the *npn* simulations). This normalization simplifies the comparison of the results. In these diagrams, the magenta crosses represent the ideal position of the received symbols without any distortion due to circuit performance or SETs. The vertical and horizontal dashed lines represent the symbol decision boundary. If an SET causes a symbol to cross these lines, the symbol will be corrupted, which would be equivalent to a single- or multiple-bit upset (depending on which line is crossed and the bit encoding scheme). Note that for the 16-QAM modulation scheme, the decision boundaries for the *npn* circuits has been drawn. Since these results are normalized, the decision boundaries for the *pnp* would be slightly different. However, for the purpose of comparing potentials for data corruption, the *npn* decision boundary will be used in the discussion below. The use of the *npn* decision boundary for both cases is equivalent to assuming that the readout circuitry in a real system, which contains analog-to-digital converters to make the decisions, will be the same in both systems.

Fig. 69a shows the QPSK constellation diagram for both LNAs without any SETs present. The diagram shows a smaller constellation for the *pnp* LNA, which is consistent with the lower gain of the circuit. The QPSK constellations resulting from ion strikes with an LET of 10 and 30 MeV-cm^2/mg are shown in Fig. 69b and Fig. 69c, respectively. At first glance, the data going through the *npn* LNA appears to be affected less compared to the *pnp* data for an LET of 10 MeV-cm^2/mg. However,

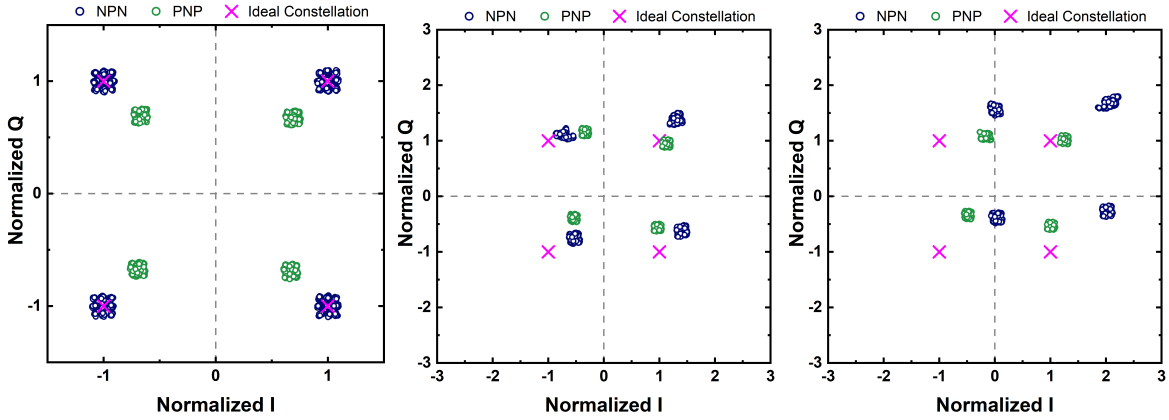

(a) No SETs **(b)** LET = 10 MeV-cm^2/mg **(c)** LET = 30 MeV-cm^2/mg

Fig. 69: Constellation diagrams for QPSK modulated data on both the *npn* and *pnp* LNAs (a) without SETs, and when an ion passes through the common emitter of each LNA for an LET of (b) 10 MeV-cm^2/mg, and (c) 30 MeV-cm^2/mg. All the received symbols have been normalized to the amplitudes of the received symbols for the *npn* design without SETs.

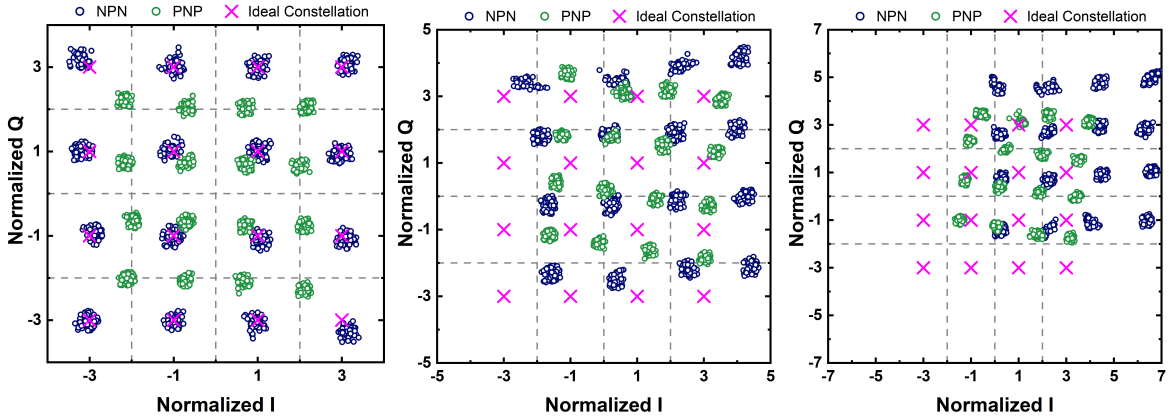

(a) No SETs **(b)** LET = 10 MeV-cm^2/mg **(c)** LET = 30 MeV-cm^2/mg

Fig. 70: Constellation diagrams for 16-QAM modulated data both the *npn* and *pnp* LNAs (a) without SETs, and when an ion passes through the common emitter of each LNA for an LET of (b) 10 MeV-cm^2/mg, and (c) 30 MeV-cm^2/mg. All the received symbols have been normalized to the amplitudes of the received symbols for the *npn* design without SETs.

because the *pnp* constellation starts with a smaller amplitude, the shift in the symbols is actually larger for the *npn* circuit. For the constellation with an LET of 30 MeV-cm^2/mg, the symbols for the *npn* cross the decision boundary, resulting in bit upsets, whereas the *pnp* constellation still has some margin that prevents upsets.

The 16-QAM constellation diagram for both LNAs without any SETs present are shown in Fig. 70a. The 16-QAM constellations resulting from ion strikes with an LET of 10 and 30 MeV-cm^2/mg are shown in Fig. 69b and Fig. 69c, respectively. The behavior of the constellations are qualitatively similar to those observed for the QPSK simulations. One thing to note is that, for the same power of the RF carrier, it is easier in 16-QAM modulation than QPSK for distortions or interference to cause the symbols to cross the decision boundaries. For the constellations of the no SET case, the normalize data show that the symbols produced by the *pnp* LNA are close to the decision boundary. This result is not surprising due to the lower gain of the *pnp* LNA. For the constellation resulting from ion strikes with an LET of 10 MeV-cm^2/mg, the majority of the symbols produced by the *pnp* LNA have crossed the decision boundary, while the majority of the symbols produced by the *npn* LNA have not. The constellations resulting from ion strikes of an LET of 30 MeV-cm^2/mg show symbols crossing the decision boundaries for both the *npn* and *pnp* circuits. These results show that the *pnp* LNA would be more susceptible to heavy ion strikes for 16-QAM modulation compared the *npn* LNA, when the RF power of the carrier is fixed.

The main takeaway from the results is that the *npn* LNA is more susceptible to producing bit upsets when compared to the *pnp* LNA for QPSK, while the reverse is true for 16-QAM. In these results, the *npn* constellation started off with more margin between the received symbols and the decision boundaries, which tends to make circuits more robust to interference or noise. However, because the transients in the *npn* LNA are much larger than those in the *pnp* LNA, it is still easier to corrupt the data in the *npn* design for QPSK modulation. However, for 16-QAM modulation, the margin between the decision boundary and the symbols for the *pnp* LNA is small enough such that ion strikes with low LET will corrupt the data. Thus, the robustness of the *pnp* LNA compared to the *npn* LNA will depend on the circuit performance

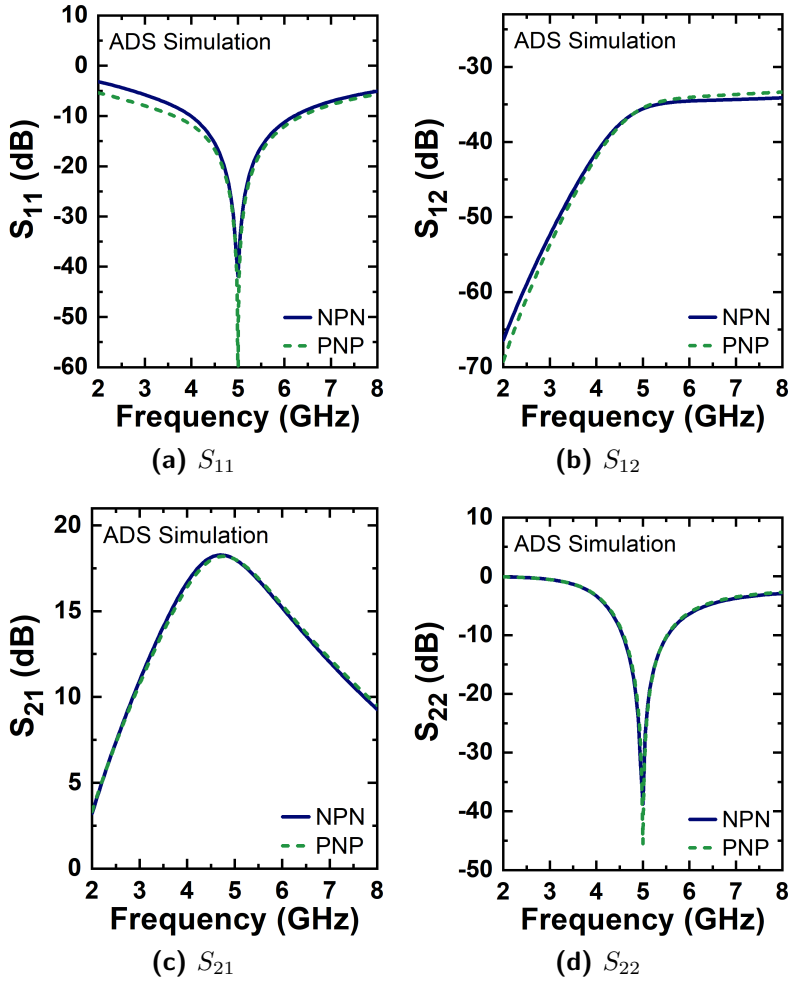

Fig. 71: Comparison of simulated S-parameters for the designed low-noise amplifiers where the *pnp* LNA was re-designed to match the gain of the *npn* LNA at 5 GHz.

and modulation scheme. A similar comparison for two circuits with matched gain is performed below.

4.3.5 Matched-Gain LNAs

To compare the SET response of these two circuits when they have the same gain, the *pnp* circuit was re-designed to closely match the S-parameters of the *npn* LNA. For this design, the transistor core was maintained the same and the bias current was increased to improve the gain of the circuit at the expense of power consumption and NF. The following design values were used: J_C = 963 μA, L_E = 232 pH. L_B = 2.04 nH, R_C = 307 Ω, L_C = 1.96 nH, and C_C = 336 fF. The performance of the

new *pnp* LNA is compared to that of the original *npn* LNA in Fig. 71. Note that the S-parameters of the two circuits are now almost identical. The NF of new *pnp* LNA is 2.5 dB, which is 0.8 dB higher than the *npn* design.

The same simulation procedure was performed for this new LNA, including mixed-mode TCAD simulations and constellation diagrams. The resulting constellations are shown in Fig. 72. The constellation for the case without SETs, shown in Fig. 72a, now shows that both LNAs have the same gain, as evidenced by the overlapping symbols from both amplifiers. In this case, the symbols at the output of both designs have the same amplitude after being downconverted. The results for the simulations with an ion strike of an LET = 10 MeV-cm^2/mg show that when the amplitudes of the symbols start being the same, the SETs will affect the *npn* design slightly more than the *pnp* design because the transients generated by the *npn* SiGe HBTs are larger. This result demonstrates that the robustness to SETs of the original *pnp* LNA does not originate from the lower gain. Finally, and similar to the results for the other *pnp* LNA, the results for ion strikes with an LET = 30 MeV-cm^2/mg also show that the *pnp* LNA has some margin between the received symbols and the decision boundary. Thus, even for matched-gain LNAs the *pnp* design shows a smaller transient response when there is RF data through the system.

4.3.6 Discussion

The presented results show that, within the context of RF circuits, *pnp* devices still show increased robustness to SETs by exhibiting lower transient peaks and collected charge across all simulated LETs. However, the performance for the circuit designed with *pnp* devices is also lower than that of one designed with *npn* devices. This was not the case circuits shown in previous work [120] because their frequency of operation was too low to show major discrepancies in performance. At these higher frequencies, the LNA resulting from using only *pnp* devices has lower gain, higher noise figure,

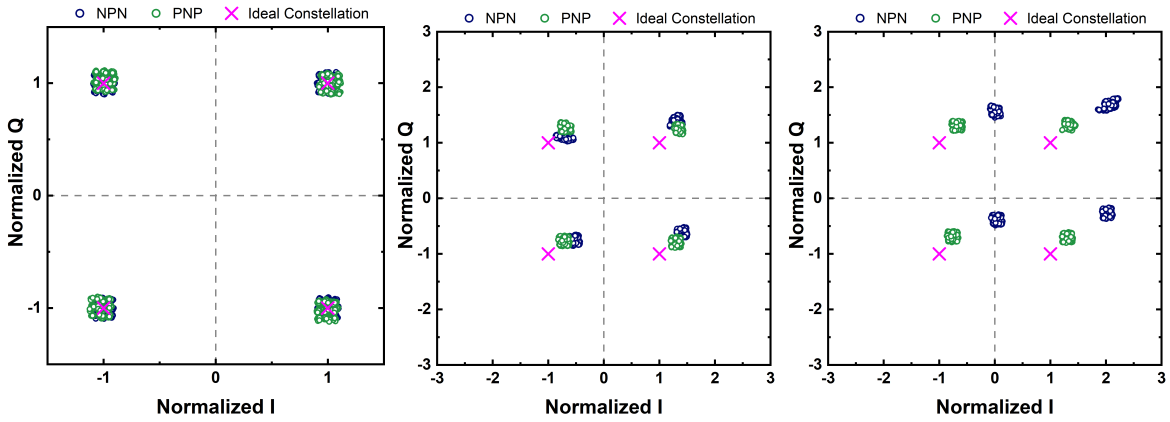

(a) No SETs **(b)** LET = 10 MeV-cm^2/mg **(c)** LET = 30 MeV-cm^2/mg

Fig. 72: Constellation diagrams for both the *npn* and *pnp* LNA (with matched gain) (a) without SETs, and when an ion passes through the common emitter of each LNA for an LET of (b) 10 MeV-cm^2/mg, and (c) 30 MeV-cm^2/mg. All the received symbols have been normalized to the amplitudes of the received symbols for the *npn* design without SETs.

and lower P1dB. Even the redesigned *pnp* LNA with the same gain had higher noise figure and lower bandwidth than the *npn* design. Given that higher noise figure can have a negative impact on satellite link performance [130], a natural question results: Is the added robustness to heavy-ion phenomena worth the decrease in circuit performance for these designs? The answer to this question depends on several factors, including the radiation environment, type of received data, and required receiver RF performance, and thus will ultimately be determined by the specifications of the intended application. Although the *pnp* LNA has lower performance than the *npn* LNA, it also consumes less *dc* power. Ultimately, the choice would depend on the system specifications.

In this section, only single-stage LNA designs were considered. However, for certain applications, multi-stage LNAs might be needed to meet the required gain or bandwidth specifications. In such designs, both *npn* and *pnp* devices can be leveraged in the same design to make a conscious tradeoff between RF performance and SET robustness. For example, in a multi-stage LNA, the first stage can be

designed using *npn* devices to provide lower NF and higher gain compared to the *pnp* design. The higher gain will serve to suppress the NF of subsequent stages, and the overall NF of the receiver. The remaining stages can be designed using *pnp* devices which will have higher NF but smaller SET response. With the additional choice of *pnp* devices, designers have an additional parameter to tune the LNA performance and SET robustness.

4.4 Utilizing Silicon-On-Insulator Platforms to Mitigate Single-Event Transients

Another approach for mitigating SEEs in circuits and systems is the use of silicon-on-insulator (SOI) platforms. SiGe HBTs built on SOI platforms exhibit lower charge collection compared to similar devices on bulk substrates since the buried oxide (BOX) serves to limit the diffusion of charge deposited in the substrate to sensitive junctions [70].

Several studies have compared the SEE response of SiGe HBTs on SOI and bulk substrates [35, 70, 71, 131]. However, many of these previous studies have been limited in scope, focusing either on charge collection measurements or presenting single-event transient (SET) data for limited values of heavy-ion linear energy transfer (LET). Furthermore, all of the studies found in the literature present results only from experimental lots that are not commercially available to designers, thus limiting their availability for mitigating SEEs.

The primary goal of this section is to provide a comparison of heavy-ion-induced SETs in SiGe HBTs on commercially-available bulk and SOI platforms. Laser-induced transients in a similar platform are used to provide more insight into some of the results obtained from heavy-ion data. In addition, TCAD simulations are employed to investigate the internal mechanisms that lead to some of the more interesting measured responses. Finally, the implications of having the same devices on bulk and SOI in the context of ion/laser correlation are discussed.

Table 9: Summary of Experimental Conditions for Heavy-Ion Data Taken at LBNL for Jazz Bulk SiGe HBT.

Device	Bulk					
Bias	GND			Biased		
Ion	Ar	Kr	Xe	Ar	Kr	Xe
Z	18	36	54	18	36	54
A	40	86	124	40	86	124
Energy (MeV)	400.00	885.59	1232.55	400.00	885.59	1232.55
SRIM LET* (MeV-cm^2/mg)	10.4	33.0	63.0	10.4	33.0	63.0
Range (μm)	112.0	91.7	71.9	112.0	91.7	71.9
Flux (10^5 ions/cm^2·s)	1.84	2.00	1.90	1.84	1.71	2.10
Eff. Fluence (10^8 ions/cm^2)	7.94	3.47	3.19	6.69	3.71	2.47
# of Events	436	491	509	436	472	527

4.4.1 Heavy-Ion and Laser Testing

The heavy-ion-induced transients were measured at the 88-inch cyclotron BASE Facility at Lawrence Berkeley National Laboratory (LBNL) using the 10-MeV/amu heavy-ion cocktail across multiple LETs ranging from 10.4 MeV-cm^2/mg to 63.0 MeV-cm^2/mg. The experimental conditions used to generate the ion data for bulk and SOI samples are given in Tables 9 and 10, respectively. The LETs throughout this section are taken to be the LETs calculated using SRIM [85] at the silicon surface after the ion passes through the back-end-of-line metals and dielectrics. These LET values were used in the estimation of the RPP thickness of each sample. A total of 10,000 ions were simulated to obtain these LET values.

Laser-induced transients on the RF circuits were measured at the U.S. Naval Research Laboratory (NRL) using the through-wafer two-photon absorption (TPA)

Table 10: Summary of Experimental Conditions for Heavy-Ion Data Taken at LBNL for Jazz SOI SiGe HBT

Device	SOI						
Bias	GND				Biased		
Ion	Ar	Ar	Y	Xe	Ar	Ar	Xe
Z	18	18	39	54	18	18	54
A	40	40	89	124	40	40	124
Energy (MeV)	400.00	400.00	928.49	1232.55	400.00	400.00	1232.55
SRIM LET* (MeV-cm^2/mg)	10.4	10.4	37.6	63.0	10.4	10.4	63.0
Range (μm)	112.0	112.0	84.1	71.9	112.0	112.0	71.9
Flux (10^5 ions/cm^2·s)	3.05	70.0	2.40	1.35	1.80	70.0	0.71
Eff. Fluence (10^8 ions/cm^2)	9.73	42.0	6.35	10.3	16.6	105	4.00
# of Events	102	176	35	101	104	433	105

experimental setup explained in detail in Section 2.2. For this particular experiment, the focused spot size was approximately 1 μm.

At LBNL, the induced SETs were captured using a Tektronix DPO71254, which is a 12.5 GHz bandwidth real-time oscilloscope capable of capturing 50 GS/sec. At NRL, SETs were captured using a 23 GHz Tektronix MSO72304DX real-time oscilloscope configured to capture 50 GS/sec.

4.4.2 Sample Selection

The SiGe HBTs used for heavy-ion testing were fabricated by TowerJazz using two commercially-available processes: SBC18H3A (bulk) and SBC18H3B (SOI) processes, referred to in this work as Jazz H3 bulk and Jazz H3 SOI, respectively. These processes feature high-speed SiGe HBTs with f_T/f_{max} of 240/280 GHz [132]. The SOI devices were fabricated on a thick-film SOI, allowing for traditional subcollector design to

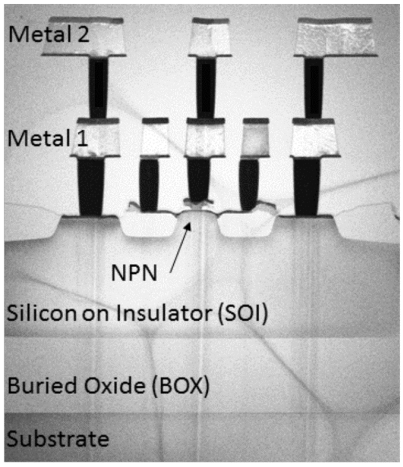

Fig. 73: Cross-section TEM micrograph of an *npn* SiGe HBT built on thick-film SOI (reproduced from [4]).

achieve maximum performance. A cross-section of the SOI SiGe HBT is shown in Fig. 73. The thick film (approximately 2 μm thick) allows for the intrinsic devices on SOI to possess very similar performance to devices built on a bulk substrate, facilitating a direct comparison between their respective SET responses. More details on the performance of these devices have been published elsewhere [132]. The emitters of all the H3 SiGe HBTs selected for testing have an area of $0.13 \times 10\ \mu m^2$, except where noted below.

SiGe HBTs have a compositionally graded SiGe alloy in the base. A laser wavelength of 1260 nm would generate carriers via TPA in Si and single-photon absorption (SPA) in Ge. Since significantly more carriers can be generated using SPA than TPA for the same laser pulse energies in these materials, the existence of SPA in the base of these samples would be problematic as it would lead to highly-localized charge generation in the intrinsic base of the device. The exact composition of the SiGe alloy for most SiGe processes is proprietary. However, a similar Jazz process has been reported to have a maximum Ge concentration of approximately 30% [133]. Using the equations in [134], the bandgap for a $Si_{0.7}Ge_{0.3}$ alloy would be approximately 1 eV at 300 K. The photon energy for a 1260 nm wavelength is 0.98 eV, which is below

the bandgap of a $Si_{0.7}Ge_{0.3}$ film. To generate carriers via SPA, the Ge concentration must be greater than 35%, which is considered to be an aggressive profile for these types of devices and could lead to issues with film stability. Thus, there is no concern for carrier generation via SPA in these particular samples.

The data shown in this section were acquired from testing one sample at NRL and a different sample at LBNL, for each process variant (i.e., bulk and SOI) and emitter geometry used. Since no additional polishing of the back of the die was performed (other than the standard foundry polish), multiple samples were measured at NRL to determine whether this would introduce sample-to-sample variation due to surface roughness. Although not included in this section, the differences observed between samples were within the uncertainty in experimental calibration and the results were consistent over multiple days of testing.

4.4.3 Results from Heavy-Ion Data

One of the main differences between bulk and SOI SiGe HBTs, in the context of radiation effects, is their charge collection volume. First, the heavy-ion cross-section for bulk SiGe HBTs has been shown to increase slightly with LET, foregoing the typical saturation behavior observed in other semiconductor platforms [121]. This increase is due to charge collection from diffusion processes that take place when highly-energetic ions deposit charge far away from the intrinsic device (e.g., outside of the confines of the deep trench isolation, or deep into the substrate). Since SiGe HBTs are known to collect charge deep within the substrate [70], adding the BOX will quench these diffusive charge collection processes, and should decrease the sensitive volume depth to the thickness of the SOI. To verify these assertions, heavy-ion data at three different LETs were taken for both the bulk and SOI samples.

The event cross-section when all terminals of the device are grounded is shown in Fig. 74a, which is calculated by dividing the number of SETs by the total fluence for

each ion. The shaded region represents the interpolation of the 95% confidence level calculated for a Poisson distribution based on the number of events. The data show a significant reduction in the event cross-section. For the SOI samples, the cross-section is smaller than the area contained within the deep trench, and is reduced to the approximate size of the intrinsic device (i.e., emitter/base/collector stack). The drastic reduction in cross-section area is unexpected since both devices have the same area in the layout. This result indicates that charge collection on the extrinsic device results only from the subcollector/substrate junction. Since this junction is removed by adding a BOX in the SOI SiGe HBTs, the results suggest that there is no charge collection outside of the intrinsic device for the SOI samples. These results will be confirmed using pulsed-laser data below.

The sensitive volume thickness, according to the rectangular parallelepiped (RPP) approximation, is shown in Fig. 74b. During these measurements, all terminals for the devices were grounded. For a more accurate extraction of RPP thickness, the heavy-ion deposited charge values have been calculated using SRIM and take into account the effects of the back-end-of-line layers on top of the intrinsic device (i.e., metals, inter-metal dielectrics and passivation layers). There are a number of implicit assumptions in this calculation [135]. The first two assumptions are that the energy deposited in the material is equal to the energy loss or LET of the the ion, and that the LET is constant throughout the thickness of the sensitive volume. These two assumptions allow for the use of a constant charge deposition rate. The third assumption is that the sensitive volume thickness does not change with LET. With these assumptions, the collected charge will be the product of the charge deposition rate and the RPP thickness. Thus by plotting collected charge as a function of charge deposition rate, the RPP thickness can be extracted from the slope of the resulting line.

The data shown in Fig. 74b show a significant reduction in the RPP thickness

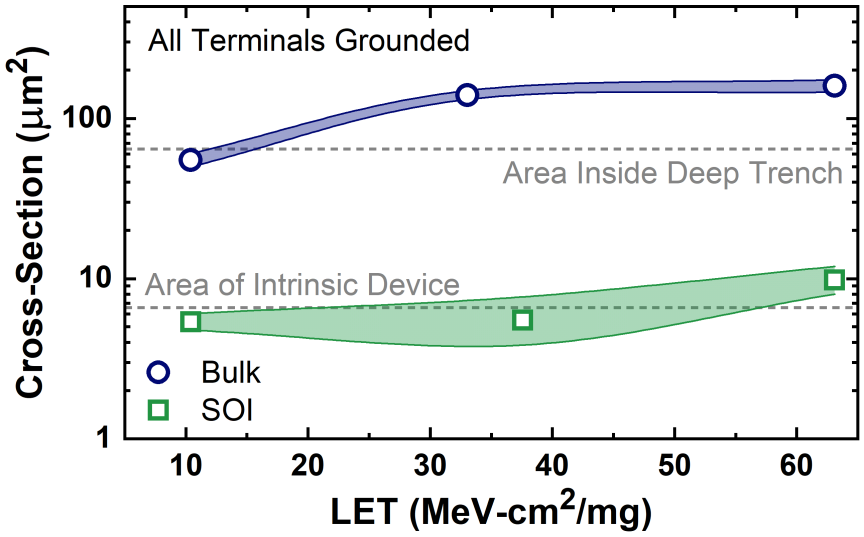

(a) Cross-section Area

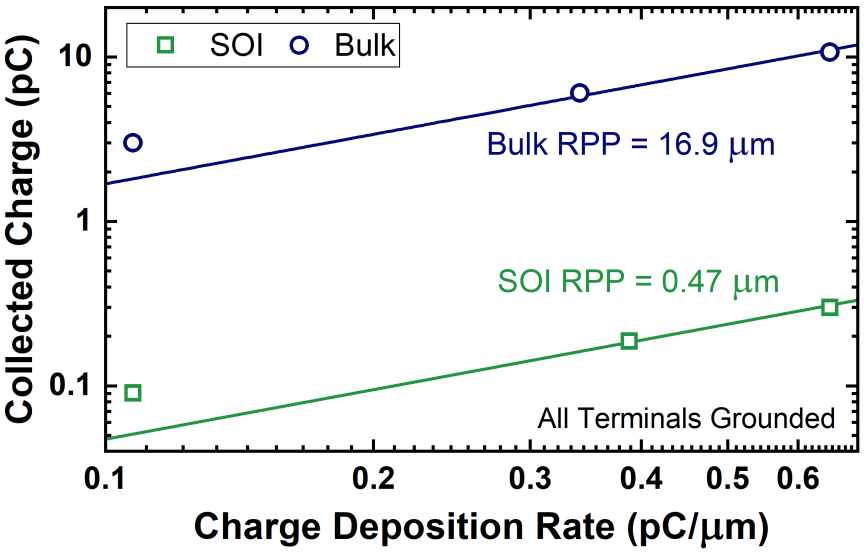

(b) Sensitive Volume Depth

Fig. 74: Comparison of (a) cross-section and (b) sensitive volume depth (RPP) for bulk and SOI SiGe HBTs with all terminals grounded extracted from heavy-ion data. The shaded region in the cross-section shows an interpolation of the 95% confidence level.

for SOI devices compared to those on a bulk substrate. Interestingly, the extracted RPP thickness of 0.47 μm for the SOI devices is smaller than the thickness of the SOI film, which is approximately 2 μm. This difference suggests that the charge deposited inside of the subcollector recombines before it reaches the collector terminal. This result will be verified using TCAD simulations below.

Overall, the sensitive volume of the SOI SiGe HBTs is much smaller than the sensitive volume of the bulk devices. In fact, the sensitive volume for the bulk devices is $\approx 350\times$ that of the SOI devices for the emitter area used in this study. Clearly, the significant reduction of sensitive volume for SOI devices is advantageous from an SEE vulnerability perspective.

The difference in RPP thickness, which results from the suppression of the collector/substrate diffusion component, is most apparent when comparing the worst-case (i.e., largest amplitude) SET waveforms. A comparison of worst-case SETs is shown in Fig. 75 for the case when all device terminals are grounded and in Fig. 76 for the case when the device is biased with $V_C = V_B = 0.8\ V$ and $V_E = V_{Sub} = 0\ V$. The collector transients for the bulk device show an extended "tail" that is not observed in the transients for the SOI device. Despite the large differences in collected charge, it is relevant to note that the transient peak amplitudes are similar between both samples for the bias conditions shown. This result is rather unexpected, partly due to the difference in RPP thickness. Given the significant difference between these waveform shapes, it is pertinent to examine the statistical distribution of collected charge and transient peaks resulting from heavy-ion experiments.

Figs. 77a and 77b show the relative frequency of measured collected charge and transient peaks, respectively, when the samples were exposed to Ar ions (LET $\approx$ 10.4 MeV-cm^2/mg) were biased with $V_C = V_B = 0.8\ V$ and $V_E = V_{Sub} = 0\ V$. The number of events recorded for the devices on bulk and SOI were 444 and 375, after an accumulated fluence of 6.7×10^8 cm^2 and 12.2×10^9 cm^2, respectively. Note that the number of recorded events is slightly different than the total number of events in Tables 9 and 10. This discrepancy is a result of the time required to save the data for further analysis. The software used for this purpose was able to count the events but not save all the transient waveforms. Thus, the event count was used to calculate the event cross-section and the number of recorded events was used in the histograms

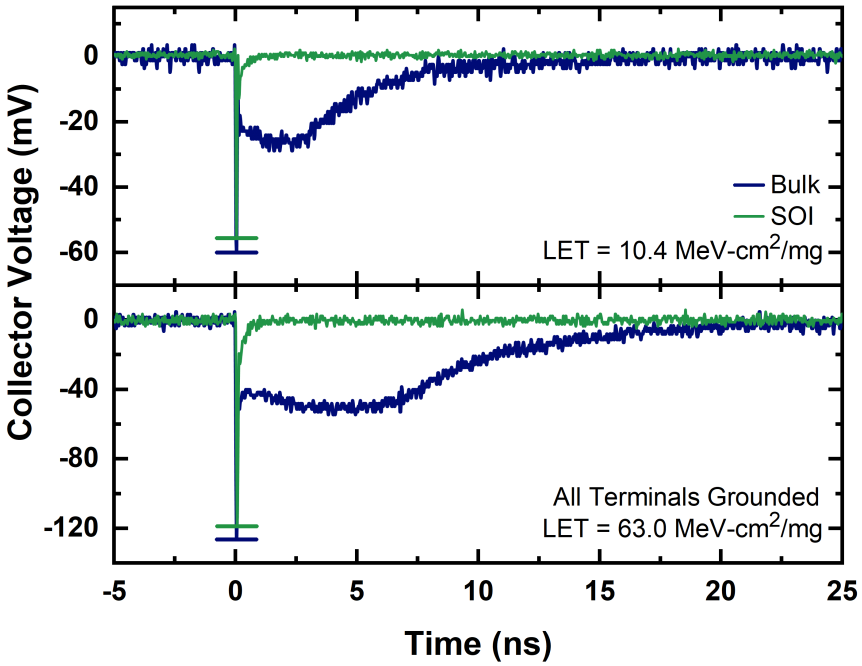

Fig. 75: Measured collector transients in SiGe HBTs on bulk and SOI for Ar (top) and Xe (bottom) ion beams when all terminals on the device were grounded. The horizontal lines indicate the transient peak amplitude for each waveform.

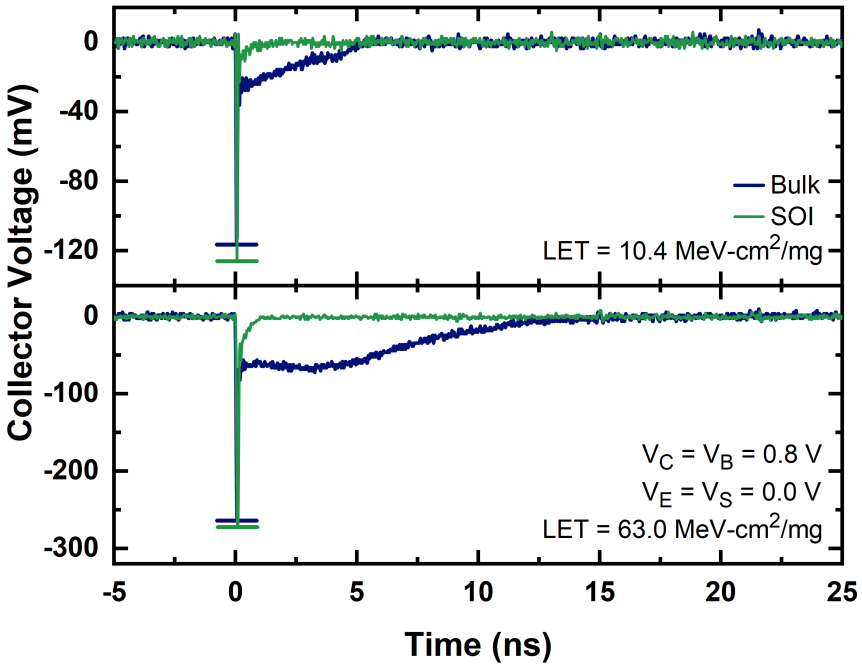

Fig. 76: Measured collector transients in SiGe HBTs on bulk and SOI for Ar (top) and Xe (bottom) ion beams when the device was biased with $V_C = V_B = 0.8\ V$ and $V_E = V_{Sub} = 0\ V$. The horizontal lines indicate the transient peak amplitude for each waveform.

shown in Figs. 77a and 77b. The data for collected charge show large differences in both the mean and the standard deviation of the collected charge between bulk and SOI devices. The devices on bulk substrate show larger collected charge values resulting from the diffusion tail of the transients. Interestingly, the transient peaks for this ion show high occurrence of events around 40 mV for the bulk device, but an almost uniform distribution for the SOI device.

Note that the bias condition used for the data in the histograms in Fig. 77 is different than for the data shown in Fig. 74. Due to limitations in beam time availability at LBNL, limited data were available at the same bias point to produce the histograms and extract the RPP thickness. However, the shape of the histograms in Fig. 77 would be similar when all terminals are grounded, although the actual collected charge and transient peak amplitudes would be different. Further, the differences between the histograms for the bulk and SOI devices, which is the focus of the present work, would also be consistent at a different bias. These assertions are confirmed with additional heavy ion data and laser measurements below.

To verify the reason for the difference in distributions, the transient peaks have been plotted as a function of collected charge in Fig. 78a, when the samples were exposed to Xe ions (LET $\approx$ 63.0 MeV-cm^2/mg) for the case when all device terminals were grounded during irradiation. The data for the bulk SiGe HBTs show three distinct groups, that were observed in data taken across LETs but become more apparent at the higher LETs. These groups have been verified with laser data to belong to three different ion strike regions (illustrated in Fig. 78c): 1) a group of low peaks and low collected charge that represents strikes outside of the deep trench (DT); 2) a group of medium peaks and large collected charge that represents strikes inside of the deep trench but outside of the intrinsic device (i.e., only involving the subcollector/substrate junction); and 3) a group of large peaks and large collected charge that represents strikes inside of the intrinsic device. These three regions have been

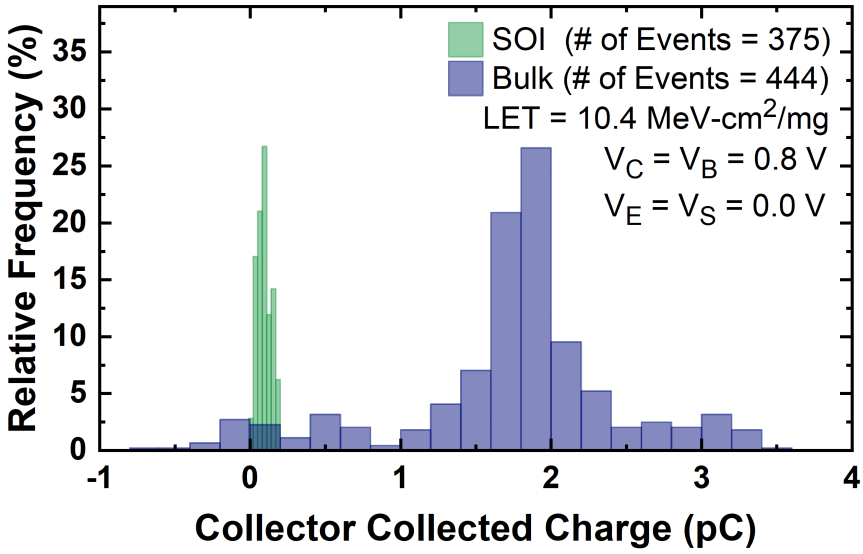

(a) Distribution of Measured Collected Charge

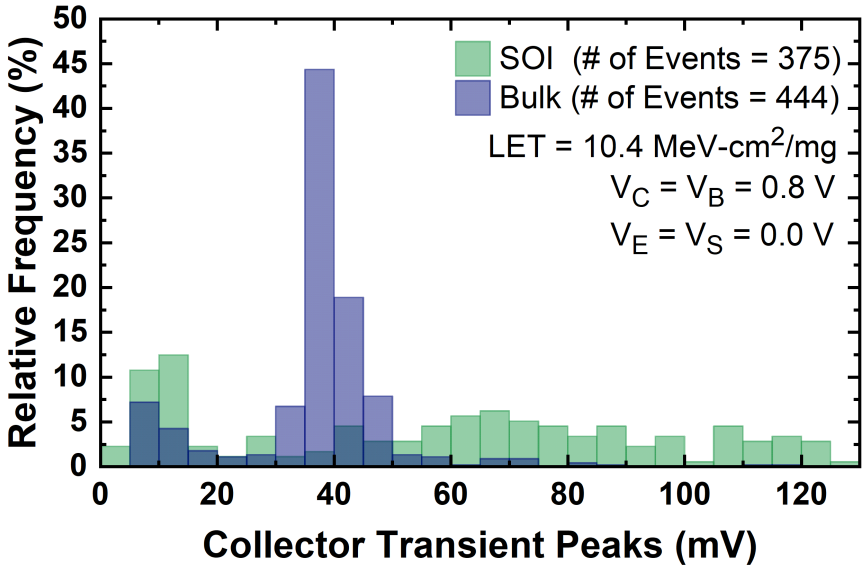

(b) Distribution of Measured Transient Peak Amplitude

Fig. 77: Relative frequency distribution of measured a) collected charge and b) transient peak amplitude on the collector terminal for bulk and SOI devices when the samples are exposed to an Ar ion beam.

previously identified for a different SiGe HBT bulk process [45], and a representative transient from each region is shown in Fig. 78b. The SOI data do not show these three groups, and in fact show a large variation in transient peaks with small variations in collected charge. Note that the maximum (worst-case) peaks for the SOI and bulk are similar. These results help to confirm that no charge collection takes place in the

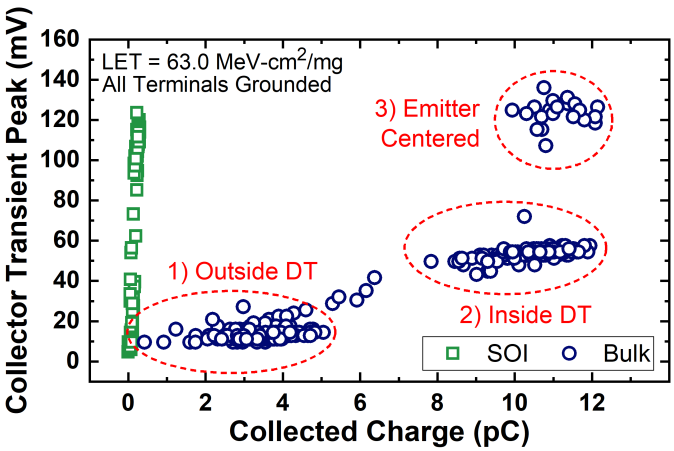

(a) Transient Peaks vs. Collected Charge

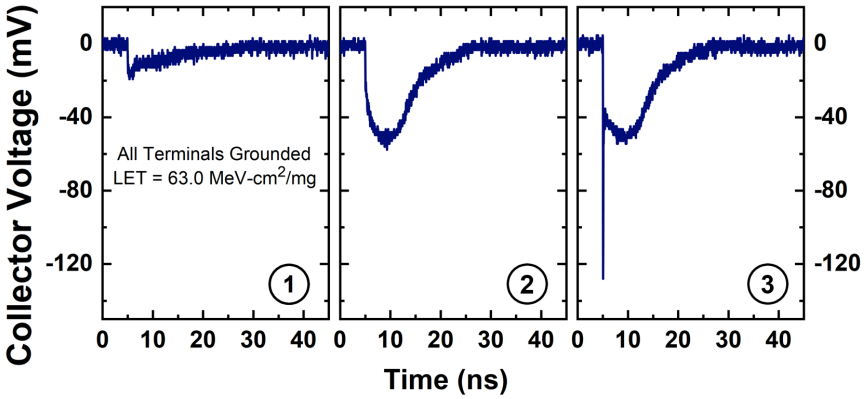

(b) Representative Transient From Each Data Group

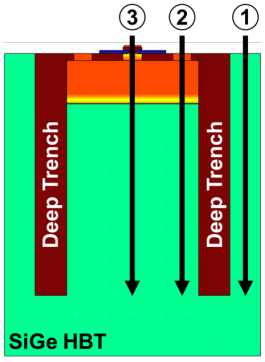

(c) Strike Locations for Each Data Grouping

Fig. 78: (a) Collector transient peaks as a function of collected charge when bulk and SOI samples are exposed to a Xe ion beam. There are three distinct regions for the bulk data that show events resulting from ion strikes in the intrinsic device, in the extrinsic device, and outside of the deep trench, which are shown in (b). This grouping of the data is not present for the SOI samples.

extrinsic device for the SOI samples.

4.4.4 Results from Pulsed Laser Data

To further understand the heavy-ion results, laser-induced transients were measured. For all the laser measurements shown, the beam was moved in the Z direction until the measured transient amplitude was maximized and all subsequent measurements were taken with the beam focused at this depth. To investigate the differences in the distribution of transient peaks shown in Fig. 77b, the laser was scanned across the device (in both X and Y directions) to obtain information about the spatial dependence of the SETs. Fig. 79 shows a 2-D map of the normalized transient peaks when the laser is scanned along the bulk and SOI devices. For these measurements the devices were biased with $V_C = V_B = 0.8\ V$ and $V_E = V_{Sub} = 0\ V$ and the laser pulse energies used for the bulk and SOI samples were approximately 60 pJ and 165 pJ, respectively. The emitter area for this device is $0.13 \times 5\ \mu m^2$. A smaller emitter area was chosen due to the symmetry of the device along the emitter length. The largest amplitude is observed in the center of the device, which has a CBEBC layout, and corresponds to the location of the emitter-base-collector stack of the intrinsic device, an expected result. As the laser is moved away from the center of the device, the data for the bulk device show a smaller, fairly constant, transient peak in the areas of the extrinsic device. These transients directly correspond to charge collection from the collector/substrate junction and form a "pedestal" in the data that is not present in the SOI results. Thus, the distribution of transients shown in Fig. 77b to be around 40 mV for the bulk device is a result of collector/substrate transients only. The large relative frequency of events around this amplitude results from the difference in area between the intrinsic and extrinsic device. Since the collector/substrate junction is absent in the SOI device and there is no charge collection in the extrinsic device, the distribution appears more uniform. The laser data confirms that no charge collection

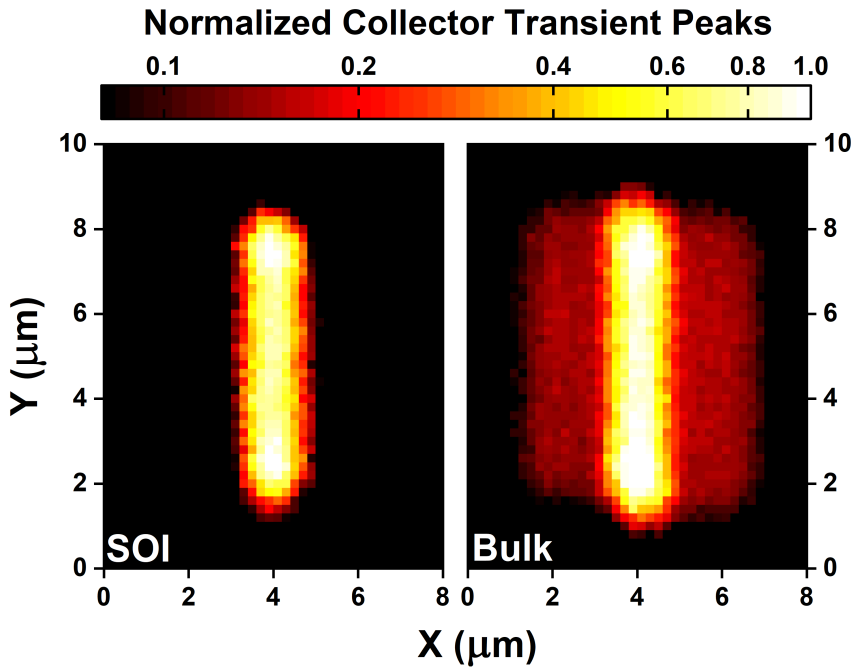

Fig. 79: Comparison of measured transient peaks for bulk and SOI devices as a function of position. The data has been normalized to the largest measured amplitude for each scan. The collector/substrate (CS) junction in the bulk SiGe HBTs results in an increase in transient peak outside the intrinsic device.

occurs outside of the intrinsic device for the SOI samples.

4.4.5 TCAD Simulations

To verify the heavy-ion results showing an RPP thickness smaller than the SOI thickness, 2-D TCAD simulations were performed. For these simulations, a representative model for a first-generation SiGe HBT was used. No attempt was made to calibrate the SET response between experiment and simulations, and the results obtained are only meant for qualitative observations. To reduce simulation time, a device with a CBE layout was simulated to reduce the number of mesh points. Although the experimental data shown in this section are for a device with a CBEBC layout, the trends observed for devices with both layout types should be similar. All terminals were grounded during the simulations to match the experimental conditions, unless stated otherwise. A Gaussian heavy-ion track was used with a constant LET as a

function of depth of 1 pC/μm. In the time domain, a Gaussian function was used to change the carrier generation rate, with a peak rate occurring at time t = 1 ns.

First, the subcollector thickness was swept from 0.25 μm to 3 μm in a bulk and SOI model while keeping the doping levels constant. For the SOI model, changing the subcollector thickness is equivalent to changing the SOI thickness, since for an optimized process, the vertical profile of the intrinsic device will not change. An ion strike traversing the center of the intrinsic device with an LET of 1 pC/μm was simulated. The results are shown in Fig. 80 and reveal two important findings. First, the collector peaks (shown at the top of Fig. 80) are very similar between bulk and SOI, which is consistent with the experimental data and the explanation above. Note that there are small changes in the transient peak as a function of the subcollector thickness, but they can be attributed to the changes in sheet resistance, and thus increases in collector series resistance (as shown by the inset). Second, the collected charge (shown at the bottom of Fig. 80) is shown to be relatively constant regardless of subcollector thickness (i.e., SOI thickness). These simulations confirm the observation from heavy-ion data that the RPP thickness for the SOI samples is smaller than the physical thickness of the SOI film.

Given the confirmed vast differences in the sensitive volume between SOI and bulk SiGe HBTs, the similarity between transient peak amplitudes for a given set of experimental conditions is unexpected. Thus, additional TCAD simulations were used to look at charge collection processes in the device. The results of these simulations are shown in Fig. 81, which shows the simulated electrostatic potential contours inside a SiGe HBT at t = 0 ns (i.e, before the strike) and t = 1 ns (i.e., during the ion strike). The potential contours are clearly disturbed by the excess carriers injected from the ion strike. However, for this particular structure and ion-strike conditions, there is a region of the subcollector where the potential remains undisturbed. In this case, the thick and heavily-doped subcollector layer acts as a barrier between

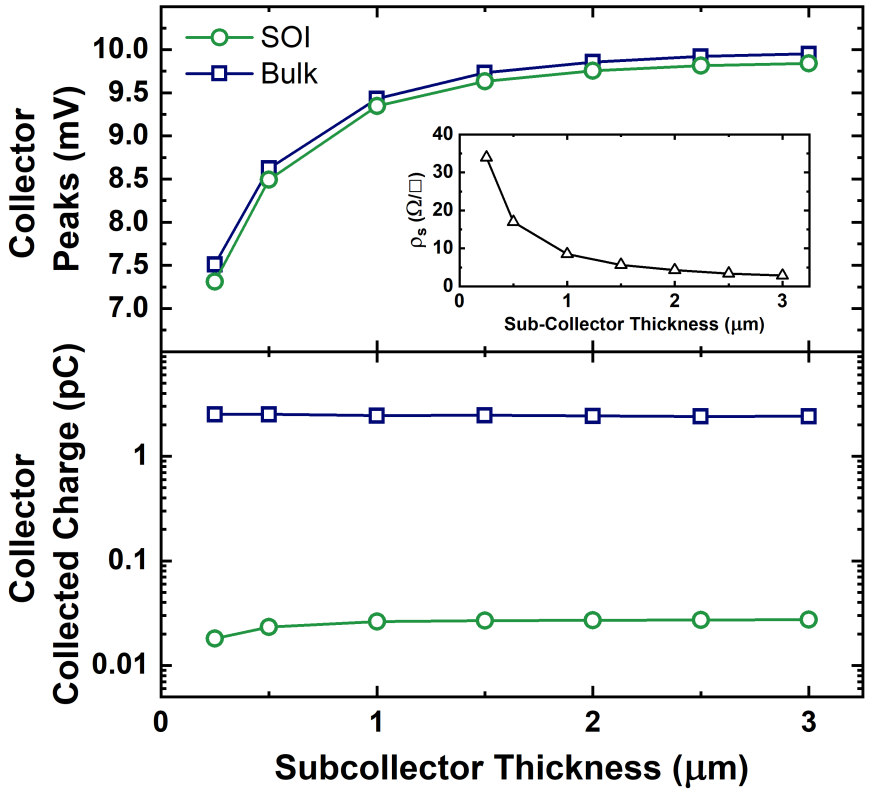

Fig. 80: Simulated transient peaks (top) and collected charge (bottom) for bulk and SOI SiGe HBTs for several subcollector thicknesses. The inset shows the difference in sheet resistance of the subcollector, which will change the series resistance of the collector terminal and affect the transient peak.

the intrinsic emitter/base/collector stack and the subcollector/substrate junction. These results suggest that, under certain conditions, the drift component that leads to the transient peak amplitude is independent of the subcollector/substrate diffusion component. This separation explains why the transient peaks in both bulk and SOI devices are similar.

One of the reasons that this potential remains undisturbed is due to the high doping levels in the thick subcollector. At low LETs, the ion-induced carrier densities may be comparable or below the doping level of the subcollector, in which case there will only be minor perturbations to the potential contours inside the subcollector. However, if the doping levels are low, the ion-induced carrier densities will be large enough to modify the potential contours in this region. When this occurs, the

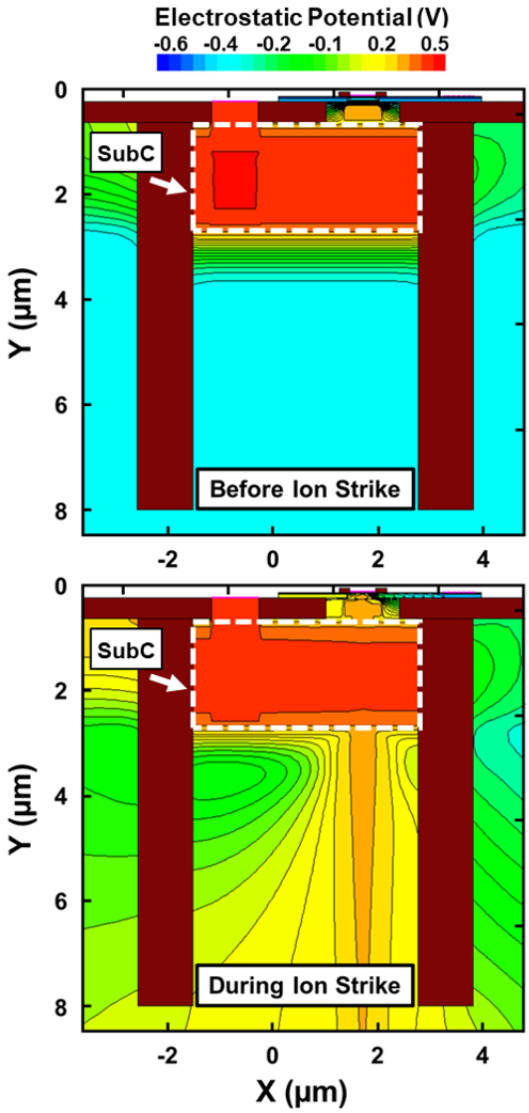

Fig. 81: Simulated electrostatic potential contours of a bulk SiGe HBT at t = 0 ns (top) and t = 1 ns (bottom) during an ion strike. The peak charge generation due to a heavy ion occurs at t = 1 ns. The potential in the subcollector region, shown enclosed by the dashed box and labeled "SubC", remains mostly undisturbed.

transients from the intrinsic and extrinsic device will no longer be decoupled, which would lead to differences between SOI and bulk transient amplitudes. These effects are shown in Fig. 82 where the percent difference between bulk and SOI transient amplitudes are shown as a function of LET for two different subcollector doping levels. The data show that for the lower doping level, there is a larger difference in SET amplitudes between bulk and SOI samples.

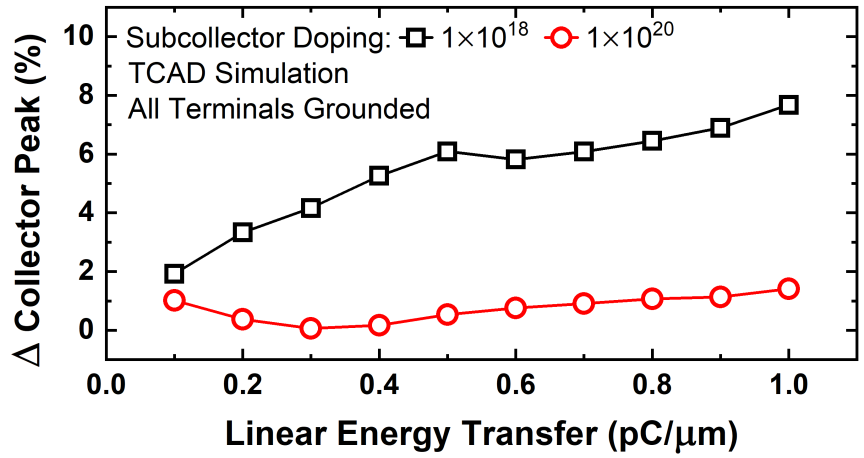

Fig. 82: Percent difference in transient peak versus LET for two different subcollector doping levels. Note that the difference between bulk and SOI is increased for a lower subcollector doping level.

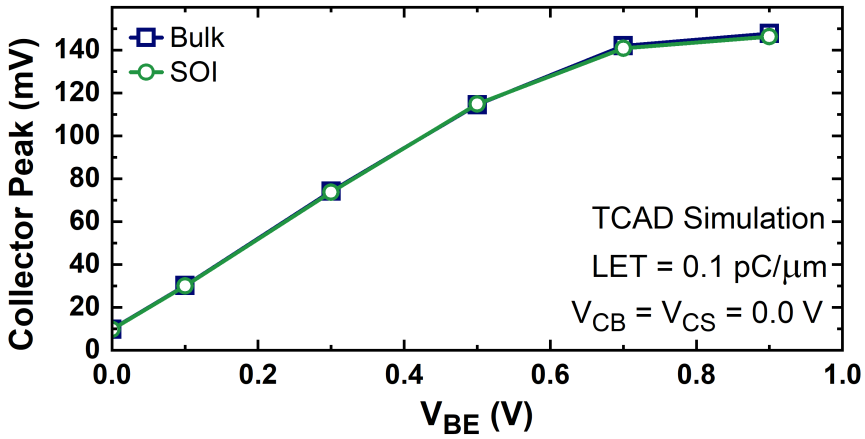

Fig. 83: Simulated transient peaks for bulk and SOI SiGe HBTs as a function of the applied base-emitter voltage.

Finally, TCAD simulations were used to verify that the transient peak amplitudes were similar for bulk and SOI across bias. For these simulations, the collector, base and substrate were biased to 0 V, and the emitter was biased with a negative voltage. The resulting transient peaks as a function of base-emitter voltage (V_{BE}) are shown in Fig. 83, where the two curves are overlapping. Since the only two points for heavy-ion data were for all terminals grounded and V_{BE} = 0.8 V, these simulations show that the similarity in amplitude between bulk and SOI samples does hold for the bias points in between.

4.4.6 Discussion

4.4.6.1 Laser Pulse Energy Loss Due to Reflections

The laser pulse energies shown thus far are the incident energies on the back of the die and have not been corrected in any way. As the laser pulse propagates through different materials, however, the change in refractive index at each interface will lead to energy loss due to Fresnel reflections. Using Fresnel's equations, the energy loss at the air/Si interface as the pulse propagates into the die can be calculated to be 31.2%. This loss will be the same for both the SOI and bulk samples.

For the SOI samples, before the pulse reaches the intrinsic device it encounters two additional interfaces as it propagates through the BOX ($Si/SiO_2/Si$). In this case, 68% of the pulse energy is transmitted through the BOX and incident on the intrinsic device, the rest is lost to reflections. This calculation does not account for the possibility of multiple reflections (i.e., the same wavefront being reflected multiple times between the two interfaces). When the space between multiple interfaces is small, the effects of multiple reflections can result in constructive or destructive interference that can either reduce or increase the amount of light transmitted through the medium.

To verify the effect of multiple reflections on the pulse energy loss, additional simulations were performed using FRED Optical Engineering Software [136]. FRED is a software program developed by Photon Engineering that uses raytracing to simulate the propagation of coherent or incoherent light through optomechanical systems. The focused laser pulse was simulated to observe the pulse energy transmitted through the BOX for different BOX thicknesses. The normalized transmission is shown as a function of BOX thickness in Fig. 84. The simulation results show that transmission through the BOX can vary between 100% and 50% for BOX thickness variations of 200 nm. Thus, accurate knowledge of the BOX thickness is necessary for accurate estimation of the pulse energy at the intrinsic device. For the Jazz H3 process in the

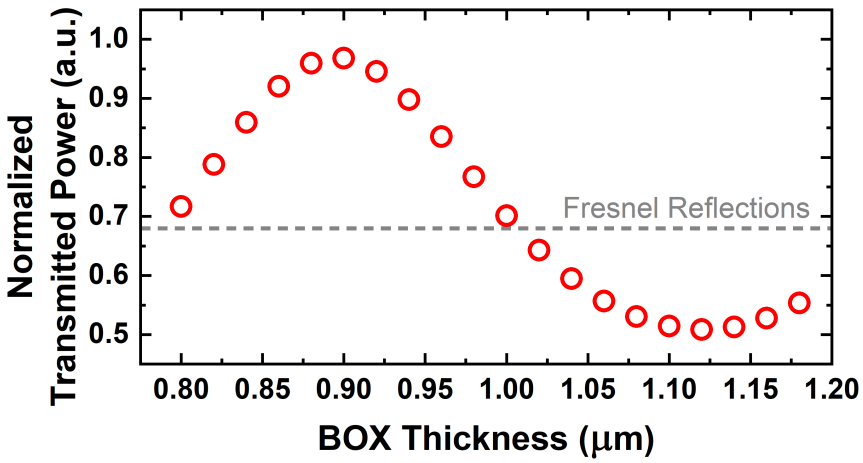

Fig. 84: Simulated laser power transmitted through the BOX as a function of BOX thickness. The dashed line indicates transmission after accounting for Fresnel reflections.

present work, the BOX thickness is around 1 μm, and the transmitted pulse energy is very close to the value obtained by using Fresnel's equations.

The main takeaway of these simulation results is that pulse energy losses due to reflections must be taken into account when comparing laser-induced transients for bulk and SOI devices. This consideration becomes important when calculating the amount of deposited charge by pulsed lasers.

4.4.6.2 Implications for Radiation Hardness Assurance

Throughout the years, many SET mitigation techniques for circuits built using SiGe HBTs have been proposed. These techniques include the use of devices operating in inverse mode (i.e., electrically swapping physical emitter and collector in the circuit) [88, 137], using *pnp* SiGe HBTs when available [34, 119–121], using different layout configurations and isolation wells in the substrate [70, 138–141], and using different circuit topologies [36, 37, 142–145]. In addition to the results in this section, several previous studies have shown that using SiGe HBTs on SOI can significantly reduce charge collection [35, 70, 71, 131]. One study showed using heavy-ion data from SiGe HBT shift registers that the single-event upset cross-section for SiGe HBTs

on SOI was lower than for similar devices built on bulk substrates. This reduction in cross-section resulted in a predicted 88% reduction of upsets per bit per day simulated using CREME96 [35]. Although SOI is considered a radiation-hardening-by-process technique, there are several advantages to using SOI devices over other radiation-hardening-by-design techniques.

First, the use of inverse-mode devices can result in circuits with lower performance [137] and process changes that improve the performance of devices operating in inverse mode can lead to a worsening of their SET response [146]. Further, *pnp* SiGe HBTs are not widely available due to the difficulties with fabricating high-performance *pnp* devices [147], making it difficult to adopt these devices in commercial designs. Finally, substrate engineering concepts will not typically affect device performance and some can be implemented without additional photomasks. However, some of these mitigation approaches can require larger designs to accommodate the additional wells [141], which can increase the cost of these approaches. In the case of a commercial process such as TowerJazz's SBC18H3, the bulk and SOI devices are almost identical in performance, with the SOI devices having lower parasitic capacitances [132]. In addition, existing circuit designs using SiGe HBTs can be easily migrated from a bulk substrate to an SOI substrate without making any significant changes since both processes would use identical photomasks. One drawback, however, of using SiGe HBTs on SOI is increased self-heating compared to bulk devices [148].

4.4.6.3 Implications for Ion/Laser Correlation

A previous study showed that in order to correlate ion and laser results in a SiGe HBT using a Gaussian laser beam, the focused spot size had to be increased [5]. In that study, increasing the spot size was necessary to elongate the charge deposition profile resulting from the laser beam so that the charge deposited deep in the substrate could

contribute to the diffusion component that results in the long transient "tail". For an SOI sample, however, this slow diffusion component does not exist. Therefore, it should be substantially easier to reproduce the waveforms obtained from heavy ions using a pulsed laser. Fig. 85 shows a comparison between laser- and ion-induced transients in bulk and SOI SiGe HBTs, where the laser pulse energy was adjusted to match the transient peak amplitude between the laser and ion data when all terminals of the device are grounded. The chosen pulse energy for the bulk and SOI SiGe HBTs that match the amplitude of the heavy-ion data were 131 pJ and 449 pJ, respectively. Note that, for a small spot size (≈ 1 μm), the charge deposition profile will also be short in the axial direction and charge will not be deposited deep in the substrate. Without the charge in the substrate to slowly diffuse to the collector terminal, the laser data in Fig. 85 show an absence of a tail for the bulk devices when the transient peak amplitudes are matched, resulting in a mismatch of the collected charge. However, the ion and laser transients for the SOI samples are almost identical after adjusting the laser pulse energy to match the transient peak. In this case, the slight differences could be attributed to the differences in bandwidth from the oscilloscopes used at each facility.

The differences shown between the ion- and laser-induced transients for the bulk SiGe HBTs illustrate the difficulties in correlating ion and laser data. These difficulties are exacerbated when considering transients induced from backside two-photon absorption excitation. The results presented, however, suggest that it is much easier to correlate ion and laser data for SiGe HBTs on SOI than on bulk substrates. The removal of the diffusion component by adding the BOX, alleviates the requirements of the charge deposition profile. That is, for an SOI SiGe HBT, a shorter charge deposition profile in the axial direction can still be used to achieve good correlation. This result is advantageous from the perspective of an experimenter, since they would not have to sacrifice lateral resolution to achieve good correlation.

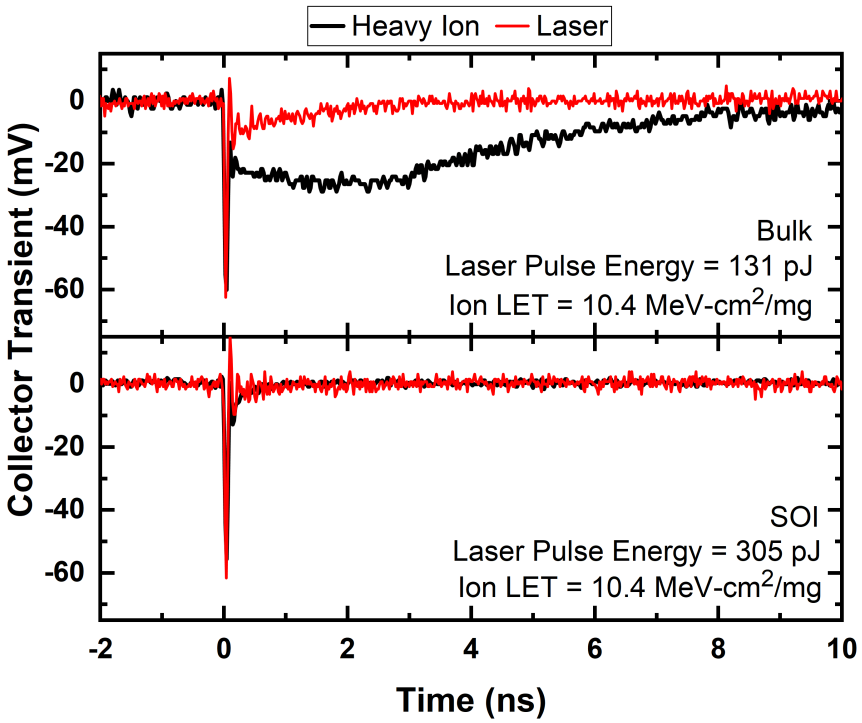

Fig. 85: Comparison between laser- and ion-induced transients in bulk (top) and SOI (bottom) SiGe HBTs when the samples are exposed to an Ar ion and all terminals of the device are grounded. Note that there are significant differences between the ion and laser transients for the bulk device, but the transients for the SOI device are almost identical.

Finally, recent studies have shown that the direction of light polarization can affect the SET response of highly-scaled FinFET devices due to plasmonic enhancement effects [149, 150]. This effect could further complicate the efforts to correlate ion and laser measurements. Thus far, there is no evidence to support that there is a polarization dependence for the laser-based response of SiGe HBTs used in the present study. Although further experimentation and simulation are required to verify whether plasmonic enhancements are being masked by other geometric factors (as is the case in [149]), it is unlikely that such effects exists for two main reasons. First, plasmonic enhancement requires specific nanostructures (e.g., metal-dielectric-metal) with small dimensions (e.g., dielectric thickness ≈10 nm). These structures are not readily available in a 130-nm process like the one used in the present study. Second, FinFETs are a lateral-transport device, so the electric field can be oriented either

parallel or perpendicular to carrier transport, which may affect the measured SETs. However, SiGe HBTs are a vertical-transport device and in this case the electric field will always be oriented perpendicular to carrier transport. Thus, it is not expected to affect SET measurements. For reference, in the present work, the light was polarized such that the electric field is across the CBEBC contacts (i.e., along the horizontal direction in Fig. 73).

4.5 Summary

This chapter has demonstrated three mitigation techniques for RF circuits and systems using experimental data from ion and laser sources as well as TCAD and circuit-level simulations.

The first used an RF power detector to sense the occurrence of SETs in RF circuits and systems. It was shown through TPA experiments that the proposed circuit can be used to detect SETs in the LNA. Furthermore, the output of the detector was shown to yield information about the RF power of the SET, and also detect the relative level of SETs with respect to the input signal. An expression for the detector output voltage as a function of the LNA SET power was derived and resulted in an excellent fit to experimental data. The circuit design trade-offs were explored using experiments and TCAD simulations, with the main trade-off being between transient responsivity and suppression of the fundamental tone. A solution to distinguish SETs on the RF system of interest and the detector itself that uses a pseudo-TMR approach was demonstrated using mixed-mode TCAD simulations.

The second technique showed that transient response of LNAs designed with *pnp* devices exhibit lower transient peaks and collected charge when compared to an LNA designed with *npn* devices. However, by using the same design procedure, the *pnp* LNA has lower performance than the *npn* LNA. Further, when modulated data is present in an RF communications system, the *npn* LNA will be more susceptible

to data corruption than the *pnp* LNA. The impact of the tradeoff between circuit performance and SET robustness will be application-specific and it is difficult to choose one over the other without making assumptions about the desired application. However, the performance of the *pnp* circuit could be improved using circuit design techniques, which could potentially be enough for a given application. An alternative version of the *pnp* LNA was designed to match the gain of the *npn* LNA. In this case, the *pnp* LNA was still more robust to SETs than the *npn* LNA. Therefore, *pnp* devices should not be ruled out as a mitigation strategy for RF circuits.

Finally, a comparison of heavy-ion induced SETs in commercially-available SiGe HBTs fabricated on both bulk and SOI substrates was shown. The devices fabricated on SOI showed a significant decrease in sensitive volume compared to similar bulk devices. The results showed that the subcollector layer acts as an effective barrier between drift and diffusion processes in an SET. This barrier enables the worst-case transient peaks of bulk and SOI SiGe HBTs to be almost identical, while the buried oxide significantly limits the charge collected by SOI devices. The comparisons shown in the this chapter, should better equip circuit and system designers to take advantage of the commercially-available SiGe-on-SOI platforms to develop electronics that are more tolerant to SETs.

CHAPTER V

CONCLUSION

The present work has presented a series of investigations with new developments for approaches to test, assess, and mitigate the risks of single-event transients in RF communications systems.

In terms of testing approaches, two novel techniques were presented that utilize pulsed lasers to emulate the SETs that result from heavy-ion measurements. Both techniques modified the charge deposition profile generated via two-photon absorption to allow for quantitative correlation between laser pulse energy and heavy-ion LET. Additional work must be completed to fully validate the results obtained from the quasi-Bessel beams in SiGe HBTs.

A new approach for assessing the effects of SETs in RF receivers carrying modulated data was presented. By using IQ diagrams and localized radiation sources like pulsed-lasers, engineers can identify vulnerabilities and deploy targeted mitigation techniques. Further, understanding the changes in amplitude and phase that result from an SET generated in a particular component, can aid in the development of new topologies for SET mitigation.

Finally, three different approaches to mitigate SETs that can be applied to RF communications systems were also presented. The first technique demonstrated the use of RF power detectors as a way to sense SETs in RF systems. The second technique explored the use of *pnp* SiGe HBTs in low-noise amplifiers and the tradeoff between performance and SET robustness of using these types of devices. The third technique included the use of SOI substrates to limit charge collection on the electrical terminals of the device. This last study also showed that correlating ion and laser

data from devices on SOI is much simpler than bulk devices due to the removal of the substrate diffusion components.

Although the investigations in the present work are all based on device test structures and circuits that utilize SiGe HBTs, the testing and assessment techniques can be applied to additional platforms. Further, RF power detectors as a way of SET sensing and the use of SOI devices can also be applied as mitigation techniques in other platforms. Thus the present work has potential to generate and advance research on SEE testing, assessment and mitigation across many semiconductor platforms.

A summary of the contributions of the present work follows.

1. A new approach to quantitatively correlate single-event transients produced by two-photon absorption and heavy ions in SiGe HBTs.

2. The first investigation on the use of quasi-Bessel beams to generate laser-induced transients in SiGe HBTs via two-photon absorption.

3. A new characterization technique for single-event transients in RF communications systems that uses I-Q diagrams.

4. Demonstrated the use of an RF power detector to sense single-event transients in RF circuits.

5. An investigation of the single-event transient response of commercial SiGe HBTs on bulk and silicon-on-insulator substrates.

6. An assessment of the tradeoffs between RF performance and single-event transient robustness of low-noise amplifiers designed using only *npn* and only *pnp* SiGe HBTs in a complementary SiGe BiCMOS platform.

CHAPTER VI

FUTURE WORK

The work completed as part of this dissertation has generated a series of additional questions that are relevant to continue advancing the study of single-event effects in devices, circuits and systems.

1. **Dependence of Laser/Ion Correlation on Emitter Area**

   Some of the results shown in Chapter 2, showed that the transient amplitude depended on the emitter geometry, while the collected charge depended on the subcollector/substrate geometry. Given these results, it is pertinent to explore experimentally how the correlation achieved between ion and laser data depends on the emitter area of the SiGe HBTs. Such an experiment might lead to a generalized set of expressions or conditions that would facilitate correlation of SETs generated by ions and lasers in SiGe HBTs.

2. **Correlation of SETs Generated by Ion and Laser at the Circuit Level**

   The results presented in this dissertation showed that it is possible to achieve excellent agreement between SETs generated by heavy ion and laser sources in SiGe HBTs. All of the results shown were at the transistor level. The next step is to verify experimentally whether correlating SETs at the device level is sufficient to ensure that the response of circuits and systems will be the same between ion and lasers. This verification would enable researchers to focus on device-level correlation and directly extend those results to larger circuits and systems.

3. **Correlation of SETs in Other Device Types and Platforms**

One of the reasons that correlation of SETs generated by heavy ions and lasers was possible is that the mechanism for collected charge and transient peak amplitude are mostly decoupled from each other in SiGe HBTs. This property may not be present in other types of semiconductor devices. Thus, the approaches shown in Chapter 2 should be applied to other types of devices such as CMOS, HEMTs and HBTs in other material systems.

4. **Experimental Verification of Characterization Methodology for RF Circuits and Systems**

   The methodology proposed in Chapter 3 allows for the comparison of multiple RF systems carrying modulated data in terms of their robustness to SETs. This assessment tool can be used to finalize the selection of RF components in space systems. Due to the complexities associated with implementing a full RF transceiver to verify this methodology experimentally, only simulations were included in this dissertation. This characterization methodology should be verified experimentally, and efforts are currently underway to achieve this.

5. **Application of IQ Diagrams for Total Ionizing Dose Studies**

   Although the IQ diagrams were used in Chapter 3 for SETs, the same diagrams could also be used to compare degradation of communications systems after they have been exposed to total ionizing dose. If the results of such an experiment reveal that the degradation is predictable with dose, a dose-dependent equalizer could be implemented to reduce the bit errors that would result from this performance degradation.

REFERENCES

[1] "July 12, 1962: The Day Information Went Global." [Online]. Available: https://www.nasa.gov/topics/technology/features/telstar.html

[2] R. A. Reed, J. Kinnison, J. C. Pickel, S. Buchner, P. W. Marshall, S. Kniffin, and K. A. LaBel, "Single-event effects ground testing and on-orbit rate prediction methods: the past, present, and future," *IEEE Transactions on Nuclear Science*, vol. 50, no. 3, pp. 622–634, Jun. 2003.

[3] A. Ildefonso, I. Song, Z. E. Fleetwood, N. E. Lourenco, M. T. Wachter, G. N. Tzintzarov, and J. D. Cressler, "Modeling Single-Event Transient Propagation in a SiGe BiCMOS Direct-Conversion Receiver," in *Radiat. Eff. Components Syst. Conf.*, 2016.

[4] A. Kar-Roy, D. Howard, E. J. Preisler, and M. Racanelli, "Recent developments using TowerJazz SiGe BiCMOS platform for mmWave and THz applications," in *Passiv. Act. Millimeter-Wave Imaging XVI, Proc. Int. Soc. Opt. Photonics*, vol. 8715, 2013, p. 871505.

[5] A. Ildefonso, Z. E. Fleetwood, G. N. Tzintzarov, J. M. Hales, D. Nergui, M. Frounchi, A. Khachatrian, S. P. Buchner, D. McMorrow, J. H. Warner, J. Harms, A. Erickson, K. Voss, V. Ferlet-Cavrois, and J. D. Cressler, "Optimizing Optical Parameters to Facilitate Correlation of Laser-and Heavy-Ion-Induced Single-Event Transients in SiGe HBTs," *IEEE Trans. Nucl. Sci.*, vol. 66, no. 1, pp. 359–367, Jan. 2019.

[6] A. Ildefonso, I. Song, G. N. Tzintzarov, Z. E. Fleetwood, N. E. Lourenco, M. T. Wachter, and J. D. Cressler, "Modeling Single-Event Transient Propagation in a SiGe BiCMOS Direct-Conversion Receiver," *IEEE Trans. Nucl. Sci.*, vol. 64, no. 8, pp. 2079–2088, 2017.

[7] A. Ildefonso, C. T. Coen, Z. E. Fleetwood, G. N. Tzintzarov, M. T. Wachter, A. Khachatrian, D. McMorrow, J. H. Warner, P. Paki, and J. D. Cressler, "Utilizing SiGe HBT Power Detectors for Sensing Single-Event Transients in RF Circuits," *IEEE Trans. Nucl. Sci.*, vol. 65, no. 1, pp. 239–248, 2018.

[8] A. Ildefonso, J. H. Warner, J. D. Cressler, G. N. Tzintzarov, D. Nergui, A. P. Omprakash, P. S. Goley, J. M. Hales, A. Khachatrian, S. P. Buchner, and D. McMorrow, "Comparison of Single-Event Transients in SiGe HBTs on Bulk and Thick-Film SOI," *IEEE Trans. Nucl. Sci.*, vol. 67, no. 1, pp. 71–80, 2020.

[9] A. Ildefonso, G. N. Tzintzarov, N. E. Lourenco, Z. E. Fleetwood, A. Khachatrian, S. P. Buchner, D. McMorrow, J. H. Warner, M. Kaynak, and J. D.

Cressler, "Tradeoffs Between RF Performance and SET Robustness in Low-Noise Amplifiers in a Complementary SiGe BiCMOS Platform," *IEEE Trans. Nucl. Sci.*, 2020. Accepted (Early Access)., doi: 10.1109/TNS.2020.2996298.

[10] "News Conference 39, July 23, 1962." [Online]. Available: https://www.jfklibrary.org/archives/other-resources/john-f-kennedy-press-conferences/news-conference-39

[11] "That's no moon. (It's also not the Death Star.)." [Online]. Available: https://airandspace.si.edu/stories/editorial/telstar-not-death-star

[12] J. S. Mayo, H. Mann, F. J. Witt, D. S. Peck, H. K. Gummel, and W. L. Brown, "The command system malfunction of the Telstar satellite," *The Bell System Technical Journal*, vol. 42, no. 4, pp. 1631–1657, 1963.

[13] D. Peck and E. Schmid, "Effects of radiation on transistors in the first Telstar satellite," *Nature*, vol. 199, 1963.

[14] D. Harland and R. Lorenz, *Space Systems Failures: Disasters and Rescues of Satellites, Rocket and Space Probes*, ser. Springer Praxis Books. Praxis, 2005.

[15] J. Scarpulla and A. Yarbrough, "What Could Go Wrong? The Effects of Ionizing Radiation on Space Electronics," *Crosslink*, pp. 15–19, 2003.

[16] M. Xapsos, "A Brief History of Space Climatology: From the Big Bang to the Present," *IEEE Trans. Nucl. Sci.*, vol. 66, no. 1, pp. 17–37, 2019.

[17] T. R. Oldham, "Basic Mechanisms of TID and DDD Response in MOS and Bipolar Microelectronics," in *IEEE NSREC Short Course*, 2011.

[18] D. M. Fleetwood, "Fast and slow border traps in MOS devices," *IEEE Trans. Nucl. Sci.*, vol. 43, no. 3, pp. 779–786, Jun. 1996.

[19] D. M. Fleetwood, P. S. Winokur, R. A. Reber, T. L. Meisenheimer, J. R. Schwank, M. R. Shaneyfelt, and L. C. Riewe, "Effects of oxide traps, interface traps, and "border traps" on metal-oxide-semiconductor devices," *Journal of Applied Physics*, vol. 73, no. 10, pp. 5058–5074, 1993.

[20] J. R. Schwank, M. R. Shaneyfelt, D. M. Fleetwood, J. A. Felix, P. E. Dodd, P. Paillet, and V. Ferlet-Cavrois, "Radiation Effects in MOS Oxides," *IEEE Trans. Nucl. Sci.*, vol. 55, no. 4, pp. 1833–1853, Aug. 2008.

[21] J. R. Srour, C. J. Marshall, and P. W. Marshall, "Review of displacement damage effects in silicon devices," *IEEE Trans. Nucl. Sci.*, vol. 50, no. 3, pp. 653–670, Jun. 2003.

[22] S. Buchner and D. McMorrow, "Single Event Transients in Linear Integrated Circuits," in *IEEE NSREC Short Course*, Jun. 2005.

[23] F. W. Sexton, "Destructive single-event effects in semiconductor devices and ICs," *IEEE Trans. Nucl. Sci.*, vol. 50, no. 3, pp. 603–621, Jun. 2003.

[24] H. Ying, B. R. Wier, J. Dark, N. E. Lourenco, L. Ge, A. P. Omprakash, M. Mourigal, D. Davidovic, and J. D. Cressler, "Operation of SiGe HBTs down to 70 mK," *IEEE Electron Device Lett.*, vol. 38, no. 1, pp. 12–15, Jan. 2017.

[25] A. P. Omprakash, H. Dao, U. S. Raghunathan, H. Ying, P. S. Chakraborty, J. A. Babcock, R. Mukhopadhyay, and J. D. Cressler, "An Investigation of High-Temperature (to 300 C) Safe-Operating-Area in a High-Voltage Complementary SiGe on SOI Technology," *IEEE Trans. Electron Devices*, vol. 64, no. 9, pp. 3748–3755, Sep. 2017.

[26] J. D. Cressler, "Silicon-germanium as an enabling technology for extreme environment electronics," *IEEE Trans. Device Mater. Rel.*, vol. 10, no. 4, pp. 437–448, Dec. 2010.

[27] ——, "Radiation effects in SiGe technology," *IEEE Trans. Nucl. Sci.*, vol. 60, no. 3, pp. 1992–2014, Jun. 2013.

[28] J. Cressler and G. Niu, *Silicon-germanium Heterojunction Bipolar Transistors*. Artech House, 2003.

[29] N. E. Lourenco, R. L. Schmid, K. A. Moen, S. D. Phillips, T. D. England, J. D. Cressler, J. Pekarik, J. Adkisson, R. Camillo-Castillo, P. Cheng, J. E. Monaghan, P. Gray, D. Harame, M. Khater, Q. Liu, A. Vallett, B. Zetterlund, V. Jain, and V. Kaushal, "Total Dose and Transient Response of SiGe HBTs from a New 4th-Generation, 90 nm SiGe BiCMOS Technology," in *2012 IEEE Radiation Effects Data Workshop*, Jul. 2012, pp. 1–5.

[30] J. A. Babcock, J. D. Cressler, L. S. Vempati, S. D. Clark, R. C. Jaeger, and D. L. Harame, "Ionizing radiation tolerance of high-performance SiGe HBTs grown by UHV/CVD," *IEEE Trans. Nucl. Sci.*, vol. 42, no. 6, pp. 1558–1566, Dec. 1995.

[31] S. Diez, M. Lozano, G. Pellegrini, F. Campabadal, I. Diez, D. Knoll, B. Heinemann, and M. Ullan, "Proton Radiation Damage on SiGe:C HBTs and Additivity of Ionization and Displacement Effects," *IEEE Trans. Nucl. Sci.*, vol. 56, no. 4, pp. 1931–1936, Aug. 2009.

[32] J. M. Roldan, W. E. Ansley, J. D. Cressler, S. D. Clark, and D. Nguyen-Ngoc, "Neutron radiation tolerance of advanced UHV/CVD SiGe HBT BiCMOS technology," *IEEE Trans. Nucl. Sci.*, vol. 44, no. 6, pp. 1965–1973, Dec. 1997.

[33] N. E. Lourenco, Z. E. Fleetwood, A. Ildefonso, M. T. Wachter, N. J. H. Roche, A. Khachatrian, D. McMorrow, S. P. Buchner, J. H. Warner, H. Itsuji, D. Kobayashi, K. Hirose, P. Paki, A. Raman, and J. D. Cressler, "The Impact of Technology Scaling on the Single-Event Transient Response of SiGe HBTs," *IEEE Trans. Nucl. Sci.*, vol. 64, no. 1, pp. 406–414, Jan. 2017.

[34] N. E. Lourenco, Z. E. Fleetwood, S. Jung, A. S. Cardoso, P. S. Chakraborty, T. D. England, N. J. Roche, A. Khachatrian, D. McMorrow, S. P. Buchner, J. S. Melinger, J. H. Warner, P. Paki, M. Kaynak, B. Tillack, D. Knoll, and J. D. Cressler, "On the transient response of a complementary (npn + pnp) SiGe HBT BiCMOS Technology," *IEEE Trans. Nucl. Sci.*, vol. 61, no. 6, pp. 3146–3153, Dec. 2014.

[35] E. P. Wilcox, S. D. Phillips, P. Cheng, T. Thrivikraman, A. Madan, J. D. Cressler, G. Vizkelethy, P. W. Marshall, C. Marshall, J. A. Babcock, K. Kruckmeyer, R. Eddy, G. Cestra, and B. Zhang, "Single Event Transient Hardness of a New Complementary (npn + pnp) SiGe HBT Technology on Thick-Film SOI," *IEEE Trans. Nucl. Sci.*, vol. 57, no. 6, pp. 3293–3297, Dec. 2010.

[36] R. Krithivasan, P. W. Marshall, M. Nayeem, A. K. Sutton, W. M. Kuo, B. M. Haugerud, L. Najafizadeh, J. D. Cressler, M. A. Carts, C. J. Marshall, D. L. Hansen, K. C. M. Jobe, A. L. McKay, G. Niu, R. Reed, B. A. Randall, C. A. Burfield, M. D. Lindberg, B. K. Gilbert, and E. S. Daniel, "Application of RHBD techniques to SEU hardening of third-generation SiGe HBT logic circuits," *IEEE Trans. Nucl. Sci.*, vol. 53, no. 6, pp. 3400–3407, Dec. 2006.

[37] S. Jung, I. Song, Z. E. Fleetwood, U. Raghunathan, N. E. Lourenco, M. A. Oakley, B. R. Wier, N.-H. Roche, A. Khachatrian, D. McMorrow, S. P. Buchner, J. H. Warner, P. Paki, and J. D. Cressler, "The Role of Negative Feedback Effects on Single-Event Transients in SiGe HBT Analog Circuits," *IEEE Trans. Nucl. Sci.*, vol. 62, no. 6, pp. 2599–2605, Dec. 2015.

[38] N. E. N. Lourenco, S. Zeinolabedinzadeh, A. Ildefonso, Z. Z. E. Fleetwood, C. C. T. Coen, I. Song, S. Jung, F. Inanlou, N. J. Roche, A. Khachatrian, D. McMorrow, S. P. S. Buchner, J. H. J. Warner, P. Paki, and J. D. J. Cressler, "An Investigation of Single-Event Effect Modeling Techniques for a SiGe RF Low-Noise Amplifier," *IEEE Trans. Nucl. Sci.*, vol. 63, no. 1, pp. 273–280, 2016.

[39] S. Zeinolabedinzadeh, I. Song, U. S. Raghunathan, N. E. Lourenco, Z. E. Fleetwood, M. A. Oakley, A. S. Cardoso, N. J. Roche, A. Khachatrian, D. McMorrow, S. P. Buchner, J. H. Warner, P. Paki-Amouzou, and J. D. Cressler, "Single-Event Effects in a W-Band (75-110 GHz) Radar Down-Conversion Mixer Implemented in 90 nm, 300 GHz SiGe HBT Technology," *IEEE Trans. Nucl. Sci.*, vol. 62, no. 6, pp. 2657–2665, Dec. 2015.

[40] I. Song, U. S. Raghunathan, N. E. Lourenco, Z. E. Fleetwood, M. A. Oakley, S. Jung, M. K. Cho, N. J. Roche, A. Khachatrian, J. H. Warner, S. P. Buchner, D. McMorrow, P. Paki, and J. D. Cressler, "An Investigation of the Use of Inverse-Mode SiGe HBTs as Switching Pairs for SET-Mitigated RF Mixers," *IEEE Trans. Nucl. Sci.*, vol. 63, no. 2, pp. 1099–1108, Apr. 2016.

[41] I. Song, S. Jung, N. E. Lourenco, U. S. Raghunathan, Z. E. Fleetwood, S. Zeinolabedinzadeh, T. B. Gebremariam, F. Inanlou, N. J. Roche, A. Khachatrian,

D. McMorrow, S. P. Buchner, J. S. Melinger, J. H. Warner, P. Paki-Amouzou, and J. D. Cressler, "Design of radiation-hardened RF low-noise amplifiers using inverse-mode SiGe HBTs," *IEEE Trans. Nucl. Sci.*, vol. 61, no. 6, pp. 3218–3225, Dec. 2014.

[42] S. D. Phillips, K. A. Moen, N. E. Lourenco, and J. D. Cressler, "Single-Event Response of the SiGe HBT Operating in Inverse-Mode," *IEEE Trans. Nucl. Sci.*, vol. 59, no. 6, pp. 2682–2690, Dec. 2012.

[43] I. Song, S. Jung, N. E. Lourenco, U. S. Raghunathan, Z. E. Fleetwood, M. K. Cho, N. J. Roche, A. Khachatrian, J. H. Warner, S. P. Buchner, D. McMorrow, P. Paki, and J. D. Cressler, "Optimization of SiGe HBT RF Switches for Single-Event Transient Mitigation," *IEEE Trans. Nucl. Sci.*, vol. 62, no. 6, pp. 3057–3063, Dec. 2015.

[44] S. Zeinolabedinzadeh, H. Ying, Z. E. Fleetwood, N. J. Roche, A. Khachatrian, D. McMorrow, S. P. Buchner, J. H. Warner, P. Paki-Amouzou, and J. D. Cressler, "Single-Event Effects in High-Frequency Linear Amplifiers: Experiment and Analysis," *IEEE Trans. Nucl. Sci.*, vol. 64, no. 1, pp. 125–132, Jan. 2017.

[45] Z. E. Fleetwood, N. E. Lourenco, A. Ildefonso, J. H. Warner, M. T. Wachter, J. M. Hales, G. N. Tzintzarov, N. J. Roche, A. Khachatrian, S. P. Buchner, D. McMorrow, P. Paki, and J. D. Cressler, "Using TCAD Modeling to Compare Heavy-Ion and Laser-Induced Single Event Transients in SiGe HBTs," *IEEE Trans. Nucl. Sci.*, vol. 64, no. 1, pp. 398–405, 2017.

[46] S. P. Buchner, F. Miller, V. Pouget, and D. P. McMorrow, "Pulsed-laser testing for single-event effects investigations," *IEEE Trans. Nucl. Sci.*, vol. 60, no. 3, pp. 1852–1875, Jun. 2013.

[47] C. Weulersse, F. Bezerra, F. Miller, T. Carrière, N. Buard, and W. Falo, "Probing SET sensitive volumes in linear devices using focused laser beam at different wavelengths," *IEEE Trans. Nucl. Sci.*, vol. 55, no. 4, pp. 2007–2012, Aug. 2008.

[48] A. M. Chugg, R. Jones, M. Moutrie, C. S. Dyer, C. Sanderson, and A. Wraight, "Probing the charge-collection sensitivity profile using a picosecond pulsed laser at a range of wavelengths," *IEEE Trans. Nucl. Sci.*, vol. 49 I, no. 6, pp. 2969–2976, Dec. 2002.

[49] A. M. Chugg, A. J. Burnell, M. J. Moutrie, R. Jones, and R. Harboe-Sørensen, "Laser SEE sensitivity mapping of SRAM cells," *IEEE Trans. Nucl. Sci.*, vol. 54, no. 6, pp. 2106–2112, Dec. 2007.

[50] V. Pouget, D. Lewis, H. Lapuyade, R. Briand, P. Fouillat, L. Sarger, and M. C. Calvet, "Validation of radiation hardened designs by pulsed laser testing and SPICE analysis," *Microelectron. Reliab.*, vol. 39, no. 6-7, pp. 931–935, Jun. 1999.

[51] D. McMorrow, J. S. Melinger, and S. Buchner, "Application of a pulsed laser for evaluation and optimization of seu-hard designs," *IEEE Trans. Nucl. Sci.*, vol. 47, no. 3 PART 1, pp. 559–565, Jun. 2000.

[52] N. M. Atkinson, R. W. Blaine, J. S. Kauppila, S. E. Armstrong, T. D. Loveless, N. C. Hooten, W. T. Holman, L. M. Massengill, and J. H. Warner, "RHBD technique for single-event charge cancellation in folded-cascode amplifiers," *IEEE Trans. Nucl. Sci.*, vol. 60, no. 4, pp. 2756–2761, Aug. 2013.

[53] D. McMorrow, S. Buchner, M. Baze, B. Bartholet, R. Katz, M. O'Bryan, C. Poivey, K. A. LaBel, R. Ladbury, M. Maher, and F. W. Sexton, "Laser-induced latchup screening and mitigation in CMOS devices," *IEEE Trans. Nucl. Sci.*, vol. 53, no. 4, pp. 1819–1824, Aug. 2006.

[54] S. D. LaLumondiere, R. Koga, J. V. Osborn, D. C. Mayer, R. C. Lacoe, and S. C. Moss, "Wavelength dependence of transient laser-induced latchup in Epi-CMOS test structures," *IEEE Trans. Nucl. Sci.*, vol. 49 I, no. 6, pp. 3059–3065, Dec. 2002.

[55] S. C. Moss, S. D. LaLumondiere, J. R. Scarpulla, K. P. MacWilliams, W. R. Crain, and R. Koga, "Correlation of Picosecond Laser-Induced Latchup and Energetic Particle-Induced Latchup in CMOS Test Structures," *IEEE Trans. Nucl. Sci.*, vol. 42, no. 6, pp. 1948–1956, Dec. 1995.

[56] V. F. Cavrois, V. Pouget, D. McMorrow, J. R. Schwank, N. Fel, F. Essely, R. S. Flores, P. Paillet, M. Gaillardin, D. Kobayashi, J. S. Melinger, O. Duhamel, P. E. Dodd, and M. R. Shaneyfelt, "Investigation of the Propagation Induced Pulse Broadening (PIPB) effect on single event transients in SOI and bulk inverter chains," *IEEE Trans. Nucl. Sci.*, vol. 55, no. 6, pp. 2842–2853, Dec. 2008.

[57] S. Buchner, K. Kang, D. Krening, G. Lannan, and R. Schneiderwind, "Dependence of the SEU window of vulnerability of a logic circuit on magnitude of deposited charge," *IEEE Trans. Nucl. Sci.*, vol. 40, no. 6, pp. 1853–1857, Dec. 1993.

[58] S. Buchner, M. Baze, D. Brown, D. McMorrow, and J. Malinger, "Comparison of error rates in combinational and sequential logic," *IEEE Trans. Nucl. Sci.*, vol. 44, no. 6, pp. 2209–2216, Dec. 1997.

[59] A. H. Johnston, "Charge Generation and Collection in p-n Junctions Excited with Pulsed Infrared Lasers," *IEEE Trans. Nucl. Sci.*, vol. 40, no. 6, pp. 1694–1702, Dec. 1993.

[60] D. McMorrow, J. B. Boos, D. Park, S. Buchner, A. R. Knudson, and J. S. Melinger, "Charge-collection dynamics of InP-based high electron mobility transistors (HEMTs)," *IEEE Trans. Nucl. Sci.*, vol. 49 III, no. 3, pp. 1396–1400, Jun. 2002.

[61] K. Ni, A. L. Sternberg, E. X. Zhang, J. A. Kozub, R. Jiang, R. D. Schrimpf, R. A. Reed, D. M. Fleetwood, M. L. Alles, D. McMorrow, J. Lin, A. Vardi, and J. Del Alamo, "Understanding Charge Collection Mechanisms in InGaAs FinFETs Using High-Speed Pulsed-Laser Transient Testing with Tunable Wavelength," *IEEE Trans. Nucl. Sci.*, vol. 64, no. 8, pp. 2069–2078, Aug. 2017.

[62] S. Buchner, D. McMorrow, A. Sternberg, L. Massengill, R. L. Pease, and M. Maher, "Single-event transient (SET) characterization of an LM119 voltage comparator: An approach to SET model validation using a pulsed laser," *IEEE Trans. Nucl. Sci.*, vol. 49 III, no. 3, pp. 1502–1508, Jun. 2002.

[63] F. Miller, N. Buard, T. Carrière, R. Dufayel, R. Gaillard, P. Poirot, J. M. Palau, B. Sagnes, and P. Fouillat, "Effects of beam spot size on the correlation between laser and heavy ion SEU testing," *IEEE Trans. Nucl. Sci.*, vol. 51, no. 6 II, pp. 3708–3715, Dec. 2004.

[64] A. Zanchi, S. Buchner, Y. Lotfi, S. Hisano, C. Hafer, and D. B. Kerwin, "Correlation of pulsed-laser energy and heavy-ion LET by matching analog SET ensemble signatures and digital SET thresholds," *IEEE Trans. Nucl. Sci.*, vol. 60, no. 6, pp. 4412–4420, Dec. 2013.

[65] J. M. Hales, A. Khachatrian, S. Buchner, N. J. Roche, J. Warner, and D. McMorrow, "A simplified approach for predicting pulsed-laser-induced carrier generation in semiconductor," *IEEE Trans. Nucl. Sci.*, vol. 64, no. 3, pp. 1006–1013, Mar. 2017.

[66] J. M. Hales, A. Khachatrian, S. Buchner, N. J. Roche, J. Warner, Z. E. Fleetwood, A. Ildefonso, J. D. Cressler, V. Ferlet-Cavrois, and D. McMorrow, "Experimental validation of an equivalent LET approach for correlating heavy-ion and laser-induced charge deposition," *IEEE Trans. Nucl. Sci.*, vol. 65, no. 8, pp. 1724–1733, 2018.

[67] R. W. Blaine, S. E. Armstrong, J. S. Kauppila, N. M. Atkinson, B. D. Olson, W. T. Holman, and L. W. Massengill, "RHBD Bias Circuits Utilizing Sensitive Node Active Charge Cancellation," *IEEE Trans. Nucl. Sci.*, vol. 58, no. 6, pp. 3060–3066, Dec. 2011.

[68] K. A. LaBel and M. M. Gates, "Single-Event-Effect Mitigation from a System Perspective," *IEEE Trans. Nucl. Sci.*, vol. 43, no. 2, pp. 654–660, Apr. 1996.

[69] M. M. Ghahroodi, M. Zwoliński, and E. Özer, "Radiation hardening by design: A novel gate level approach," in *2011 NASA/ESA Conference on Adaptive Hardware and Systems (AHS)*, Jun. 2011, pp. 74–79.

[70] J. A. Pellish, R. A. Reed, R. D. Schrimpf, M. L. Alles, M. Varadharajaperumal, G. Niu, A. K. Sutton, R. M. Diestelhorst, G. Espinel, R. Krithivasan, J. P. Comeau, J. D. Cressler, G. Vizkelethy, P. W. Marshall, R. A. Weller, M. H. Mendenhall, and E. J. Montes, "Substrate engineering concepts to mitigate

charge collection in deep trench isolation technologies," *IEEE Trans. Nucl. Sci.*, vol. 53, no. 6, pp. 3298–3305, Dec. 2006.

[71] M. Varadharajaperumal, G. Niu, J. D. Cressler, R. A. Reed, and P. W. Marshall, "Three-dimensional simulation of heavy-ion induced charge collection in SiGe HBTs on SOI," *IEEE Trans. Nucl. Sci.*, vol. 51, no. 6 II, pp. 3298–3303, Dec. 2004.

[72] S. Mateos-Angulo, M. San-Miguel-Montesdeoca, D. Mayor-Duarte, S. L. Khemchandani, and J. D. Pino, "SET analysis and radiation hardening techniques for CMOS LNA topologies," *Semiconductor Science and Technology*, vol. 33, no. 8, 2018.

[73] Yurong Hu and V. O. K. Li, "Satellite-based Internet: A Tutorial," *IEEE Commun. Mag.*, vol. 39, no. 3, pp. 154–162, Mar. 2001.

[74] "Satellite Communications – A Continuing Revolution," *IEEE Aerosp. Electron. Syst. Mag.*, vol. 15, no. 10, pp. 95–107, Oct. 2000.

[75] M. Irsigler, G. W. Hein, and A. Schmitz-Peiffer, "Use of C-Band frequencies for satellite navigation: benefits and drawbacks," *GPS Solutions*, vol. 8, pp. 119–139, 2004.

[76] G. W. Hein, M. Irsigler, J. A. Avila-Rodriguez, S. Wallner, T. Pany, and P. Hartl, "Envisioning a Future GNSS System of Systems, Part 3 – A Role for C-Band?" *Inside GNSS*, pp. 64–73, May 2007.

[77] K. Maine, P. Anderson, and F. Bayuk, "Communication Architecture for GPS III," in *2004 IEEE Aerospace Conf. Proc.*, Mar. 2004, pp. 1532 – 1539.

[78] Z. Ali, I. Barnard, P. Fox, P. Duggan, R. Gray, P. Allan, A. Brand, and R. Ste-Mari, "Description of RADARSAT-2 synthetic aperture radar design," *Canadian Journal of Remote Sensing*, vol. 30, no. 3, pp. 246–257, 2004.

[79] F. Miller, A. Germain, N. Buard, R. Gahiard, P. Poirot, C. Chatry, T. Carriere, and R. Dufayel, "Interest of laser test facility for the assessment of natural radiation environment effects on integrated circuits based systems," in *Proc. 7th Eur. Conf. Radiat. Its Eff. Components Syst. 2003. RADECS 2003.*, vol. 2003-Septe, Sep. 2003, pp. 199–209.

[80] D. Lewis, V. Pouget, F. Beaudoin, P. Perdu, H. Lapuyade, P. Fouillat, and A. Touboul, "Backside laser testing of ICs for SET sensitivity evaluation," *IEEE Trans. Nucl. Sci.*, vol. 48, no. 6 I, pp. 2193–2201, Dec. 2001.

[81] D. McMorrow, W. T. Lotshaw, J. S. Melinger, S. Buchner, and R. L. Pease, "Subbandgap laser-induced single event effects: carrier generation via two-photon absorption," *IEEE Trans. Nucl. Sci.*, vol. 49, no. 6, pp. 3002–3008, Dec. 2002.

[82] J. M. Hales, A. Khachatrian, S. Buchner, J. Warner, A. Ildefonso, G. N. Tzintzarov, D. Nergui, D. M. Monahan, S. D. LaLumondiere, J. D. Cressler, and D. McMorrow, "New Approach for Pulsed-Laser Testing That Mimics Heavy-Ion Charge Deposition Profiles," *IEEE Trans. Nucl. Sci.*, vol. 67, no. 1, pp. 81–90, Jan. 2020.

[83] K. L. Ryder, L. D. Ryder, A. L. Sternberg, J. A. Kozub, E. X. Zhang, A. Khachatrian, S. P. Buchner, D. P. Mcmorrow, J. M. Hales, Y. Zhao, L. Wang, C. Wang, R. A. Weller, R. D. Schrimpf, S. M. Weiss, and R. A. Reed, "Comparison of Sensitive Volumes Associated With Ion- and Laser-Induced Charge Collection in an Epitaxial Silicon Diode," *IEEE Trans. Nucl. Sci.*, vol. 67, no. 1, pp. 57–62, Jan. 2020.

[84] F. Wrobel, A. D. Touboul, V. Pouget, L. Dilillo, E. Lorfevre, and F. Saigne, "The Power Law Shape of Heavy Ions Experimental Cross Section," *IEEE Trans. Nucl. Sci.*, vol. 64, no. 1, pp. 427–433, Jan. 2017.

[85] J. F. Ziegler, J. P. Biersack, and M. D. Ziegler, "SRIM." [Online]. Available: http://www.srim.org/SRIM/SRIM2011.htm

[86] V. Pouget, H. Lapuyade, P. Fouillat, D. Lewis, and S. Buchner, "Theoretical investigation of an equivalent laser LET," *Microelectron. Reliab.*, vol. 41, no. 9-10, pp. 1513–1518, Sep. 2001.

[87] D. I. Kovsh, S. Yang, D. J. Hagan, and E. W. Van Stryland, "Nonlinear optical beam propagation for optical limiting," *Appl. Opt.*, vol. 38, no. 24, p. 5168, Aug. 1999.

[88] N. E. Lourenco, S. D. Phillips, T. D. England, A. S. Cardoso, Z. E. Fleetwood, K. A. Moen, D. McMorrow, J. H. Warner, S. P. Buchner, P. Paki-Amouzou, J. Pekarik, D. Harame, A. Raman, M. Turowski, and J. D. Cressler, "An investigation of single-event effects and potential SEU mitigation strategies in fourth-generation, 90 nm SiGe BiCMOS," *IEEE Trans. Nucl. Sci.*, vol. 60, no. 6, pp. 4175–4183, 2013.

[89] J. A. Pellish, R. A. Reed, A. K. Sutton, R. A. Weller, M. A. Carts, P. W. Marshall, C. J. Marshall, R. Krithivasan, J. D. Cressler, M. H. Mendenhall, R. D. Schrimpf, K. M. Warren, B. D. Sierawski, and G. F. Niu, "A generalized SiGe HBT single-event effects model for on-orbit event rate calculations," *IEEE Trans. Nucl. Sci.*, vol. 54, no. 6, pp. 2322–2329, Dec. 2007.

[90] J. A. Pellish, R. A. Reed, D. McMorrow, J. S. Melinger, P. Jenkins, A. K. Sutton, R. M. Diestelhorst, S. D. Phillips, J. D. Cressler, V. Pouget, N. D. Pate, J. A. Kozub, M. H. Mendenhall, R. A. Weller, R. D. Schrimpf, P. W. Marshall, A. D. Tipton, and G. Niu, "Laser-induced current transients in silicon-germanium HBTs," *IEEE Trans. Nucl. Sci.*, vol. 55, no. 6, pp. 2936–2942, Dec. 2008.

[91] J. A. Pellish, R. A. Reed, D. McMorrow, G. Vizkelethy, V. F. Cavrois, J. Baggio, P. Paillet, O. Duhamel, K. A. Moen, S. D. Phillips, R. M. Diestelhorst, J. D. Cressler, A. K. Sutton, A. Raman, M. Turowski, P. E. Dodd, M. L. Alles, R. D. Schrimpf, P. W. Marshall, and K. A. LaBel, "Heavy ion microbeam-and broadbeam-induced transients in SiGe HBTs," *IEEE Trans. Nucl. Sci.*, vol. 56, no. 6, pp. 3078–3084, 2009.

[92] B. E. Fischer, "The scanning heavy ion microscope at GSI," *Nucl. Inst. Methods Phys. Res. B*, vol. 10-11, no. PART 2, pp. 693–696, May 1985.

[93] A. Khachatrian, N. J. Roche, D. McMorrow, J. H. Warner, S. P. Buchner, and J. S. Melinger, "A Dosimetry Methodology for Two-Photon Absorption Induced Single-Event Effects Measurements," *IEEE Trans. Nucl. Sci.*, vol. 61, no. 6, pp. 3416–3423, Dec. 2014.

[94] H. Urey, "Spot size, depth-of-focus, and diffraction ring intensity formulas for truncated Gaussian beams," *Appl. Opt.*, vol. 43, no. 3, pp. 620–625, Jan. 2004.

[95] R. L. Schmid, A. C. Ulusoy, S. Zeinolabedinzadeh, and J. D. Cressler, "A comparison of the degradation in RF performance due to device interconnects in advanced SiGe HBT and CMOS technologies," *IEEE Trans. Electron Devices*, vol. 62, no. 6, pp. 1803–1810, 2015.

[96] J. M. Hales, A. Khachatrian, J. Warner, S. Buchner, A. Ildefonso, G. N. Tzintzarov, D. Nergui, D. M. Monahan, S. D. LaLumondiere, J. D. Cressler, and D. McMorrow, "Using Bessel beams and two-photon absorption to predict radiation effects in microelectronics," *Opt. Express*, vol. 27, no. 26, pp. 37 652–37 666, Dec. 2019.

[97] C. M. Hsieh, P. C. Murley, and R. R. O'Brien, "A field-funneling effect on the collection of alpha-particle-generated carriers in silicon devices," *IEEE Trans. Electron Devices*, vol. 2, no. 4, pp. 103–105, Apr. 1981.

[98] B. Razavi, *RF Microelectronics*. Prentice Hall, 2012.

[99] G. Vallant, M. Epp, W. Schlecker, U. Schneider, L. Anttila, and M. Valkama, "Analog IQ impairments in Zero-IF radar receivers: Analysis, measurements and digital compensation," in *2012 IEEE I2MTC - Int. Instrum. Meas. Technol. Conf. Proc.*, May 2012, pp. 1703–1707.

[100] S. Mirabbasi and K. Martin, "Classical and modern receiver architectures," *IEEE Commun. Mag.*, vol. 38, no. 11, pp. 132–139, Nov. 2000.

[101] B. Jagannathan, M. Khater, F. Pagette, J. S. Rieh, D. Angell, H. Chen, J. Florkey, F. Golan, D. R. Greenberg, R. Groves, S. J. Jeng, J. Johnson, E. Mengistu, K. T. Schonenberg, C. M. Schnabel, P. Smith, A. Stricker, D. Ahlgren, G. Freeman, K. Stein, and S. Subbanna, "Self-aligned SiGe NPN transistors with 285 GHz fmax and 207 GHz fT in a manufacturable technology," *IEEE Electron Device Lett.*, vol. 23, no. 5, pp. 258–260, May 2002.

[102] R. A. Shafik, M. S. Rahman, and A. H. Islam, "On the extended relationships among EVM, BER and SNR as performance metrics," in *Proc. 4th Int. Conf. Electr. Comput. Eng. ICECE 2006*, Dec. 2006, pp. 408–411.

[103] W. A. Teso, *Communication systems engineering*, ser. Pearson Education. Prentice Hall, 1972, vol. 293, no. 2.

[104] K. McClaning, *Wireless Receiver Design for Digital Communications*, ser. Telecommunications Series. Institution of Engineering and Technology, 2012.

[105] J. M. Espinosa-Duran, J. Velasco-Medina, G. Huertas, R. Velasco, and J. L. Huertas, "Measuring SET effects in a CMOS operational amplifier using a built-in detector," in *IEEE AFRICON Conf.*, Sep. 2007, pp. 1–7.

[106] Z. Zhang, T. Wang, L. Chen, and J. Yang, "A new Bulk Built-In Current Sensing circuit for single-event transient detection," in *Can. Conf. Electr. Comput. Eng.*, May 2010, pp. 1–4.

[107] H. Liang, P. Mishra, and K. Wu, "Error correction on-demand: A low power register transfer level concurrent error correction technique," *IEEE Trans. Comput.*, vol. 56, no. 2, pp. 243–252, Feb. 2007.

[108] J. W. May and G. M. Rebeiz, "Design and characterization of W-band SiGe RFICs for passive millimeter-wave imaging," *IEEE Trans. Microw. Theory Tech.*, vol. 58, no. 5 PART 2, pp. 1420–1430, May 2010.

[109] M. Uzunkol, W. Shin, and G. M. Rebeiz, "Design and analysis of a low-power 3-6-Gb/s 55-GHz OOK receiver with high-temperature performance," *IEEE Trans. Microw. Theory Tech.*, vol. 60, no. 10, pp. 3263–3271, Oct. 2012.

[110] R. L. Schmid, P. Song, C. T. Coen, A. C. Ulusoy, and J. D. Cressler, "A W-band integrated silicon-germanium loop-back and front-end transmit-receive switch for Built-in-self-test," in *2015 IEEE MTT-S Int. Microw. Symp. IMS 2015*, May 2015, pp. 1–4.

[111] A. Valdes-Garcia, R. Venkatasubramanian, R. Srinivasan, J. Silva-Martinez, and E. Sánchez-Sinencio, "A CMOS RF RMS detector for built-in testing of wireless transceivers," in *Proc. IEEE VLSI Test Symp.*, May 2005, pp. 249–254.

[112] W. M. L. Kuo, Q. Liang, J. D. Cressler, and M. A. Mitchell, "An X-band SiGe LNA with 1.36 dB mean noise figure for monolithic phased array transmit/receive radar modules," in *IEEE Radio Frequency Integrated Circuits (RFIC) Symposium*, 2006, pp. 498–501.

[113] L. Gilreath, V. Jain, and P. Heydari, "Design and analysis of a W-band SiGe direct-detection-based passive imaging receiver," *IEEE J. Solid-State Circuits*, vol. 46, no. 10, pp. 2240–2252, Oct. 2011.

[114] D. A. Black, W. H. Robinson, I. Z. Wilcox, D. B. Limbrick, and J. D. Black, "Modeling of Single Event Transients with Dual Double-Exponential Current Sources: Implications for Logic Cell Characterization," *IEEE Trans. Nucl. Sci.*, vol. 62, no. 4, pp. 1540–1549, 2015.

[115] S. Rami, A. Paganini, and W. R. Eisenstadt, "A minimally invasive wideband mixed-mode detector for mm-Wave BIST applications," in *Proc. - Electron. Components Technol. Conf.*, Jun. 2010, pp. 735–743.

[116] T. Zhang, W. R. Eisenstadt, R. M. Fox, and Q. Yin, "Bipolar microwave RMS power detectors," *IEEE J. Solid-State Circuits*, vol. 41, no. 9, pp. 2188–2192, Sep. 2006.

[117] T. Zhang, W. R. Eisenstadt, and R. M. Fox, "A novel 5GHz RF power detector," in *Proc. - IEEE Int. Symp. Circuits Syst.*, vol. 1, May 2004, pp. I–897–900 Vol.1.

[118] A. Vanelli-Coralli, G. E. Corazza, G. K. Karagiannidis, P. T. Mathiopoulos, D. S. Michalopoulos, C. Mosquera, S. Papaharalabos, and S. Scalise, "Satellite communications: Research trends and open issues," in *2007 Int. Work. Satell. Sp. Commun. IWSSC'07*, Sep. 2007, pp. 71–75.

[119] I. Song, M. Cho, Z. E. Fleetwood, Y. Gong, S. Pavlidis, S. P. Buchner, D. McMorrow, P. Paki, M. Kaynak, and J. D. Cressler, "p-n-p-Based RF Switches for the Mitigation of Single-Event Transients in a Complementary SiGe BiCMOS Platform," *IEEE Trans. Nucl. Sci.*, vol. 65, no. 1, pp. 391–398, Jan. 2018.

[120] A. Ildefonso, N. E. Lourenco, Z. E. Fleetwood, M. T. Wachter, G. N. Tzintzarov, A. S. Cardoso, N. J. Roche, A. Khachatrian, D. Mcmorrow, S. P. Buchner, J. H. Warner, P. Paki, M. Kaynak, B. Tillack, and J. D. Cressler, "Single-Event Transient Response of Comparator Pre-Amplifiers in a Complementary SiGe Technology," *IEEE Trans. Nucl. Sci.*, vol. 64, no. 1, pp. 89–96, 2017.

[121] N. E. Lourenco, A. Ildefonso, G. N. Tzintzarov, Z. E. Fleetwood, K. Motoki, P. Paki, M. Kaynak, and J. D. Cressler, "Single-Event Upset Mitigation in a Complementary SiGe HBT BiCMOS Technology," *IEEE Trans. Nucl. Sci.*, vol. 65, no. 1, pp. 231–238, 2018.

[122] B. Heinemann, R. Barth, D. Bolze, J. Drews, P. Formanek, O. Fursenko, M. Glante, K. Glowatzki, A. Gregor, U. Haak, W. Höppner, D. Knoll, R. Kurps, S. Marschmeyer, S. Orlowski, H. Rücker, P. Schley, D. Schmidt, R. Scholz, W. Winkler, and Y. Yamamoto, "A Complementary BiCMOS Technology with High Speed npn and pnp SiGe:C HBTs," in *Tech. Dig. - Int. Electron Devices Meet.*, Dec. 2003, pp. 117–120.

[123] B. Heinemann, R. Barth, D. Bolze, J. Drews, P. Formanek, T. Grabolla, U. Haak, W. Höppner, D. Knoll, K. Köpke, B. Kuck, R. Kurps, S. Marschmeyer, H. H. Richter, H. Rücker, P. Schley, D. Schmidt, W. Winkler, D. Wolansky,

H. E. Wulf, and Y. Yamamoto, "A low-parasitic collector construction for high-speed SiGe:C HBTs," in *Tech. Dig. - Int. Electron Devices Meet. IEDM*, 2004, pp. 251–254.

[124] C. Çaışkan, I. Kalyoncu, M. Yazici, and Y. Gurbuz, "Sub-1-db and wideband sige bicmos low-noise amplifiers for x -band applications," *IEEE Trans. Circuits Syst. I*, vol. 66, no. 4, pp. 1419–1430, Apr. 2019.

[125] Y. Koutsoyannopoulos, Y. Papananos, S. Bantas, and C. Alemanni, "Performance limits of planar and multi-layer integrated inductors," in *2000 IEEE International Symposium on Circuits and Systems (ISCAS)*, vol. 2, May 2000, pp. 160–163.

[126] E. Ragonese, T. Biondi, G. Longo, and G. Palmisano, "A comparative analysis of monolithic spiral inductors in silicon bipolar technology," in *Southwest Symposium on Mixed-Signal Design, 2003.*, Feb. 2003, pp. 144–149.

[127] M. Ballicchia and S. Orcioni, "A Methodology for Design and Modeling of Optimum Quality Spiral Inductors," in *2008 IEEE Topical Meeting on Silicon Monolithic Integrated Circuits in RF Systems*, Jan. 2008, pp. 102–105.

[128] M. Gordon and S. P. Voinigescu, "An inductor-based 52-GHz 0.18 μm SiGe HBT cascode LNA with 22 dB gain," in *Proceedings of the 30th European Solid-State Circuits Conference*, Sep. 2004, pp. 287–290.

[129] R. L. Schmid, C. T. Coen, S. Shankar, and J. D. Cressler, "Best Practices to Ensure the Stability of SiGe HBT Cascode Low Noise Amplifiers," in *2012 IEEE Bipolar/BiCMOS Circuits and Technology Meeting (BCTM)*, Sep. 2012, pp. 1–4.

[130] S. C. Ekpo and D. George, "Impact of Noise Figure on a Satellite Link Performance," *IEEE Commun. Lett.*, vol. 15, no. 9, pp. 977–979, Sep. 2011.

[131] M. Bellini, S. D. Phillips, R. M. Diestelhorst, P. Cheng, J. D. Cressler, P. W. Marshall, M. Turowski, G. Avenier, A. Chantre, and P. Chevalier, "Novel total dose and heavy-ion charge collection phenomena in a new SiGe HBT on thin-film SOI technology," *IEEE Trans. Nucl. Sci.*, vol. 55, no. 6, pp. 3197–3201, Dec. 2008.

[132] T. Thibeault, E. Preisler, J. Zheng, L. Dong, S. Chaudhry, S. Jordan, and M. Racanelli, "A study of ultra-high performance SiGe HBT devices on SOI," in *Proc. IEEE Bipolar/BiCMOS Circuits Technol. Meet.*, Sep. 2013, pp. 235–238.

[133] J. D. Cressler, *Silicon heterostructure handbook: Materials, fabrication, devices, circuits and applications of sige and si strained-layer epitaxy.* CRC press, 2005.

[134] L. Yang, J. R. Watling, R. C. Wilkins, M. Boriçi, J. R. Barker, A. Asenov, and S. Roy, "Si/SiGe heterostructure parameters for device simulations," *Semicond. Sci. Technol.*, vol. 19, no. 10, pp. 1174–1182, Aug. 2004.

[135] E. L. Petersen, J. C. Pickel, J. H. Adams, and E. C. Smith, "Rate prediction for single event effects – A critique," *IEEE Trans. Nucl. Sci.*, vol. 39, no. 6, pp. 1577–1599, Dec. 1992.

[136] "FRED Optical Engineering Software." [Online]. Available: https://photonengr.com/

[137] I. Song, M. K. Cho, M. A. Oakley, A. Ildefonso, I. Ju, S. P. Buchner, D. McMorrow, P. Paki, and J. D. Cressler, "On the Application of Inverse-Mode SiGe HBTs in RF Receivers for the Mitigation of Single-Event Transients," *IEEE Trans. Nucl. Sci.*, vol. 64, no. 5, pp. 1142–1150, 2017.

[138] M. Varadharajaperumal, G. Niu, X. Wei, T. Zhang, J. D. Cressler, R. A. Reed, and P. W. Marshall, "3-D simulation of SEU hardening of SiGe HBTs using shared dummy collector," *IEEE Trans. Nucl. Sci.*, vol. 54, no. 6, pp. 2330–2337, Dec. 2007.

[139] A. K. Sutton, M. Bellini, J. D. Cressler, J. A. Pellish, R. A. Reed, P. W. Marshall, G. Niu, G. Vizkelethy, M. Turowski, and A. Raman, "An evaluation of transistor-layout RHBD techniques for SEE mitigation in SiGe HBTs," *IEEE Trans. Nucl. Sci.*, vol. 54, no. 6, pp. 2044–2052, Dec. 2007.

[140] G. Niu, H. Yang, M. Varadharajaperumal, Y. Shi, J. D. Cressler, R. Krithivasan, P. W. Marshall, and R. Reed, "Simulation of a new back junction approach for reducing charge collection in 200 GHz SiGe HBTs," *IEEE Trans. Nucl. Sci.*, vol. 52, no. 6, pp. 2153–2157, Dec. 2005.

[141] S. D. Phillips, K. A. Moen, L. Najafizadeh, R. M. Diestelhorst, A. K. Sutton, J. D. Cressler, G. Vizkelethy, P. E. Dodd, and P. W. Marshall, "A comprehensive understanding of the efficacy of N-ring SEE hardening methodologies in SiGe HBTs," *IEEE Trans. Nucl. Sci.*, vol. 57, no. 6 PART 1, pp. 3400–3406, 2010.

[142] G. Niu, R. Krithivasan, J. D. Cressler, P. A. Riggs, B. A. Randall, P. W. Marshall, R. A. Reed, and B. Gilbert, "A comparison of SEU tolerance in high-speed SiGe HBT digital logic designed with multiple circuit architectures," *IEEE Trans. Nucl. Sci.*, vol. 49 I, no. 6, pp. 3107–3114, Dec. 2002.

[143] D. L. Hansen, P. Chu, K. Jobe, A. L. McKay, and H. P. Warren, "SEU cross sections of hardened and unhardened SiGe circuits," *IEEE Trans. Nucl. Sci.*, vol. 53, no. 6, pp. 3579–3586, Dec. 2006.

[144] X. Wei, T. Zhang, G. Niu, M. Varadharajaperumal, J. D. Cressler, and P. W. Marshall, "3-D mixed-mode simulation of single event transients in SiGe HBT

emitter followers and resultant hardening guidelines," *IEEE Trans. Nucl. Sci.*, vol. 55, no. 6, pp. 3360–3366, Dec. 2008.

[145] T. S. Mukherjee, A. K. Sutton, K. T. Kornegay, R. Krithivasan, J. D. Cressler, G. Niu, and P. W. Marshall, "A novel circuit-level SEU hardening technique for high-speed SiGe HBT logic circuits," *IEEE Trans. Nucl. Sci.*, vol. 54, no. 6, pp. 2086–2091, Dec. 2007.

[146] Z. E. Fleetwood, A. Ildefonso, G. N. Tzintzarov, B. Wier, U. Raghunathan, M. K. Cho, I. Song, M. T. Wachter, D. Nergui, A. Khachatrian, J. H. Warner, P. McMarr, H. Hughes, E. Zhang, D. McMorrow, P. Paki, A. Joseph, V. Jain, and J. D. Cressler, "SiGe HBT Profiles with Enhanced Inverse-Mode Operation and Their Impact on Single-Event Transients," *IEEE Trans. Nucl. Sci.*, vol. 65, no. 1, pp. 399–406, 2018.

[147] P. S. Chakraborty, K. Moen, M. Bellini, and J. D. Cressler, "Investigation of the device design challenges and optimization issues associated with complementary SiGe HBT scaling," *2009 Int. Semicond. Device Res. Symp. ISDRS '09*, vol. 4, pp. 5–6, 2009.

[148] A. P. Omprakash, P. S. Chakraborty, H. Ying, A. S. Cardoso, A. Ildefonso, and J. D. Cressler, "On the potential of using SiGe HBTs on SOI to support emerging applications up to 300°C," in *Proc. IEEE Bipolar/BiCMOS Circuits Technol. Meet.*, vol. 2015-Novem, Oct. 2015, pp. 27–30.

[149] H. Gong, K. Ni, E. X. Zhang, A. L. Sternberg, J. A. Kozub, K. L. Ryder, R. F. Keller, L. D. Ryder, S. M. Weiss, R. A. Weller, M. L. Alles, R. A. Reed, D. M. Fleetwood, R. D. Schrimpf, A. Vardi, and J. A. Del Alamo, "Scaling Effects on Single-Event Transients in InGaAs FinFETs," *IEEE Trans. Nucl. Sci.*, vol. 65, no. 1, pp. 296–303, Jan. 2018.

[150] L. D. Ryder, R. D. Schrimpf, S. M. Weiss, R. A. Reed, K. L. Ryder, A. L. Sternberg, J. A. Kozub, H. Gong, E. X. Zhang, D. Linten, J. Mitard, and R. A. Weller, "Polarization Dependence of Pulsed Laser-Induced SEEs in SOI FinFETs," *IEEE Trans. Nucl. Sci.*, vol. 67, no. 1, pp. 38–43, Jan. 2020.

Vita

Adrian Ildefonso Rosa is originally from Arroyo, a small town in the southeastern coast of Puerto Rico. He received his B.S. in Computer Engineering in 2014 from the University of Puerto Rico at Mayagüez, where he graduated with top honors. He then joined the Silicon-Germanium Devices and Circuits Team at the Georgia Institute of Technology under the supervision of Dr. John D. Cressler. He received his M.S. in Electrical and Computer Engineering in May 2017, and his Ph.D. in Electrical and Computer Engineering in August 2020. During his time at Georgia Tech, he received the GEM Fellowship in 2014 and the NSF Graduate Research Fellowship in 2015.

Adrian's research focuses on studying the effects of ionizing radiation on electronic devices, circuits and systems designed using silicon-germanium (SiGe) technologies. The primary goal of his work is to build more robust systems for space-based applications by identifying and implementing novel design strategies that improve the radiation tolerance of analog and RF circuits. Through internships at the U. S. Naval Research Laboratory in Washington DC, USA, he has also worked on quantitatively correlating fundamental differences in charge deposition between heavy-ion- and laser-induced single-event transients (SETs) in SiGe heterojunction bipolar transistors. This effort aims to establish laser-based testing as an additional tool to fully qualify electronics for space applications.

He has authored and co-authored more than 30 refereed journal publications and conference proceedings. Adrian received both the Outstanding Student Paper Award and the Outstanding Conference Paper Award at the 2018 IEEE Nuclear and Space Radiation Effects Conference, only the second time in the history of the conference that both awards have been given to a student in the same year. He is also the recipient of the IEEE NPSS Graduate Scholarship and the IEEE NPSS Phelps Continuing Education Grant.